Håkon Drengsrud

# Systematic Evaluation of VIV Prediction for Riser with Partial Strake Coverage

Master's thesis in MTMART
Supervisor: Prof. Svein Sævik, NTNU, and Jie Wu, Sintef Ocean
June 2019

Master's thesis

**NTNU**
Norwegian University of Science and Technology
Faculty of Engineering
Department of Marine Technology

NTNU
Norwegian University of
Science and Technology

Håkon Drengsrud

# Systematic Evaluation of VIV Prediction for Riser with Partial Strake Coverage

Master's thesis in MTMART
Supervisor: Prof. Svein Sævik, NTNU, and Jie Wu, Sintef Ocean
June 2019

Norwegian University of Science and Technology
Faculty of Engineering
Department of Marine Technology

NTNU
Kunnskap for en bedre verden

**NTNU Trondheim**
**Norwegian University of Science and Technology** *Faculty of Engineering*
*Department of Marine Technology*

# MASTER THESIS SPRING 2019

**for**

**Stud. tech. Håkon Drengsrud**

## Systematic Evaluation of VIV Prediction for Riser with Partial Strake Coverage

*Vurdering av VIV prediksjon for stigerør som er delvis dekket med strakes*

Vortex induced vibrations (VIV) can lead to fast accumulation of fatigue damage of slender marine structures. Strakes have been used as a common VIV suppression device. It can effectively suppress VIV, but it increases the drag loads on the structure and installation cost. Therefore, partial strake coverage is often considered due to economical and practical reasons. Recently, model tests have been carried out at SINTEF Ocean to study the suppression of VIV for risers with partial coverage. In addition, a new time-domain (TD) VIV prediction model has been developed that enables relevant modelling of the test set-ups. The objective of this project is to form the basis for a systematic evaluation of the TD VIV model prediction for risers with partial strake coverage versus experimental test data and is to be carried out as a continuation of the project work from fall 2018 as follows:

1. Literature study on the fundamental theory of VIV and the numerical prediction tools available. Learn how to use the new TD VIV prediction tool.
2. Get an overview of the experimental data and learn how to process these data into a convenient format for comparison with the TD VIV model. Select the most relevant cases with respect to further studies.
3. Develop an analytical hydrodynamic load model concept for the strakes and establish a numerical model as a basis for correlation studies.
4. Perform TD VIV simulation and compare with model test results to demonstrate that the model can be used for further studies.
5. Perform correlation studies between TD VIV simulation and model test results with respect to the hydrodynamic parameters needed to get a best fit.
6. Perform case study of a deepwater riser with/without strakes.
7. Conclusions and recommendations for further work

All necessary input data are assumed to be provided by Sintef Ocean.

The work scope in terms of cases to be included is to be agreed upon with the supervisors.

In the thesis, the candidate shall present his personal contribution to the resolution of problems within the scope of the work.

Theories and conclusions should be based on mathematical derivations and/or logic reasoning identifying the various steps in the deduction.

The candidate should utilise the existing possibilities for obtaining relevant literature.

**Thesis format**
The thesis should be organised in a rational manner to give a clear exposition of results, assessments, and conclusions. The text should be brief and to the point, with a clear language. Telegraphic language should be avoided.

The thesis shall contain the following elements: A text defining the scope, preface, list of contents, summary, main body of thesis, conclusions with recommendations for further work, list of symbols and acronyms, references and (optional) appendices. All figures, tables and equations shall be numerated.

The supervisors may require that the candidate, in an early stage of the work, presents a written plan for the completion of the work.

The original contribution of the candidate and material taken from other sources shall be clearly defined. Work from other sources shall be properly referenced using an acknowledged referencing system.

The thesis shall be submitted in electronic format (.pdf):

- Signed by the candidate
- The text defining the scope shall be included (this document)
- Drawings and/or computer models that are not suited to be part of the thesis in terms of appendices shall be provided on separate (.zip) files.

**Ownership**
NTNU has according to the present rules the ownership of the thesis. Any use of the thesis has to be approved by NTNU (or external partner when this applies). The department has the right to use the thesis report as if the work was carried out by a NTNU employee, if nothing else has been agreed in advance.

**Thesis supervisors:**

Prof. Svein Sævik, NTNU
Jie Wu, Sintef Ocean

**Deadline: June , 2019**

Trondheim, January 21, 2019

Svein Sævik

Candidate – date and signature:

# Preface

This report is the result of my master's thesis work at the Department of Marine Technology at the Norwegian University of Technology and Science during the spring 2019.

Crucial parts of the thesis work involved familiarizing with the software Riflex and experiments related to VIV. On one hand this involved getting to know a highly theoretical non-linear finite element tool, and on the other hand dive into practical research and all the factors that may influence a VIV experiment. No experiments were carried out in this thesis, nevertheless the thesis work has provided me with practical and theoretical VIV knowledge, as well as an understanding of the benefits of nonlinear finite element programs, which I am grateful for.

I wish to express my gratitude to my supervisors Prof. Svein Sævik, NTNU and Jie Wu, Sintef Ocean for weekly guidance and discussions. I would in particular like to point out their high level of reliability and availability. Further, I am grateful to Svein for granting me access to the weekly VIV meetings where I have been exposed to the relevant research of other people working with VIV. I also owe great thanks to the participants from both NTNU and Sintef Ocean at the VIV meetings for their encouragement and recommendations.

For those reading this thesis it will be an advantage to be familiar with hydrodynamics and structural mechanics.

Candidate - date and signature:
June 6, 2019
Håkon Drengsrud
..............................
Håkon Drengsrud

# Abstract

With basis in the PhD work by Mats J. Thorsen and Jan V. Ulveseter, this thesis presents the work on a semi-empirical time domain tool able to predict the vortex-induced vibrations (VIV) response of both bare risers and risers partially fitted with strakes. A goal was to establish a model that can provide accurate predictions for a large variety of cases, another was to avoid making the model too complex. Overall, this thesis aims at bringing the time domain VIV prediction tool first formulated by Thorsen, and further developed by Ulveseter, a step closer of one day becoming a tool suitable for engineering applications.

Two separate hydrodynamic load models for bare and straked sections were formulated, where both were based on Morison's equation and hence included both drag and inertia forces. The model for bare sections included an additional term related to vortex-induced excitation forces. A key element in the modelling of the vortex-induced excitation forces was a synchronization model that connected the vortex shedding and the pipe motion to simulate lock-in. While the load model for bare sections was defined by a set of empirical parameters, the load model for straked sections was given by hydrodynamic added mass and drag coefficients found from analytical formulations.

The hydrodynamic load model was combined with a non-linear finite element structural model in order to predict the VIV response of flexible pipes. VIV of both bare and partially straked (50% and 75%) risers in uniform and shear flow were simulated, and the same set of empirical parameters for defining the hydrodynamic load model was used for all simulated cases. The quality of the response predictions was evaluated in terms of both cross-flow and in-line stress, fatigue and displacement. Only fundamental VIV response was considered. In general the model provided accurate or conservative results, but non-conservative predictions were observed for some of the cases with low current speed. However, these are associated with low fatigue damage and will not be of large significance when designing a real marine riser. Extreme conservatism was observed in some cases, which also underlines that it is difficult to produce accurate results for a wide range of cases with a single set of empirical parameters.

Simulations of the response for the partially straked risers revealed that the hydrodynamic model for strakes is promising, however the application seems to be restricted to when the response is controlled by the bare section, i.e. when the percentage strake coverage is not too high. As the fatigue damage in general is very low for risers fitted with high percentage strake coverage, this is not a major drawback for the model.

# Sammendrag

Med utgangspunkt i doktorgradsavhandlingene til Mats J. Thorsen og Jan V. Ulveseter presenterer denne oppgaven en semi-empirisk tidsplan-modell som er i stand til å predikere virvelinduserte vibrasjoner (VIV) for stigerør både med og uten strakes. Et mål var å etablere en modell som gir nøyaktige prediksjoner for et bredt utvalg av lasttilfeller, i tillegg til at det var ønskelig å ha en så enkel modell som mulig. Det overordnede målet ved denne avhandlingen var å ta ytterligere et steg mot å gjøre VIV tidsplan-modellen utviklet av Thorsen og Ulveseter anvendbar for reelle ingeniør-problemstillinger.

To separate hydrodynamiske lastmodeller for seksjoner med og uten strakes ble etablert, der begge modellene var basert på Morisons ligning og dermed inkluderte både drag- og treghetskrefter. Modellen for bare seksjoner hadde i tillegg et ledd relatert til virvelinduserte eksitasjonskrefter. Et svært sentralt element i modelleringen av de virvelinduserte eksitasjonskreftene var en synkroniseringsmodell som koblet virvelavløsningen og bevegelsen til stigerøret slik at lock-in ble simulert. Lastmodellen for bare seksjoner var gitt av et sett med empiriske parametere, mens analytiske hydrodynamiske tilleggsmasse- og dragkoeffisienter definerte lastmodellen for seksjoner med strakes.

Den hydrodynamiske lastmodellen ble kombinert med en ikke-lineær elementmodell for prediksjon av VIV-respons for fleksible rør. VIV for både bare stigerør og stigerør delvis dekket med strakes (50% og 75%) i uniform strømning og skjær-strømning ble simulert, og det samme settet med empiriske parametere ble brukt i alle simuleringer. For å vurdere kvaliteten på respons-prediksjonene ble det sett på spenninger, utmatting og utbøyinger både cross-flow og in-line. Kun fundamental VIV-respons ble tatt i betraktning. Generelt gir modellen nøyaktige eller konservative resultater, men ikke-konservative resultater ble observert for noen av tilfellene med lav strømningshastighet. Disse tilfellene er imidlertid assosiert med liten utmatting og vil derfor ikke være av stor betydning i designet av et reelt stigerør. Ekstremt konservative resultater ble observert i en del tilfeller, og dette understreker hvor vanskelig det er å produsere nøyaktige resultater for et bredt spekter av tilfeller med kun ett sett empiriske parametere.

Simuleringer med stigerør delvis dekket med strakes avslørte at den hydrodynamiske modellen er lovende. Samtidig virker det som at bruken av modellen vil være begrenset til tilfeller der responsen er kontrollert av den bare delen av stigerøret, altså når andelen av røret som er dekket med strakes ikke er for stor. Ettersom utmattingen generelt er veldig liten for stigerør med stor andel strakes-dekning er ikke dette en stor ulempe med modellen.

# List of symbols

| | |
|---|---|
| $\hat{f}$ | Non-dimensional frequency, typically related to oscillation frequency of structure |
| $\hat{f}_0$ | Non-dimensional frequency center of synchronization range in TD VIV model |
| $\hat{f}_{exc,y}$ | Non-dimensional vortex-induced excitation frequency in TD VIV model |
| $\hat{f}_{range}$ | Non-dimensional frequency synchronization range in TD VIV model |
| $\alpha$ | Parameter restricting the instantaneous frequency of in-line motion in TD VIV model. Note: might also refer to the phase difference between the cross-flow and in-line motion in the forced oscillation experiments with strakes by Senga |
| $\alpha_1$ | Mass proportionality constant for Rayleigh damping |
| $\alpha_2$ | Stiffness proportionality constant for Rayleigh damping |
| $\ddot{\mathbf{r}}$ | Nodal acceleration vector in the dynamic equilibrium equation |
| $\dot{\mathbf{r}}$ | Nodal velocity vector in the dynamic equilibrium equation |
| $\mathbf{C}$ | Damping matrix in the dynamic equilibrium equation |
| $\mathbf{K}$ | Stiffness matrix in the dynamic equilibrium equation |
| $\mathbf{M}$ | Mass matrix in the dynamic equilibrium equation |
| $\mathbf{r}$ | Nodal displacement vector in the dynamic equilibrium equation |
| $\mathbf{R}^E$ | External force vector in the dynamic equilibrium equation |
| $\Delta\hat{f}$ | Amplitude from center to boundaries of synchronization range in TD VIV model |
| $\Delta t$ | Time-step in numerical time domain integration |
| $\dot{\phi}_{exc,x}$ | Instantaneous frequency of the in-line vortex-induced excitation force in the TD VIV model |
| $\dot{\phi}_{exc,y}$ | Instantaneous frequency of the cross-flow vortex-induced excitation force in the TD VIV model |
| $\eta$ | Suppression efficiency of for vortex-induced vibration suppression devices |
| $\kappa_y$ | Curvature about local element y-axis |
| $\kappa_z$ | Curvature about local element z-axis |
| $\nu$ | Kinematic viscosity of fluid |

| | |
|---|---|
| $\omega_n$ | Eigenfrequency of mode n |
| $\phi_{\dot{x}_{rel}}$ | Instantaneous phase of the relative in-line velocity of the structure in TD VIV model |
| $\phi_{\dot{y}_{rel}}$ | Instantaneous phase of the relative cross-flow velocity of the structure in TD VIV model |
| $\phi_{exc,x}$ | Instantaneous phase of the in-line vortex-induced excitation force in TD VIV model |
| $\phi_{exc,y}$ | Instantaneous phase of the cross-flow vortex-induced excitation force in TD VIV model |
| $\rho$ | Density of fluid |
| $\sigma_{disp}$ | Standard deviation of displacement. Relevant for presentation of displacement results |
| $\theta$ | Instantaneous phase difference between the structure's relative cross-flow velocity and the cross-flow excitation force in TD VIV model |
| $A/D$ | Amplitude to diameter ratio. Describes VIV response |
| $C_A$ | Non-dimensional added mass coefficient |
| $C_D$ | Non-dimensional drag coefficient |
| $C_L$ | Non-dimensional lift coefficient |
| $C_M$ | Non-dimensional inertia coefficient |
| $C_{d,y}$ | Damping coefficient for early version of TD VIV cross-flow model |
| $C_{Df}$ | Surface skin friction drag coefficient. Related to the tangential drag coefficient |
| $C_{v,x}$ | vortex-induced in-line excitation force coefficient for TD VIV model |
| $C_{v,y}$ | vortex-induced cross-flow excitation force coefficient for TD VIV model |
| $D$ | Diameter of riser |
| $f_n$ | Natural frequency of structure |
| $f_s$ | Vortex shedding frequency |
| $f_{n0}$ | Still water natural frequency of structure |
| $f_{osc}$ | Oscillation frequency of structure |
| $H/D$ | Strakes height to diameter ratio. Describes strakes geometry |
| $KC$ | Keulegan-Carpenter number |
| $N$ | Number of strakes |
| $P/D$ | Strakes pitch to diameter ratio. Describes strakes geometry |
| $R_e$ | Reynolds number |
| $S_t$ | Strouhal number |
| $T$ | Wave period. Related to the KC number |

| | |
|---|---|
| $U$ | Current velocity |
| $U_R$ | Reduced velocity |
| $v_m$ | Maximum particle velocity. Related to the KC number |
| $\psi_n$ | Mode shape of mode n |

# List of acronyms

| | |
|---|---|
| CF | Cross-flow |
| IL | In-line |
| CFD | Computational Fluid Dynamics |
| CRS1 | Cross-section type 1 in Riflex |
| CRS2 | Cross-section type 2 in Riflex |
| DFT | Discrete Fourier Transform |
| DoF | Degree of Freedom |
| FEM | Finite Element Method |
| LGS | Longitudinal Grooved Suppression |
| MIT | Massachusetts Institute of Technology |
| MsC | Master of Science |
| NCS | Norwegian Continental Shelf |
| NDP | Norwegian Deepwater Program |
| SCR | Steel Catenary Riser |
| std | Standard deviation |
| TD VIV Model | Time Domain Vortex-Induced Vibration Model |
| VIM | Vortex-Induced Motions |
| VIV | Vortex-Induced Vibrations |

# Contents

# List of figures

# List of tables

# Chapter 1

# Introduction

## 1.1 Background

Slender marine structures such as risers, umbilicals and mooring lines are exposed to oscillating forces when placed in a flowing fluid. These oscillating forces cause the vortex-induced vibrations (VIV) phenomenon which can lead to fast accumulation of fatigue damage. To be able to predict the stresses in slender marine structures under these conditions is hence of great significance for determining their expected lifetime and avoid premature structural failure.

A large amount of research has been done on VIV, and much of it is reflected over in the DNV GL VIV Best Practice [1]. Research is needed in order to better understand VIV, and research experiments are essential for establishing empirical hydrodynamic added mass, drag and excitation coefficients which are the foundation of the most common prediction tools today: the semi-empirical VIV models. In the industry the semi-empirical frequency domain prediction tools dominate, such as VIVANA, VIVA and SHEAR7. These have the drawback that they can only consider stationary flow and linear structures, as the dynamic equilibrium equation is solved in the frequency domain.

In recent years it has been proposed time domain prediction tools which are not restricted by non-linearities as time-varying flow, geometric stiffness and contact-conditions which limits the frequency domain tools. One of these tools is the semi-empirical time domain VIV model (TD VIV model) developed at NTNU by the PhDs Mats Jørgen Thorsen [2] and Jan Vidar Ulveseter [3], which is based on a synchronization load model of the vortex-induced forces. When coupled to a finite element model (FEM) it has been shown that the model is capable of predicting the VIV response of slender elastic structures in uniform, shear and oscillating flow([4], [5]), as well as in conditions with combined current and irregular waves [6]. Other existing tools are computational fluid dynamics (CFD) and wake oscillator models. As CFD is extremely computationally demanding and determining the parameters for the wake oscillator model is complicated in order to obtain good predictions, these methods are not common for the design of slender marine structures today.

## 1.2 Objectives

In the offshore industry it has for a long period been common to fit marine risers with suppression devices such as strakes and fairings in order to reduce VIV and overcome the issue of early fatigue failure. VIVANA [7] offers prediction of VIV response for risers with helical strakes. The present work aims at including the same feature to a model combining the TD VIV model and a Morison load model in the Finite Element (FE) software Riflex. The Norwegian Deepwater Programme (NDP) High Mode VIV tests [8], which include tests of bare risers and partially and fully straked risers in uniform and shear flow, are used for evaluation of the model.

## 1.3 Thesis structure

This thesis is organized with the following outline:

**Chapter 2** provides a literature review of the VIV knowledge relevant for the thesis.

**Chapter 3** presents the development of the hydrodynamic load model and the numerical and structural model, as well as issues and observations made during the thesis work. In addition a presentation of the tools used for assessing the model performance is given.

**Chapter 4** describes the Norwegian Deepwater Programme (NDP) High Mode VIV tests, and sets of relevant tests are chosen for benchmarking of the model.

In **Chapter 5** the results of the simulations with both bare and partially straked risers compared to the experimental results are presented.

**Chapter 6** summarizes the key findings, concludes and gives recommendations for further work.

# Chapter 2

# Vortex-induced vibrations

A literature review on vortex-induced vibrations (VIV) is presented in order to provide the relevant knowledge for this master's thesis. First, the fundamental concepts of VIV are presented before more specific theory is covered, such as experimental VIV research, methods for VIV suppression and existing tools for VIV prediction. At last the development of the TD VIV model and Morison load theory are dealt with. A large portion of the VIV theory covered in this thesis is based on DNV GL VIV Best Practice [1], while smaller parts are taken from other sources which are all referred to.

## 2.1 Fundamental VIV theory

### 2.1.1 Vortex shedding

To illustrate the concept of vortex shedding the fixed circular cylinder exposed to a uniform and stationary fluid flow shown in Figure 2.1 is considered. Sufficiently far away from the cylinder surface the flow can be considered undisturbed by the presence of the cylinder and potential theory applies. But close to the cylinder surface viscous forces cause a boundary layer which separates the potential flow and the cylinder surface. At the surface of the fixed cylinder the fluid velocity is zero and increases radially through the boundary layer to the velocity of the undisturbed flow. Moving along the body surface downstream of the stagnation point the pressure gradient becomes less and less negative which causes a retardation of the fluid close the surface. At some point the pressure gradient becomes positive and this point is referred to as the separation point. A shear layer is formed due to the flow separation and in turn creates a vortex downstream of the separation point. This phenomenon occurs on both the lower and upper side of the cylinder, so that vortices are shed from both sides of the cylinder, but with different directions of vorticity.

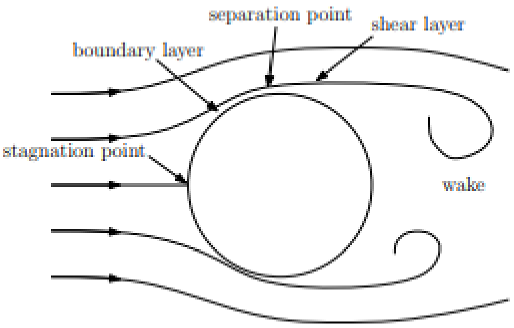

Figure 2.1: Flow around a fixed circular cylinder

In order to classify the flow past a circular cylinder it is common to use the Reynolds number:

$$R_e = \frac{U \cdot D}{\nu}, \tag{2.1.1}$$

where $U$ is the velocity of the incoming flow relative to the cylinder, $D$ is a characteristic length which for a cylindrical structure is equal to the cylinder diameter and $\nu$ is the kinematic viscosity of the fluid. It is commonly accepted to divide the flow regimes by the magnitude of the Reynolds number and according to Greco [9] the different regimes are given as follows for flow past smooth circular cylinders:

- Sub-critical flow regime: $R_e \lessapprox 2 \cdot 10^5$.
- Critical flow regime: $2 \cdot 10^5 \lessapprox R_e \lessapprox 5 \cdot 10^5$.
- Super-critical flow regime: $5 \cdot 10^5 \lessapprox R_e \lessapprox 3 \cdot 10^6$.
- Transcritical flow regime: $3 \cdot 10^6 \lessapprox R_e$.

Note that some literature refers to the post-critical flow regime, which covers both super-critical and transcritical flow. The typical vortex shedding pattern created behind a fixed rigid cylinder as a function of the Reynolds number is shown in Figure 2.2.

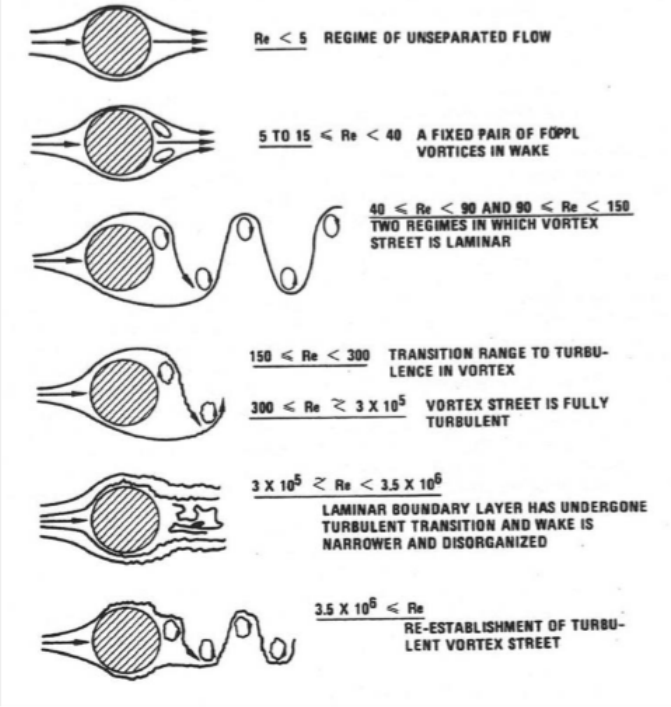

Figure 2.2: Vortex shedding pattern behind a smooth fixed cylinder as a function of $R_e$

For $Re > 5$ vortex shedding occurs: at first in pairs, but for $Re > 40$ instabilities cause the vortices to be shed alternatively from the lower and upper separation points. The frequency which the vortices are shed off from the cylinder with is simply referred to as the vortex shedding frequency $f_s$ and is for a fixed cylinder related to the Strouhal number, $S_t$, by:

$$S_t = \frac{D \cdot f_s}{U}. \tag{2.1.2}$$

It should be noted that within the lock-in region the vortex shedding frequency does not follow this relation, but locks on to a natural frequency of the structure. The lock-in phenomenon is closer investigated in Section 2.1.3.

### 2.1.2 Forces induced by vortex shedding

In general a body in a steady and uniform flow with velocity $U$ will experience a drag and lift force which will be parallel and perpendicular to the incoming flow direction. Their mean values per unit length, independent of time, can be expressed as:

$$\begin{aligned} \bar{F}_D &= \frac{\rho}{2} C_D D U^2 \\ \bar{F}_L &= \frac{\rho}{2} C_L D U^2. \end{aligned} \tag{2.1.3}$$

Here $\rho$ is the density of the fluid, $D$ is a characteristic cross-sectional length which is equal to the diameter for a circular cylinder and $C_D$ and $C_L$ are the drag and lift coefficients which are determined empirically. The mean value of the lift force is for symmetric bodies in infinite fluid equal to zero. while the mean drag force is non-zero.

When the vortex shedding has a definite periodicity, i.e. there is a single vortex shedding frequency, the body which the incoming fluid flows around will experience oscillatory forces due to the periodic changes of the pressure on the body. Hence the drag and lift force will not only have a mean component, but an oscillating component with certain amplitudes $A_D$ and $A_L$ as well. The frequency of the oscillating lift force will be equal to the vortex shedding frequency $f_s$, while the drag force will oscillate with twice the vortex shedding frequency. The reason for the different oscillation frequency for the drag force and the lift force is that the direction of the vortex-induced lift force will depend on which side of the body the vortex is shed. The side of which vortex shedding occurs does not influence the drag force. The lift and drag forces can hence be approximated by the expressions shown in Equation (2.1.4), including the fact that the lift and drag force is composed of a static and dynamic term:

$$\begin{aligned} F_D &= \bar{F}_D + A_D \cos(4\pi f_s t + \beta_D) \\ F_L &= \bar{F}_L + A_L \cos(2\pi f_s t + \beta_L). \end{aligned} \tag{2.1.4}$$

$\beta_D$ and $\beta_L$ are the phase angles of the drag and lift force, respectively.

### 2.1.3 VIV and VIM: Consequences of vortex shedding

If the body subjected to vortex-induced oscillating drag and lift forces is free to oscillate, the forces will cause oscillatory motions of the body both parallel and perpendicular to the incoming flow. The body may oscillate with its natural period and hence vortex-induced resonance may occur. The vortex-induced resonance phenomenon is generally separated into vortex-induced motions (VIM) and vortex-induced vibrations (VIV), although they refer to the same phenomenon. The reason for the separation is that VIV is associated with much higher oscillation frequency than VIM. Typically VIM is related to the rigid body motion of floating structures while VIV is related to elastic motions of structures such as rigid and flexible pipes. This thesis only treats VIV, with special focus on circular cylindrical structures.

As mentioned previously, body motions both parallel and orthogonal to the incoming flow are induced, which are referred to as cross-flow and in-line VIV, respectively. For now, only consider rigid pipes. Cross-flow VIV occurs when the oscillation frequency of the lift force $f_s$ is equal to the natural frequency $f_{n,y}$ of the structure in the direction orthogonal to the incoming flow. Correspondingly, when the drag force oscillation frequency $2f_s$ equals the in-line natural frequency $f_{n,x}$ of the structure in-line VIV occurs. It should be noted that these definitions are only used to indicate for which frequency range VIV occurs, as VIV induces lock-in. Lock-in is the phenomenon of the vortex shedding frequency locking on to the natural frequency of the structure. The reduced velocity $U_R$ is very relevant for describing lock-in and is given as

$$U_R = \frac{U}{f_n D}, \tag{2.1.5}$$

where $D$ is the diameter of the circular cylinder. To illustrate how $U_R$ is related to VIV an example of cross-flow VIV for a rigid pipe is considered. Conditions within the sub-critical flow regime are assumed, $S_t = 0.2$ and cross-flow VIV develops when the vortex shedding frequency $f_s$ is equal to the natural frequency $f_{n,y}$. It is then found, by rearranging Equation (2.1.2) and (2.1.5), that VIV occurs at $U_R \approxeq 5$. It should be noted that this value of $U_R$ is a rough estimate for when VIV occurs. This is supported by experimental results found by Vikestad [10] who studied cross-flow VIV for a circular cylinder in water. The lock-in region is seen to initiate at $U_R \approxeq 3$ and is still relevant up to $U_R \approxeq 14$, as seen in Figure 2.3. The results show that VIV occurs for a much broader region of reduced velocities than $5 < U_R < 7$ as found by Feng (1968) (according to Faltinsen [11]), which was a study of cross-flow VIV of a circular cylinder in air. This clearly indicates the effect oscillations in water will have on the natural frequency due to the change of added mass. Vikestad's results also show the effect of VIV with respect to the response amplitude: when the lock-in region is reached the amplitude increases rapidly up to values as large as about the diameter of the cylinder.

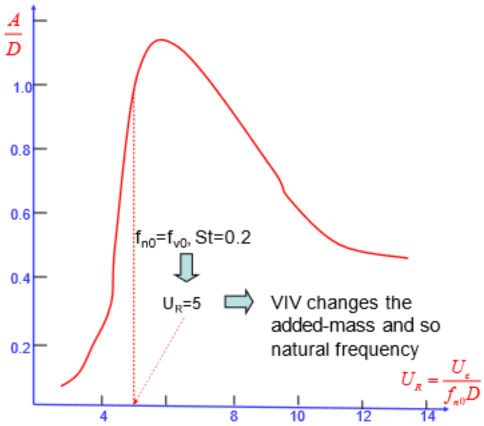

Figure 2.3: Vikestad: Cross-flow amplitude of oscillation for a rigid circular cylinder as function of reduced velocity

As in-line VIV occurs with a frequency $2f_s$, i.e. with half of the period associated with cross-flow VIV, in-line vibrations are induced at lower reduced velocities than cross-flow vibrations. These vibrations are referred to as pure in-line VIV and are particularly important for free spanning pipelines. The phenomenon is illustrated in Figure 2.4 [12] for reduced velocities from about 1 to 3. What should also be mentioned with respect to this figure is that the response amplitude associated with in-line VIV is much smaller than for cross-flow VIV.

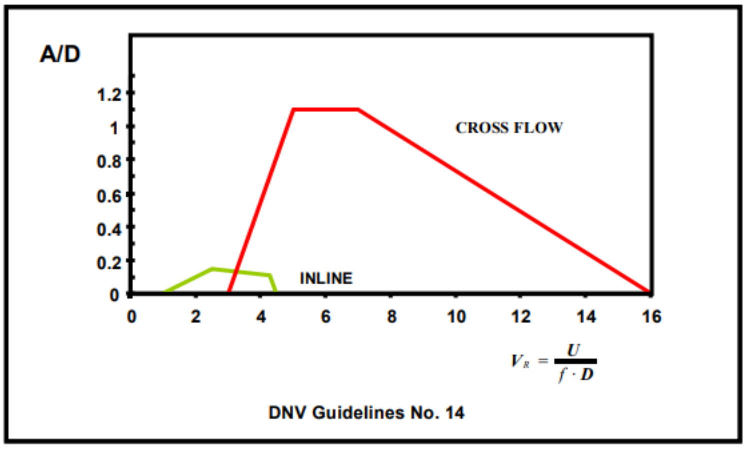

Figure 2.4: In-line and cross-flow amplitude of oscillation for circular cylinder as function of reduced velocity. Normalized by diameter

To summarize, the major consequences of VIV are given below:

- Increased oscillatory response can potentially cause rapid accumulation of fatigue damage, which over a sufficiently long time will lead to structural collapse.
- The in-line drag is amplified.

## 2.2 VIV of flexible cylinders

In Section 2.1 VIV on rigid cylinders was the main focus, but real marine risers are flexible structures and are more complex than the rigid cylinders. This is due to the spatial response variability the flexible pipes exhibit when they are exposed to hydrodynamic loads such as waves and currents. Typical experimental research related to VIV of flexible pipes is presented in Section 2.3.4, and this section is provided in advance as an introduction to the dynamic behaviour of such structures.

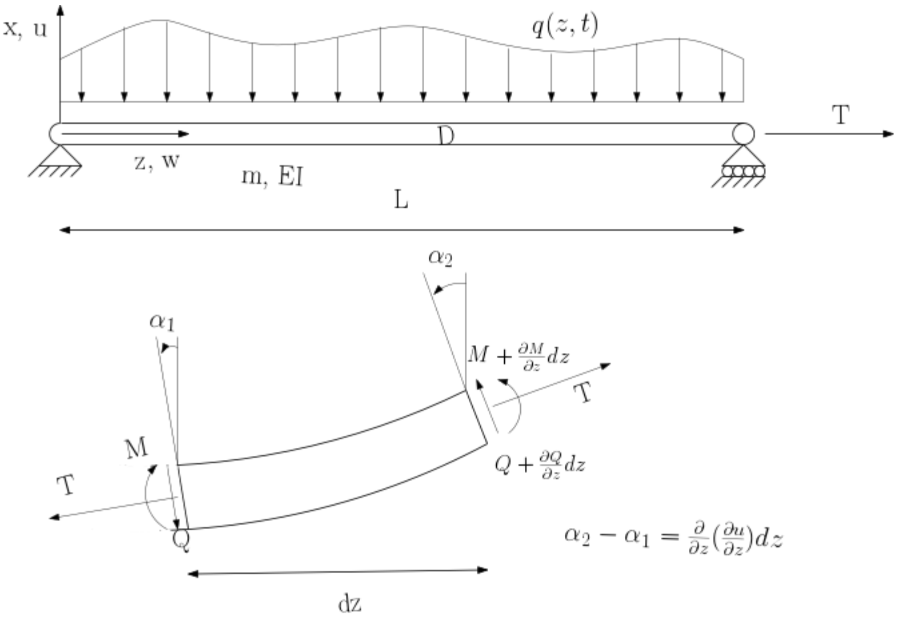

Figure 2.5: Schematic illustration of a pinned-pinned tensioned beam and the internal forces acting on a small deformed element with length $dz$

A common, but idealized, way of representing marine risers is by a pinned-pinned beam with a uniform mass distribution and constant tension $T$, bending stiffness $EI$ and diameter $D$ as illustrated in Figure 2.5. The dynamic equilibrium equation, when assuming small lateral displacements and neglecting shear deformations, is established through vertical force equilibrium for a small element with length $dz$ as seen in Figure 2.5:

$$m\frac{\partial^2 u}{\partial t^2} - T\frac{\partial^2 u}{\partial z^2} - \frac{\partial Q}{\partial z} = q(z,t). \tag{2.2.1}$$

$m$ is the cylinder mass per unit length, $u$ is the lateral displacement of the cylinder and $q$ is the arbitrary external load which might depend on the position along the pipe $z$ ($z \in [0, L]$) and the time $t$. By moment equilibrium within the segment the relation between the bending moment $M$ and the shear force $Q$ can be established. The moment can be expressed in terms of the cylinder curvature $\kappa = \frac{\partial^2 u}{\partial z^2}$ and the bending stiffness $EI$, hence the shear force can be written as:

$$Q = \frac{\partial M}{\partial z} = \frac{\partial}{\partial z}(-EI\kappa). \tag{2.2.2}$$

With this expression at hand the dynamic equilibrium equation can be rewritten by inserting Equation (2.2.2) into Equation (2.2.1):

$$m\frac{\partial^2 u}{\partial t^2} - T\frac{\partial^2 u}{\partial z^2} + EI\frac{\partial^4 u}{\partial z^4} = q(z,t). \tag{2.2.3}$$

In the case of no external loading the pipe vibrates freely. A common way of solving this type of differential equations is by separating the variables into spatial factors and time factors by modal analysis. The spatial factors are normally referred to as the mode shapes $\psi_n(z)$, and they have to satisfy the boundary conditions of the structure. The time factors $Y_n(t)$ are called modal weights. A pinned-pinned beam has moment free supports so the displacement and curvature should be zero at both ends, hence the lateral displacement $u$ can be expressed as a sum of eigen-modes:

$$u(z,t) = \sum_{n=1}^{\infty} \psi_n(z)Y(t) = \sum_{n=1}^{\infty} u_0 sin\Big(\frac{n\pi z}{L}\Big) sin\omega_n t, \quad n = 1,2,3,... \tag{2.2.4}$$

In Figure 2.6 the three first mode shapes are shown. By inserting Equation (2.2.4) into Equation (2.2.3), in the case of $q(z,t) = 0$, the natural frequencies are found:

$$\omega_n = \frac{n\pi}{L}\sqrt{\frac{T}{m} + \frac{EI}{m}\Big(\frac{n\pi}{L}\Big)^2}, \quad n = 1,2,3,... \tag{2.2.5}$$

Each natural frequency $\omega_n$ is associated with a mode shape $\psi_n(z)$, and the natural frequency increases with the mode number as seen from Equation (2.2.5). The natural frequency has one term related to the tension $T$ which is linear with $n$ and another term related to the bending stiffness $EI$ which depends on $n^2$. It should be noted that the behaviour for low and high modes might be different due to the natural frequency's dependency of the mode number, as the bending stiffness becomes more important as the mode number increases. It is common to classify the structural behaviour of pipes as either tension dominated ($T$-term $\gg$ $EI$-term) or bending stiffness dominated ($EI$-term $\gg$ $T$-term). .

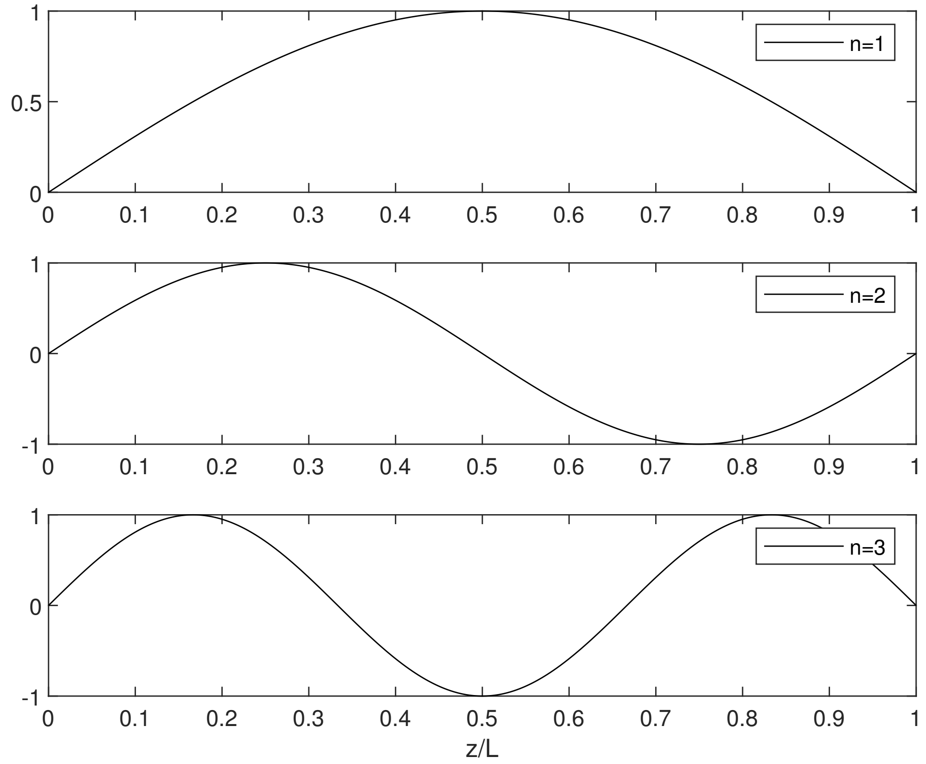

Figure 2.6: Mode shape one, two and three for a pinned-pinned flexible beam with constant tension

As flexible pipes have an infinite number of natural frequencies, the vortex shedding frequency might attach to a large range of frequencies, each with its own synchronization range. To illustrate this, consider a condition where the current velocity has been increased from 0 up to a level where the vortex shedding frequency is synchronized with the first natural frequency $\omega_1$. If the current velocity is increased more, to a level where synchronization with $\omega_1$ is no longer possible, the vibration amplitude would decrease if a rigid pipe was considered as in Section 2.1. But in the case of a flexible pipe the vortex shedding frequency might synchronize with the next natural frequency $\omega_2$, which might increase or decrease the vibration amplitude depending on the new energy transfer balance between the structure and the fluid. Lock-in and associated high amplitude vibrations is hence not limited by a reduced velocity band for flexible pipes. And VIV of flexible pipes is even more complicated than this: if the pipe is subjected to varying flow velocities along the pipe length more than one frequency may be excited and cause multi-frequency response.

In addition to the cross-flow response at the fundamental vortex shedding frequency $\omega$ and the inline response at (typically) about $2\omega$, higher harmonic response might be present for flexible pipes. Aronsen [13] measured the hydrodynamic forces on a rigid cylinder in forced oscillation tests with combined cross-flow and in-line oscillation and observed the presence of forces at multiples of the oscillation frequency: even multiples of the oscillation frequency appeared parallel to the flow and odd multiples were seen perpendicular to the flow. For flexible pipes the force contributions at multiples of the fundamental frequency will cause associated response which is referred to as higher order harmonic response. It should be noted that significant higher harmonic response is not present just as long as a flexible pipe is exposed to a incoming flow. Wu et al. [14] studied the experimental data from the Shell high mode VIV tests [15] and the Hanøytangen tests [16] in order to find out when higher harmonics occur and which factors that influence their occurrence. The study was focused on the $3\omega$ component, as this is widely recognized as the most important higher order harmonics component. The investigation showed that in many cases the third-order harmonic stress was larger than the stress associated with the fundamental cross-flow frequency. It was observed that when the response was stationary the significance of the $3\omega$ response was much larger than when the response was chaotic. For higher modes, i.e. when the contribution from bending stiffness increases, the general trend was that the response was chaotic. In order to strengthen these observations Wu et al. [17] looked into data from other experimental cases in addition to the two previously mentioned, namely the Norwegian Deepwater Programme (NDP) High Mode VIV tests [8] and the ExxonMobil rotating rig tests [18]. The study concluded that higher order VIV occur when:

- The response is stationary, i.e. not chaotic.
- The pipe is tension-dominated, i.e. the contribution from bending stiffness is low.
- The response is dominated by travelling waves.

The response of a flexible pipe can consist of both standing and travelling waves, where the response in parts of the riser is dominated by travelling waves and other parts by standing waves. In Figure 2.7 the displacement responses with standing and travelling waves of a pipe placed in a linearly sheared current of varying speed are shown. A good example of response dominated by standing waves is seen in Figure 2.7 (a). When the current speed is increased the travelling waves dominate in the part of the riser exposed to highest speed, which is illustrated in Figure 2.7 (b) and 2.7 (c). When travelling waves dominate the response, the largest response is also seen in the part of the riser exposed to highest speeds.

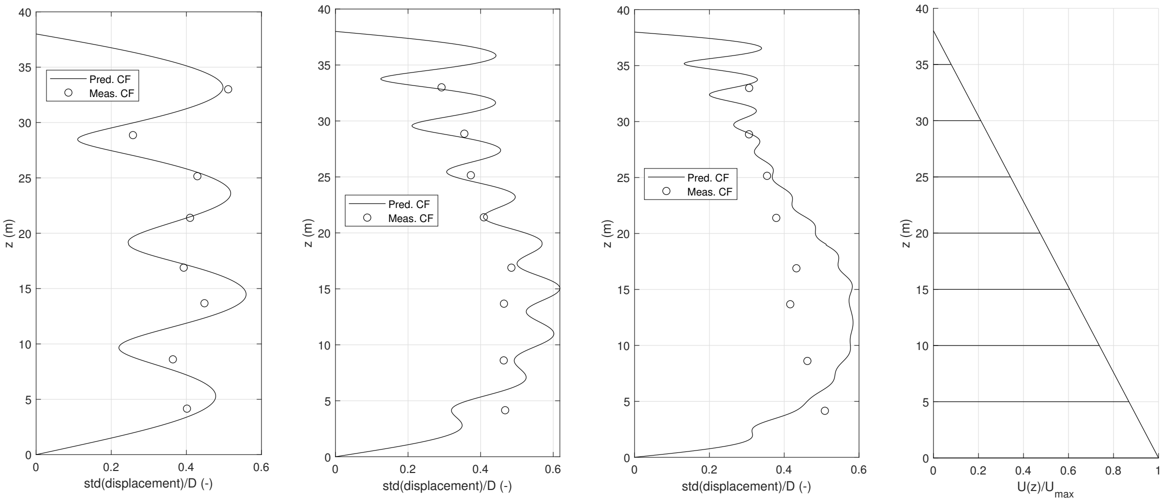

(a) $U_{max} = 0.6m/s$ (b) $U_{max} = 1.4m/s$ (c) $U_{max} = 2.2m/s$ (d) Current profile

Figure 2.7: Illustration of responses with standing and travelling waves
Lines: std of predicted cross-flow displacement response along riser. Circles: std of cross-flow displacement response along riser obtained from integration of measured accelerations from NDP tests [8]

## 2.3 VIV research

As VIV may have catastrophic consequences for slender marine structures the marine industry have spent a lot of money on research to better understand and avoid the VIV phenomenon. To perform experiments in full-scale is demanding, hence most experiments have been performed in model scale. A limiting factor when doing research in model scale is that a condition with Reynolds number outside of the sub-critical flow regime is difficult to generate in towing tanks. Real slender marine structures will be exposed of critical and post-critical flow regimes as well, which few experiments up to now have been able to investigate.

As seen in Figure 2.4 the amplitude of in-line vibrations is of much lower order than the cross-flow vibration amplitude. This is most likely the reason why most research on VIV has been on cross-flow response. Research done by Baarholm et al. [19] in large-model scale showed that the smaller amplitude of oscillations does not mean the contribution to fatigue damage is negligible from in-line VIV. Hence in-line VIV has been considered more relevant in recent years, and especially its interaction with cross-flow VIV.

The typical experiments that have been performed to improve the understanding of VIV are, according to DNV GL VIV Best Practice [1], the following:

- Rigid pipes with fixed supports.
- Free oscillations of rigid pipes on elastic supports.
- Forced oscillations of rigid pipes on elastic supports.
- Slender elastic pipes in various flow conditions.

In these experiments the pipe has typically been subjected to uniform or shear flow, i.e. stationary currents, which is logical since the most common existing VIV prediction tools are not able to predict the VIV response for pipes subjected to time-varying flow.

### 2.3.1 Rigid pipes with fixed supports

These experiments have been conducted mainly to investigate the flow pattern behind a circular pipe as a function of current speed or the Reynolds number. This includes investigating how the Strouhals number $S_t$, proportional to the vortex shedding $f_s$, depends on the Reynolds number. Naturally $S_t$ will change if strakes are fitted to the pipe, and up to today few experiments of this type have been conducted with straked pipes. For the case of a bare rigid pipe in a uniform incident flow, research [9] has shown that $S_t$ is stable and approximately equal to 0.2 within the sub-critical flow regime, independent of the surface roughness of the cylinder. The transition from laminar to turbulent flow in the boundary layer causes an increase of the vortex shedding frequency in the critical flow regime. Consequently $S_t$ is drastically increased for smooth cylinders, while small changes are seen for very rough cylinders. Pipes applied offshore are generally not smooth, as they will be exposed of marine growth and hence it is normally not needed to include the sudden increase in $S_t$ in VIV analyses. In the super-critical flow regime the importance of roughness is no longer significant, and $S_t$ returns to more or less the same level as in the sub-critical flow regime. $S_t$ as a function of Reynolds number is presented by Greco [9] and is shown in Figure 2.8, where $k/D$ is the roughness normalized by the pipe diameter.

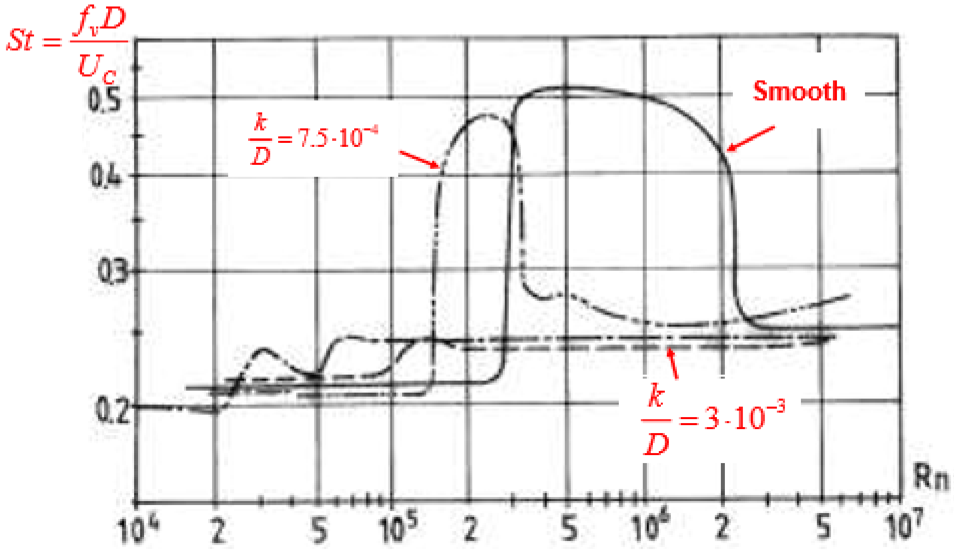

Figure 2.8: Strouhal number as a function of Reynolds number for a fixed cylinder in steady flow

### 2.3.2 Free oscillations of rigid pipes on elastic supports

These experiments are carried out by one of the three test set ups listed below, which are illustrated in Figure 2.9,

- Pure cross-flow test
- Pure in-line test
- Combined cross-flow and in-line test

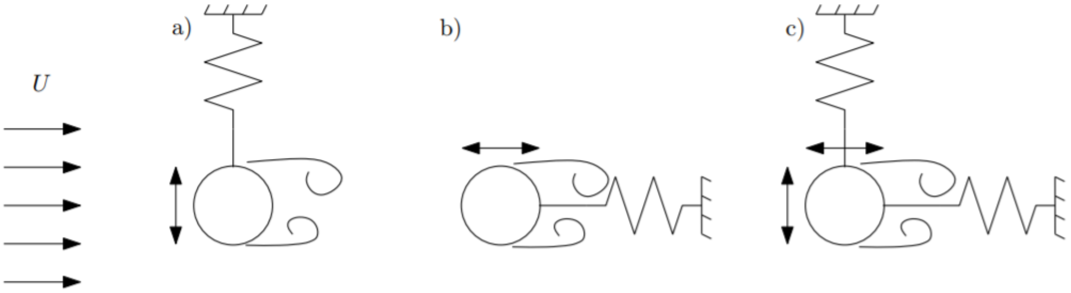

Figure 2.9: Free oscillation test types

The free oscillation experiments are conducted in order to study the VIV response, typically in terms of response amplitudes and response frequencies, and the lock-in phenomenon described in Section 2.1.3. As well the drag coefficient for the oscillating pipe is usually found. Normally these experiments are carried out for a set of current speeds. To be able to compare the wide range of experiments (different diameter, current speed, still water natural frequency, etc) of this type that has been performed, the current speed is written on its dimensionless form, i.e. as reduced velocity $U_R$. When referring to $U_R$ in these experiments one should keep in mind that it is based on the still water natural frequency.

The free oscillation experiments involves three important frequencies that need to be distinguished, and each of them should be related to a dimensionless parameter:

- Strouhals number for a fixed cylinder: vortex shedding frequency $f_s$
- Reduced velocity: still water natural frequency $f_{n0}$
- Non-dimensional frequency: oscillation frequency of the pipe $f_{osc}$

The non-dimensional frequency is expressed in terms of the pipe diameter $D$ and the current speed $U$:

$$\hat{f} = f_{osc}\frac{D}{U}. \tag{2.3.1}$$

Note that during lock-in the oscillation frequency $f_{osc}$ will be somewhere in-between the natural frequency in still water $f_{n0}$ and the vortex shedding frequency $f_s$ according to Strouhals number and corresponds to the natural frequency of the oscillating system:

$$f_{osc} = \frac{1}{2\pi}\sqrt{\frac{k}{m_d + m_a}}, \tag{2.3.2}$$

$m_d$ is the dry mass, $m_a$ is the added mass and $k$ is the stiffness of the test rig. The added mass changes when the pipe oscillates in the flowing fluid and causes the natural frequency of the oscillating system to be different from the natural frequency in still water. Added mass can be found from processing of the experimental data by considering the hydrodynamic force in phase with the pipe acceleration. Another important feature found from these experiments is that VIV is self-limiting. This is illustrated by Figure 2.10 where the pipe displacement is zero before vortex shedding is initiated. A transient response follows before steady-state is reached, i.e. a state where no energy is dissipated or provided to the system. But some force increased the displacement of the pipe gradually to the steady-state was reached, proving that the excitation force varies with the amplitude and that VIV is self-limiting.

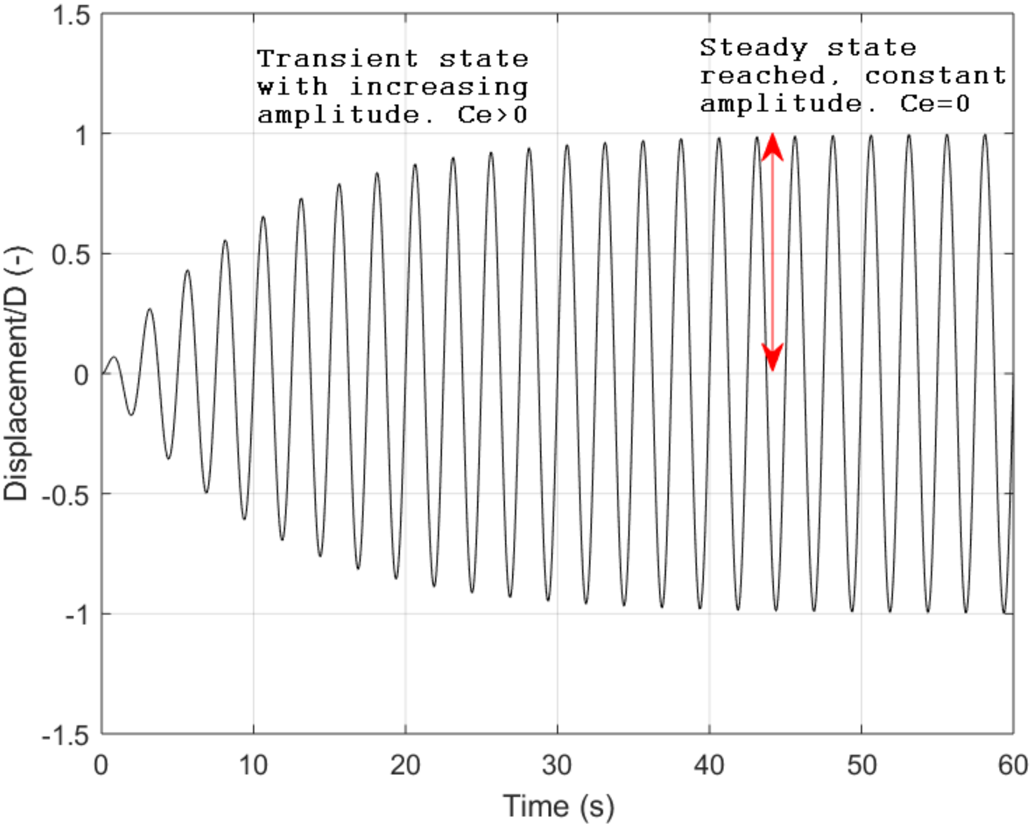

Figure 2.10: Illustration of VIV as a self-limiting process

The excitation force is 0 in the free oscillation tests after the steady-state is reached and the excitation force coefficient $C_e$ is hence normally not studied in these tests. However, some researchers have used the transient period to establish the excitation force coefficients in cross-flow and in-line direction, but generally the forced oscillation experiments are preferred when establishing both the excitation and added mass coefficients.

### 2.3.3 Forced oscillations of rigid pipes on elastic supports

In the forced oscillation experiments the pipe is placed in a constant uniform current, and the test rig does not include any springs or dampers. The pipe is forced to move in a predefined pattern: either purely in the orthogonal direction of the current, purely in in-line direction or in both directions. The experiments are illustrated in Figure 2.11, and the motion of the pipe is typically described by the simple sinusoidal functions given in the figure.

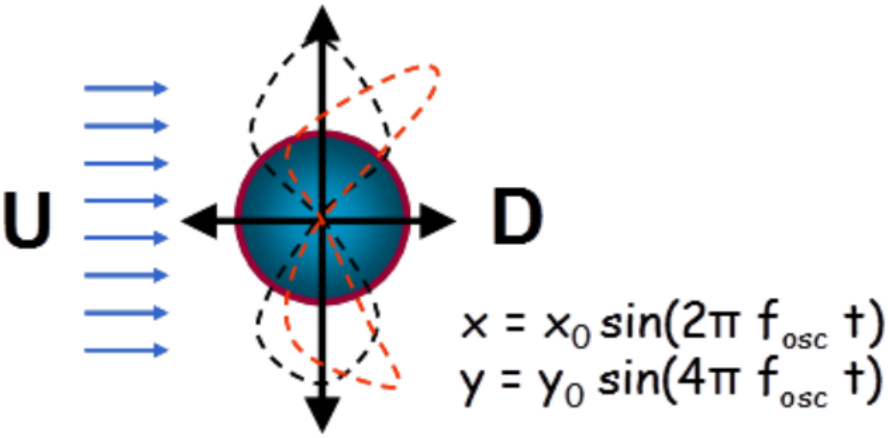

Figure 2.11: Forced oscillation experiments

The hydrodynamic forces are measured and split into a contribution in phase with the acceleration of the pipe and a contribution in phase with the pipe velocity, corresponding to the added mass and excitation forces, respectively. This makes it possible to find the added mass and excitation coefficients for any combination of oscillation frequency and vibration amplitude. Typically the results are plotted as a contour-plot with the non-dimensional frequency and the amplitude ratio $A/D$ along the axes. Examples of this can be seen in Figure 2.12, where the plots from Aronsen [13] of in-line added mass and excitation force coefficients are shown. The bold black lines indicate for which combinations of amplitude and frequency there is zero excitation. Positive excitation coefficients mean the pipe is excited, while for negative excitation coefficients energy is dissipated from the pipe and the pipe motions are damped. These plots are commonly used in the empirical VIV prediction tools, see Section 2.5, to map the excitation zone.

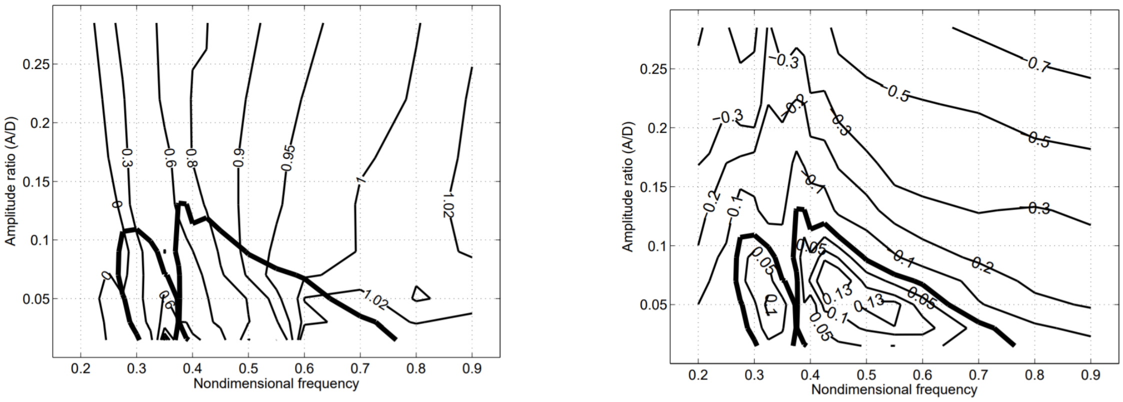

(a) Added mass coefficient

(b) Excitation force coefficient

Figure 2.12: Contour plots of the in-line added mass and excitation force coefficients from Aronsen

### 2.3.4 Slender elastic pipes in various flow conditions

The three types of experiments mentioned up to now are commonly referred to as 2D tests, but to better understand the dynamic behaviour of slender structures, experiments with free oscillations of slender flexible pipes are performed. These structures are typically scaled models of real marine structures as piles, pipelines and risers. Instead of associating the natural frequencies to the test rig as for the free oscillations of rigid pipes, the models in these experiments will have a large number of natural frequencies connected to modeshapes. Hence the structure will not have a constant amplitude along the structure, and typically the maximum amplitude along the flexible pipe is larger than for the rigid pipe. Aronsen [13] divides the experiments done on flexible pipes into three categories:

- Scaled model of piles: Cantilever beams.
- Scaled model of pipelines: Bending stiffness dominated beams.
- Scaled model of risers: Tension dominated beams.

Only the experiments with tension dominated beams will be explained here as the dynamic behaviour of marine risers is the area of interest in this thesis. The fact that the pipe is tension dominated makes excitation of more than one modeshape probable, hence higher order modes tend to appear. This in particular was investigated by Lie and Kaasen [20]. During these type of experiments the pipe is fitted with instruments such as accelerometers and strain gauges at selected positions along the pipe in order to measure the cross-flow and in-line response. Response frequencies and corresponding responding modes are calculated from modal analysis. Note that these experiments intend to model the behaviour of marine risers which are placed vertically in the water column. They are hence exposed of varying incoming flow speeds along its length. To investigate this, experiments are typically performed by exposing the scaled riser model of a shear current. Exceptions exist and for instance Chaplin et al. [21] performed experiments of a vertical tensioned riser exposed to a stepped current.

## 2.4 VIV suppression

Due to the fact that VIV cause dynamic stresses in elastic structures like flexible risers, power cables, steel catenary risers (SCR) and umbilicals, which consequently lead to fatigue damage of the structure, the need of VIV suppression devices is evaluated in the design process. Generally these devices cancel out or reduce VIV by two principles:

1. Reduce the correlation of vortices, and hence forces, along the body length.
2. Reduce the amplitude of the oscillatory forces acting on the body by reducing vortex generation and wake interaction.

So, the devices need to reduce the amplitude of the oscillatory motions, but as well the drag coefficient must be kept low and the structure should be able to deal with flow which changes direction.

The suppression devices can according to Dhanak et al. [22] be divided in active and passive devices, where the difference is simply that the active devices need energy input to control the vortex shedding while the passive devices do not need energy input. Active suppression techniques involve a way of controlling the boundary layer or the shape of the body surface to minimize VIV. These devices are expensive to integrate in a real-size slender structure and are hence rarely used in the industry. Helical strakes and fairings are the most common passive suppression devices, but other suppression devices have also been introduced by Zdravkovich [23], such as unidirectional strakes (which are only effective in one flow direction), shrouds and splitter plates. For slender structures in need of buoyancy elements, such as drilling risers, it has been proposed buoyancy elements that contribute to VIV reduction. An example of this is the LGS (Longitudinal Grooved Suppression) developed by AMOG Consulting [24], where the LGS geometry is inspired by the shape of various cacti.

### Suppression efficiency

The suppression efficiency is expressed by the maximal response amplitude to diameter ratio for the circular cylinder with and without a suppression device implemented, and is a measure of the ability of the suppression device to suppress VIV:

$$\eta = \frac{(A_{max}/D)_{bare} - (A_{max}/D)_{suppression}}{(A_{max}/D)_{bare}}. \tag{2.4.1}$$

### Helical strakes

Among all the proposed devices for reducing VIV the helical strakes are the most common. The geometry of a slender structure fitted with helical strakes is similar to a screw, as each single strake is a rectangle wrapped in a helix along the length of the structure. Tests have shown that implementing the strakes in a triple helix configuration, shown in Figure 2.13, is optimal.

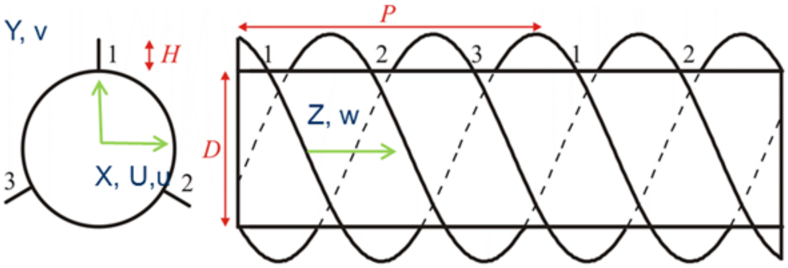

Figure 2.13: Illustration of a circular cylinder with 3 strakes with 120° separation

The geometry of the helical strakes are given by the pitch to diameter ratio (P/D) and the height to diameter ratio (H/D). The DNV GL VIV Best Practice [1] recommends, for use on risers, that the pitch is 12D-18D and the height is 0.20D-0.25D. Regarding the height of the strakes it is important that it is large enough to stick out of the boundary layer of the body. As well it has been found that the edge of the strakes need to be sharp to obtain a high suppression efficiency.

Earlier in this section the two principles for reducing VIV were introduced and helical strakes corresponds to the first, namely to alter the vortex shedding so that the oscillatory forces are uncorrelated along the length of the cylinder. This happens as flow around the body will be separated at a clear point due to the sharp edge of the strakes, but at different angular positions along the length of the body. This means the phase of the vortex shedding will be slightly different from one cross-section to the consecutive. The vortices will be shed in finite cells, and hence the amplitude of the oscillatory forces is reduced.

Strakes are very effective when it comes to reducing VIV, and experiments show that the response amplitude for some flow conditions can be reduced by 95% with full strake coverage. But this comes with a cost: the drag force on the structure is increased due to the strakes. As introduced in Section 2.1.3 the in-line drag forces increases when the slender structure vibrates, which is due to a large wake deficit is created behind the structure. The wake deficit is obviously reduced when strakes are implemented since the oscillations of the structure are significantly reduced, but anyway the drag is normally larger than it is for a structure not fitted with strakes.

An important consideration when installing strakes on a riser is how to configure the strakes. Intuitively one would think that reducing the height of the strakes would decrease the drag, but one must keep in mind that the height of the strakes must be sufficient for the VIV reduction to be effective. As well it should be evaluated which parts of the structure that should be covered with strakes. Typically it is considered whether or not it is sufficient to cover only the part of the structure exposed to the current flow with highest velocity, as this part will give the largest VIV contribution. When only parts of the structure is covered by strakes one should have transition zones between the straked and bare sections to avoid large local stresses. A transition zone is a section where the height of the strakes, i.e. the strake coverage, is gradually reduced.

### Fairings

The other important device for suppression of VIV is fairings. A fairing has a foil-shaped streamlined geometry as seen in Figure 2.14. Fairings are free to rotate about the longitudinal axis of the pipe due to the fact that the direction of the incoming flow is not constant and the fairing is most effective when its tail points downstream. It adjusts itself automatically as the direction of the incoming flow changes. If the fairings are not free to rotate, but are locked to the pipe, they will not align with the incoming flow and a steady lift will be introduced as well as increased drag forces.

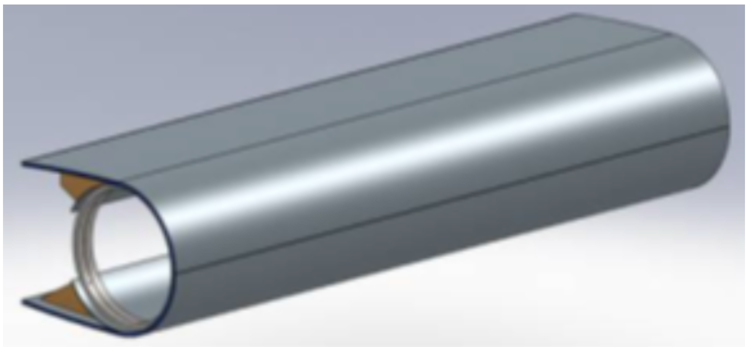

Figure 2.14: Illustration of fairings for a circular cylinder

Fairings are based on the second principle for reducing VIV, i.e. reducing the vortex generation and wake interaction by its streamlined geometry. According to DNV GL VIV Best Practise [1], experiments have proven that fairings are very effective for VIV suppression in both the sub-critical and the critical flow regime. Actually the fairings have some characteristics that surpass those of strakes, such as a lower drag and a lower influence from marine growth. On the other hand instability oscillations at high reduced velocities might be induced due to poor design of the fairing. This phenomena is called galloping and is, in contrast to lock-in, not self-limiting and may cause failure of the structure.

## 2.5 VIV prediction tools

To predict VIV has been important within the offshore industry for a long time. In general, for the prediction of VIV it is essential to establish:

1. A mathematical model able to represent the structural response due to the given hydrodynamic forces acting on the structure. Typically the finite element method (FEM) is applied for this, where non-linear FEM allows the user to deal with non-linearities such as large displacements, time-varying geometric stiffness and non-linearities related to the boundary conditions.
2. A hydrodynamic model capable of calculating the loads on the structure, which will be dependent of the structure motion.

Various methods for predicting the hydrodynamic loads exist. Typically the methods are divided in three types:

- Computational Fluid Dynamics - CFD.
- Wake oscillator models.
- Semi-empirical models.

CFD is very computationally demanding and to perform a full analysis takes a lot of time. For most problems the computational costs are too large for other than very strong computers, and for practical engineering it is not suitable at the moment. Nevertheless, it should be mentioned that the method, solving the Navier-Stokes equation for the flowing fluid around the relevant structure, is promising with respect to VIV prediction.

Another prediction method is the wake oscillator model, which operate in the time domain, and is described by Facchinetti et al. [25]. The method is based on modelling the wake dynamics by the van der Pol equations in order to describe vortex shedding. It is also an empirical model where the necessary parameters in the model are found from experimental results. Most of these models have been based on only free oscillation experiments, while Ogink and Metrikine [26] tried to establish a model able to reproduce the experimental results of both free and forced oscillations. It was found that establishing a set of frequency dependent parameters was very difficult in order to make the model conform to both free and forced oscillations.

The last type of prediction tools is also the type most commonly used by engineers up to today, namely the semi-empirical models. Most of these prediction tools perform the analysis in the frequency domain, but in recent years promising methods for time domain prediction of VIV have been proposed, such as the one by Mainçon [27] and the one by Thorsen et al. [2]. Mainçon's method involves applying an artificial neural network which predicts the instantaneous hydrodynamic forces by using the compressed information from the recent velocity history. Thorsen does on the other hand base his prediction tool on a synchronization model that simulates how the excitation force and the structure motion synchronize in order to obtain lock-in.

### 2.5.1 Semi-empirical frequency models

Various semi-empirical frequency domain prediction tools exist today. SHEAR7, VIVANA and VIVA, distributed by AMOG Consulting, SINTEF Ocean and MIT, respectively, are the three most used tools. DNV GL VIV Best Practice [1] provides an illustration of the various VIV prediction tools, and this is shown in Figure 2.15 where the properties of the three mentioned frequency domain tools are indicated. The common feature for these tools is that they consist of two parts; one part containing a fluid-structure interaction model, consisting of a fluid force model and the dynamic equilibrium equations, and a second part containing a database of hydrodynamic cross-section coefficients. The structural modelling is done by analytical functions, finite elements or finite differences. The hydrodynamic coefficients (added mass, drag and excitation) are established from the experiments described in Section 2.3.2 and 2.3.3. Which values that are picked from the database of hydrodynamic coefficients depend on the frequency (typically given by the non-dimensional oscillation frequency) and amplitude of oscillation for each cross-section. From the fluid properties, the cross-sectional hydrodynamic parameters and the cross-section geometry the forces on each cross-section are found.

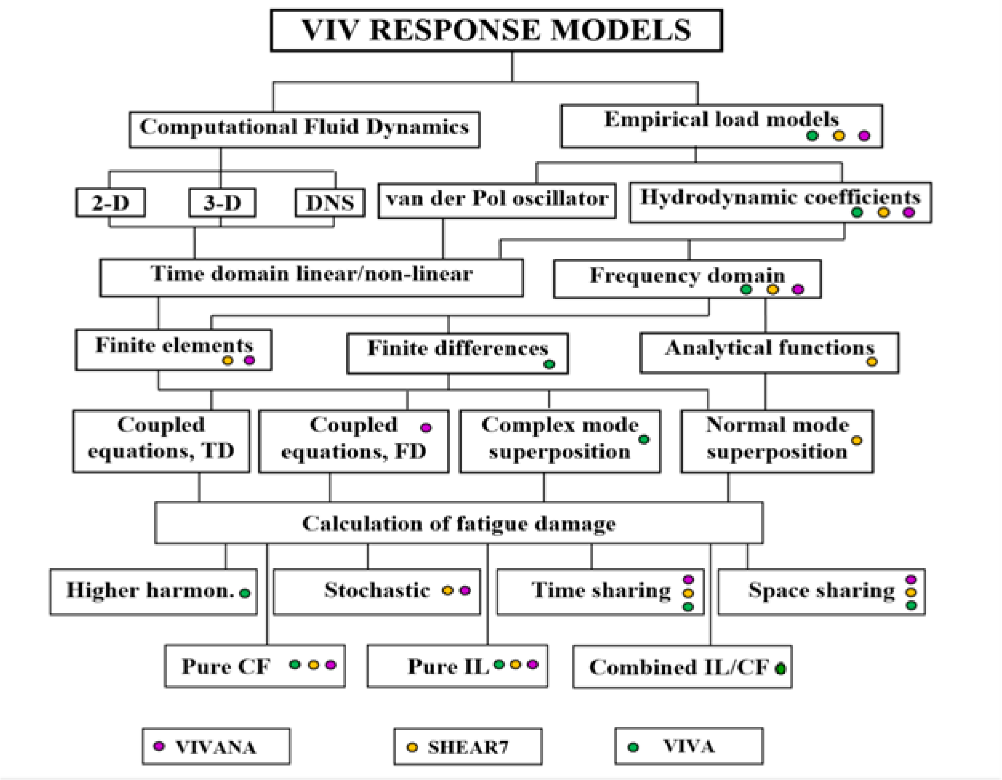

Figure 2.15: Illustration of the available VIV prediction tools

The semi-empirical frequency domain tools are useful for many analyses, but they are also limited. Due to the formulation that only allows stationary and harmonic response in the frequency domain the structural model is required to be linear. As well, the incoming flow must be stationary which means that VIV caused by waves cannot be predicted by these tools. For cases where the incoming velocity varies much along the riser the interaction between different frequency responses might be significant, but this is difficult to account for with these tools. Observe from Figure 2.15 that only VIVA can account for the interaction between cross-flow and in-line VIV. To overcome the limitations concerning non-linearities, a method performing step-wise numerical integration of the dynamic equilibrium equation in the time domain would be preferred, and the VIV synchronization model first proposed by Thorsen et al. [4] is promising in regard to accomplishing this.

### 2.5.2 Synchronization time domain model - The TD VIV model

The key element of this model is the formulation of a synchronization model for the vortex-induced excitation forces. Strip theory is used, meaning that hydrodynamic forces on a cylinder cross-section are found from the velocities and accelerations from that particular cross-section. The reference frame used is illustrated in Figure 2.16, with a right-handed coordinate system with origin in the static equilibrium position, is used: the x-axis points in the in-line direction, the y-axis points in the cross-flow direction and the z-axis points out of the plane parallel to the cylinder axis. $U$ is the velocity of the incoming flow, $\dot{x}$ and $\dot{y}$ are the cross-flow and in-line velocities of the cross-section and $\ddot{x}$ and $\ddot{y}$ are the cross-flow and in-line accelerations of the cross-section.

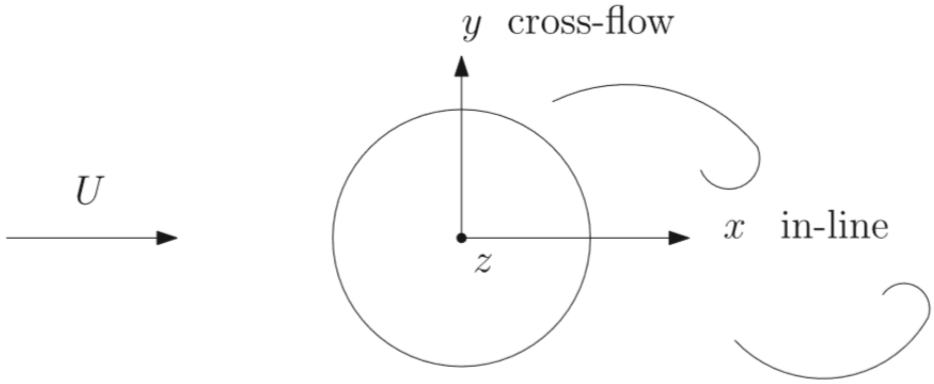

Figure 2.16: Definition of the coordinate system for the TD VIV model

In order to establish a hydrodynamic force model, Thorsen has investigated various models ([4], [5], [28], [29]). The first papers where the TD VIV model was introduced, considered pure cross-flow VIV with a hydrodynamic force model on the form:

$$F_y = F_{exc} + F_{damping} + F_{add} = \frac{1}{2}\rho D U^2 C_{v,y} \cos\phi_{exc,y} - \frac{1}{2}\rho D C_{d,y}|\dot{y}|\dot{y} - \rho\frac{\pi D^2}{4}C_A\ddot{y}, \tag{2.5.1}$$

where the first term is the excitation force, the second term is the damping force and the last term is the added mass force. A similar model was used by Ulveseter et al. [30] considering pure in-line VIV. $D$ is the diameter of the cylinder, $U$ is the velocity of the incoming flow, $C_{v,y}$ is the vortex-induced cross-flow excitation force coefficient, which is a function of the cross-flow amplitude ratio $\frac{y_0}{D}$. $\rho$ is the density of the fluid, $C_{d,y}$ is the damping coefficient, $C_A$ is the added mass coefficient, and $\dot{y}$ and $\ddot{y}$ are the cross-flow velocity and acceleration, respectively. $\phi_{exc,y}$ is the instantaneous phase of the cross-flow vortex-induced excitation force. How $\phi_{exc,y}$ is coupled to the cylinder response is an important feature of the TD VIV model and will be discussed later in this section when the most recently updated model is presented.

Note that the damping model is changed from the first paper by Thorsen et al. [4] where the damping is composed of both a linear and a quadratic term, to the model proposed by Thorsen et al. [5] presented above. This is seen to increase the accuracy of the damping model. In both cases the essence is that an equivalent damping model is established from the damping found in experiments. This is achieved by demanding that the energy dissipated over one oscillation period is equal for the equivalent damping and the damping found in experiments.

In later papers modifications of the hydrodynamic model have been made. Strip theory is still applied, and for the calculation of cross-sectional hydrodynamic forces the coordinate system and relevant variables are shown in Figure 2.17. The structural response is given by the structural motion vector **x** and the fluid velocity vector **u**.

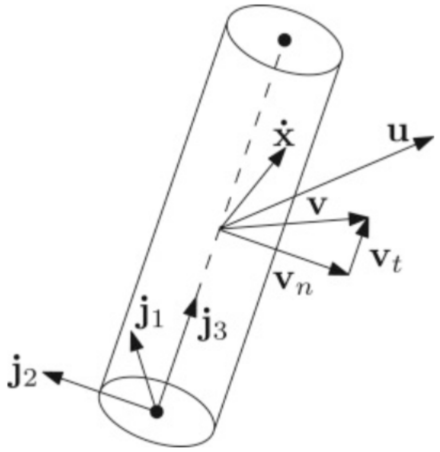

Figure 2.17: Coordinate system of cylinder segment with relevant velocity vectors

Instead of a separate damping model Thorsen et al. [29] includes the damping by the drag term in Morison's equation. Unlike in the previous papers this involves that the mean in-line drag is included. As well a non-linear FEM is implemented, providing an improved prediction tool. Note that the vortex-induced fluctuating in-line drag force is not included in this paper and that only cross-flow vibrations are considered. The total hydrodynamic damping model is given by adding the excitation force due to vortex shedding to Morison's equation:

$$\mathbf{F} = \underbrace{(C_A+1)\rho\frac{\pi D^2}{4}\dot{\mathbf{u}}_n - C_A\rho\frac{\pi D^2}{4}\ddot{\mathbf{x}}_n + \frac{1}{2}\rho D C_D|\mathbf{v}_n|\mathbf{v}_n}_{\text{Morison load terms}} + \underbrace{\frac{1}{2}\rho D C_{v,y}|\mathbf{v}_n|(\mathbf{j}_3\times\mathbf{v}_n)\cos\phi_{exc,y}}_{\text{Vortex-induced excitation term}}, \qquad (2.5.2)$$

where the Morison load terms perpendicular to the cylinder axis are:

- The first term is the inertia force due to the acceleration of the fluid particle $\dot{\mathbf{u}}_n$, where $C_A$ is the added mass coefficient equal to 1 for a circular cylinder.
- The second term is the correction of the inertia force due to the cylinder acceleration $\ddot{\mathbf{x}}_n$.
- The third term is the drag force given by the relative velocity normal to the cylinder $\mathbf{v}_n = \mathbf{u}_n - \dot{\mathbf{x}}_n$ as illustrated in Figure 2.17. $C_D$ is the drag coefficient.

The vortex-induced excitation force is perpendicular to the normal component of the relative velocity $\mathbf{v}_n$ which is continuously changed due to the vibration of the cylinder. Note that tangential forces are neglected in the expression for the cross-sectional forces $\mathbf{F}$ (in Section 3.1 it is shown how Morison's equation contains both normal and tangential terms).

**Combined cross-flow and in-line vibrations**
Up to this point the hydrodynamic models for pure cross-flow or in-line vibrations have been shown. A natural development would be a model including combined cross-flow and in-line vibrations and this is presented by Ulveseter et al. [6]. The hydrodynamic model presented here is also the model used for

the simulations in this thesis. The expression for the hydrodynamic forces per unit length acting on a strip of the cylinder is extended from Equation (2.5.2) by adding the in-line vortex-induced fluctuating excitation force and is given by:

$$\begin{aligned}\mathbf{F} = &\underbrace{(C_A+1)\rho\frac{\pi D^2}{4}\dot{\mathbf{u}}_n - C_A\rho\frac{\pi D^2}{4}\ddot{\mathbf{x}}_n + \frac{1}{2}\rho D C_D|\mathbf{v}_n|\mathbf{v}_n}_{\text{Morison load terms}} \\ &+ \underbrace{\overbrace{\frac{1}{2}\rho D C_{v,y}|\mathbf{v}_n|(\mathbf{j}_3\times\mathbf{v}_n)\cos\phi_{exc,y}}^{\mathbf{F}_{v,y}} + \overbrace{\frac{1}{2}\rho D C_{v,x}|\mathbf{v}_n|\mathbf{v}_n\cos\phi_{exc,x}}^{\mathbf{F}_{v,x}}}_{\text{Vortex-induced excitation terms}},\end{aligned} \tag{2.5.3}$$

The parameters described for Equation (2.5.2) are the same, while the parameters introduced, $C_{v,x}$ and $\phi_{exc,x}$, are the in-line vortex-induced excitation force coefficient and the instantaneous phase of the in-line vortex-induced excitation force. The directions of the vortex-induced excitation forces cross-flow and in-line, $\mathbf{F}_{v,y}$ and $\mathbf{F}_{v,x}$, are conveniently shown in Figure 2.18. The figure illustrates that the forces are normal to the cylinder axis, but how the forces will be oriented with respect to the coordinate system will depend on the normal component of the relative velocity, $\mathbf{v}_n$.

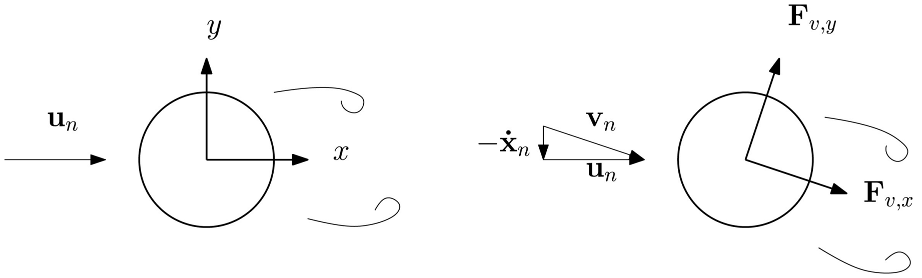

Figure 2.18: Illustration of the direction of the vortex-induced excitation forces

With the combined cross-flow and in-line TD VIV model at hand it is time to explain the synchronization model. Lock-in as a resonance phenomenon was described in Section 2.1.3 and the instantaneous phases $\phi_{exc,y}$ and $\phi_{exc,x}$ introduce lock-in to the hydrodynamic model. These will change continuously, but not at a constant rate as a consequence of the frequency of the excitation force not being constant. To explain this the cross-flow instantaneous phase $\phi_{exc,y}$ is first considered.

The rate of change of $\phi_{exc,y}$ is by Thorsen and Ulveseter referred to as the instantaneous frequency $\dot{\phi}_{exc,y}$. Generally it will be a function of the instantaneous phase difference $\theta$ between the structure's relative cross-flow velocity $\phi_{\dot{y}_{rel}}$ and the cross-flow excitation force $\phi_{exc,y}$: $\theta = \phi_{\dot{y}_{rel}} - \phi_{exc,y}$. $\phi_{\dot{y}_{rel}}$ needs to be updated at each time-step of the numerical integration and it is referred to Thorsen et al. [29] for details of how it is computed. Now the basic idea of the synchronization model is introduced. The phase difference $\theta$ indicates if the vortex shedding force or the structure velocity is "in front": for negative $\theta$ the excitation force is in front, and for positive $\theta$ the excitation force is behind. For a certain range of non-dimensional excitation frequencies $\hat{f}_{exc,y}$ the instantaneous vortex shedding force increases or decreases its frequency in order to catch up with the frequency of the cross-flow structure velocity. Only within the synchronization range energy is transferred from the fluid to the structure. Outside the synchronization range there is a negligible energy transfer between the fluid and the structure as the vortex shedding force is not able to synchronize to the structure velocity. The synchronization range is given by the center $\hat{f}_0$ and the amplitude $\Delta\hat{f}$ by: $\hat{f}_{range} = \hat{f}_0 \pm \Delta\hat{f}$. The non-dimensional excitation frequency is expressed as:

$$\hat{f}_{exc,y} = \hat{f}_0 + \Delta\hat{f}\sin\theta \tag{2.5.4}$$

and the instantaneous frequency:

$$\dot{\phi}_{exc,y} = 2\pi f_{exc,y} = 2\pi\hat{f}_{exc}\frac{|\mathbf{v}_n|}{D}. \tag{2.5.5}$$

Experiments have shown that the frequency of in-line VIV is approximately twice the cross-flow VIV frequency. This is what the in-line synchronization model first introduced by Thorsen et al. [28] is based upon. The instantaneous frequency of the in-line force $\dot{\phi}_{exc,x}$ is given in terms of the instantaneous frequency of the cross-flow force $\dot{\phi}_{exc,y}$ and the phase difference between the in-line relative velocity of the structure $\phi_{\dot{x}_{rel}}$ and the in-line excitation force $\phi_{exc,x}$:

$$\dot{\phi}_{exc,x} = 2\dot{\phi}_{exc,y}(1 + \alpha\sin(\phi_{\dot{x}_{rel}} - \phi_{exc,x})). \tag{2.5.6}$$

In order to satisfy the experimental observations, $\dot{\phi}_{exc,x} \approxeq 2\dot{\phi}_{exc,y}$, the factor $\alpha$ is set to a number much smaller than 1.

The work done by Ulveseter et al. [6] included two cases of incoming flow: one with steady uniform current, while the other involved exposing the riser of irregular waves and current simultaneously. The same set of empirical parameters were used in the two cases. The second case is of particular interest: the good results show how powerful the TD VIV model is as a prediction tool and confirm the superior applicability of this semi-empirical time domain prediction tool compared to the semi-empirical frequency domain tools when it comes to handling non-linearities.

## 2.6 Morison load theory

Morison load theory is applicable for slender structures, i.e. it is a long-wave approximation and is valid for approximately $\lambda/D \geq 5$. Here $\lambda$ is the wavelength and $D$ is a characteristic length equal to the diameter in the case of a circular pipe. Strip theory is applied as the force per unit length is calculated for small sections along the structure and integrated to find the total load. Morison's equation does not take into account diffraction effects. For less slender structures where diffraction loads matter, other load models should hence be used such as the MacCamy-Fuchs load model.

The hydrodynamic forces in the plane on a pipe section excited by a current are characterized by a tangential and normal component $f^t$ and $f^n$, given as force per unit length, which are functions of the relative velocity $\mathbf{v}_r$ between the incoming fluid velocity $\mathbf{u}$ and the structure velocity $\dot{\mathbf{x}}$, as illustrated in Figure 2.19.

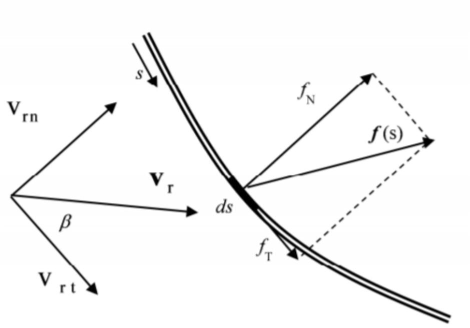

Figure 2.19: Hydrodynamic loads in the plane of a circular pipe section

Mathematically the forces $f^t$ and $f^n$ can be expressed in terms of the hydrodynamic drag and added mass coefficients for flow in tangential and normal direction:

$$f^t = \frac{\pi D^2}{4}\rho C_M^t \dot{u}_t - \frac{\pi D^2}{4}\rho C_A^t \ddot{x}_t + \frac{1}{2}\rho C_D^t D v_{rt}|\mathbf{v}_r| \tag{2.6.1}$$

$$f^n = \frac{\pi D^2}{4}\rho C_A^n(\dot{u}_n - \ddot{x}_n) + \frac{\pi D^2}{4}\rho \dot{u}_n + \frac{1}{2}\rho C_D^n D v_{rn}|\mathbf{v}_r|. \tag{2.6.2}$$

The terms in the equations above are explained in the following list:

| | |
|---|---|
| $D$ $(m)$ | Outer diameter of riser. |
| $\rho$ $(kg/m^3)$ | The density of the fluid. |
| $C_A^t$, $C_A^n$ (-) | Added mass coefficients for flow in tangential and normal direction. For a straked riser section these coefficients are related to the inertia coefficients by:<br>$C_A^t = C_M^t$ in the tangential direction, the -1 term goes away since the volume of the strakes is neglected.<br>$C_A^n = C_M^n - 1$ in the normal direction. |
| $C_D^t$, $C_D^n$ (-) | Drag coefficients in the tangential and normal flow direction. |
| $\dot{u}_t$, $\dot{u}_n$ $(\frac{m}{s^2})$ | Fluid particle acceleration components in tangential and normal flow direction. |

| | |
|---|---|
| $\ddot{x}_t$, $\ddot{x}_n$ ($\frac{m}{s^2}$) | Acceleration components of the riser section in the tangential and normal flow direction. |
| $v_{rt}, v_{rn}$ ($\frac{m}{s}$) | Relative fluid velocity components between the riser section and the incoming fluid in tangential and normal flow direction. |
| $\mathbf{v}_r$ | Relative fluid velocity .<br>$\mathbf{v_r} = \mathbf{u} - \dot{\mathbf{x}}$<br>$\lvert\mathbf{v}_r\rvert = \sqrt{v_{rn}^2 + v_{rt}^2}$ |

Note that for the 3D load case the drag force for flow out of the plane must be considered, and it is expressed equally as $f^n$ in Equation (2.6.2).

# Chapter 3

# Methodology

In this chapter the methods used for obtaining the results and conclusions of this thesis are presented. First, the hydrodynamic model is established based on the concepts presented in Section 2.5.2 and 2.6, before the theory and structure of the Finite Element (FE) software Riflex are covered. Riflex combines the hydrodynamic load model presented in Section 3.1 with a numerical model and how they are established in Riflex is described. An evaluation of the analytical formulas for the hydrodynamic coefficients for straked sections is also given. The tools for evaluating the performance of the model performance are presented, as well as the calibration of the hydrodynamic coefficients. Some observations were done during the thesis work which affected the choices of parameters in the numerical and hydrodynamic model, and these are presented and referred to as model experiences. At last the hydrodynamic coefficients for both bare and straked pipe sections for the final model are presented.

Note that the NDP High Mode VIV tests [31] were used for benchmarking in this thesis and are frequently referred to in this chapter as the NDP experiments. The NDP experiments relevant for this thesis are described in detail in Chapter 4. It is unfortunate that the experiments are referred to before being introduced, but as this chapter covers how the model was established, a model aiming at representing the NDP experiments, it was found necessary.

## 3.1 Hydrodynamic load model

To be able to predict the response in experiments with risers partially fitted with strakes, a hydrodynamic load model was needed. Different approaches were considered, and it was chosen to simply divide the riser in bare and straked segments, where either a TD VIV or Morison load model is applied. The TD VIV model was developed by Thorsen et al. [28] for bare pipes, and it is included as one of the hydrodynamic load options in Riflex alongside with Morison and MacCamy-Fuchs loading for the axi-symmetric cross-section CRS1. The modelling of straked sections is done by the Morison load model on a bi-symmetric cross-section CRS2. Hydrodynamic drag and added mass coefficients are required as input to both the TD VIV load model and the Morison load model, and how they are established is presented in this section.

### 3.1.1 Drag and added mass coefficients

With the expressions for determining the forces on slender structures at hand, presented in Section 2.5.2 and 2.6, it remains to establish the hydrodynamic load parameters such as drag and added mass coefficients. In general these coefficients are functions of the Reynolds number, the Keulegan-Carpenter number and the surface roughness of the cylinder. The Keulegan-Carpenter number $KC$ is a function of the wave period $T$, the maximum particle velocity $v_m$ and the diameter $D$ of the riser and is given as:

$$KC = \frac{v_m T}{D}. \tag{3.1.1}$$

### Coefficients for bare pipe sections

First the hydrodynamic coefficients for the bare pipe sections are considered. These are determined empirically and typically tuned to fit the measured forces. The tangential drag coefficient is caused mainly by skin friction, is small and for practical purposes set to 0. Compared to the tangential drag coefficient the normal drag coefficient is in general large. To establish it the curves presented in DNV GL RP-C205 [32] shown in Figure 3.1 may be used, where the normal drag coefficient is given as a function of the Reynolds number. One should be aware of the fact that the drag coefficient will be dependent of the KC number as well.

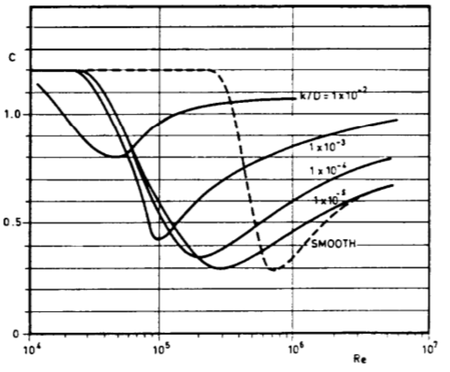

Figure 3.1: Drag coefficient for fixed circular cylinder in uniform flow for various roughness

In the tangential direction the added mass contribution is negligible when the pipe surface is assumed smooth and $C_A^t$ is typically set to 0. For a circular cross-section a typical value for the normal inertia coefficient $C_M^n$ is 2, found from potential theory, implying an added mass coefficient $C_A^n$ equal to 1.

For establishing the drag and added mass coefficients of a straked riser section DNV GL VIV Best Practice [1] presents empirical formulas, which were first introduced by Nestegård et al. [33]. These formulas are based on analyses of strakes with a triple helix configuration and are found by considering simple 2D hydrodynamic flow models. Only the normal drag coefficient is calibrated with respect to experimental results.

### Straked sections: drag coefficient for flow in tangential direction

The strakes will introduce a non-negligible drag force in the tangential direction, as each of the strakes can be considered as a thin wall on the riser surface. To establish an expression for $C_D^t$ a starting point is taken where the strakes are assumed perpendicular to the incoming flow, and two consecutive strakes are not affected by the presence of the other with respect to the incoming flow. From these assumptions an expression for the tangential drag coefficient as a function of the height to diameter ratio $H/D$, the pitch to diameter ratio $P/D$ and the number of strakes $N$ can be derived. Note that in this expression it has been accounted for the fact that the tangential velocity not necessarily will be normal to the strakes and that skin friction will contribute to the total drag coefficient. The surface skin friction component $C_{Df}$ can be set to 0.03 according to DNV GL VIV Best Practice [1].

$$C_D^t = \frac{5}{4}N\pi\frac{H}{D}\frac{D}{P}\Big(\frac{H}{D}+1\Big)\Big(\frac{1}{\sqrt{1+(P/\pi D)^2}}\Big)^3 + C_{Df}\Big(1+N\frac{H}{\pi D}\Big). \tag{3.1.2}$$

**Straked sections: drag coefficient for flow in normal direction**

The empirical formula for the drag coefficient in normal direction is based on experimental results for strakes with $H/D = 0.1$, 0.2 and $P/D = 5$, 10, 15 for Reynolds number 2000-10000. The experiments were carried out by Korkischko et al. [34]. It has been found that the the pitch to diameter ratio affects the normal drag coefficient to a small extent, hence $C_D^n$ is expressed only in terms of the drag coefficient for the bare riser $C_{D0}^n$ and the height to diameter ratio $H/D$:

$$C_D^n = C_{D0}^n\Big(1+0.7\big(\frac{H}{D}\big)+7\big(\frac{H}{D}\big)^2\Big). \tag{3.1.3}$$

Equation (3.1.3) is only valid for $H/D \leq 0.25$, which includes the recommended range of $H/D$ from 0.2 to 0.25 suggested by DNV GL [1].

**Straked sections: added mass coefficient for flow in tangential direction**

The same assumptions that were made for the derivation of the tangential drag coefficient form the basis for establishing an expression for the tangential added mass coefficient. An expression in terms of the height to diameter ratio, the pitch to diameter ratio and the number of strakes is then obtained. As was done for the tangential drag coefficient the effect of the angle of attack, i.e. the fact that in reality the tangential velocity will not be normal to the strakes, is included in the expression:

$$C_A^t = 2N\pi\Big(\frac{H}{D}\Big)^2\Big(\frac{D}{P}\Big)\frac{1}{1+(\frac{P}{\pi D})^2}. \tag{3.1.4}$$

**Straked sections: added mass coefficient for flow in normal direction**

To establish an analytic expression for the added mass coefficient in normal direction the 2D added mass coefficient $C_{A,2D}^n$ for a circular cross-section with $N \geq 3$ equally spaced strakes is used. An assumption used to obtain this expression is that the flow is normal to the strakes.

$$C_{A,2D}^n = \frac{2}{\delta^2}\left[\Big(\frac{1+\delta^N}{2}\Big)^{4/N} - \frac{1}{2}\delta^2\right]. \tag{3.1.5}$$

Here $\delta$ is a function of the diameter $D$ of the riser and the strakes height $H$:

$$\delta = \frac{1}{1+2\Big(\frac{H}{D}\Big)}. \tag{3.1.6}$$

It must be known when applying this equation that it is only valid for large values of $P/D$. Note that $C_{A,2D}^n$ only depends on the height of the strakes and not the pitch. But the effect of pitching strakes must be accounted for in the expression for $C_A^n$ and this is done by the factor $\kappa_p$:

$$\kappa_p = \frac{(\frac{P}{D})^2}{\pi^2+(\frac{P}{D})^2}. \tag{3.1.7}$$

The resulting expression for $C_A^n$ is written as:

$$C_A^n = (C_{A,2D}^n - 1)\kappa_p + 1. \tag{3.1.8}$$

## 3.2 The Riflex software

For structural analysis of slender structures such as flexible risers, power cables, mooring lines, pipelines and steel catenary risers Riflex is a powerful tool. What is common for the structures fit for analysis in Riflex is that their bending stiffness is small, as well the deflections of a slender marine structure are large, the cross-section is complex and has non-linear properties and the upper end might be exposed to large motions. Riflex is based on a non-linear finite element formulation which allows the user to analyze both the static and dynamic behaviour of a structure, including the features explained above.

### 3.2.1 Riflex theory

The finite element formulation in Riflex includes two types of elements based on small strain theory, namely a bar and a beam element. The deformation of the bar element is described by the total Lagrange formulation, while the beam element formulation is based on co-rotated ghost reference. Both formulations are based on the principle of virtual displacements. The difference between them is that in the total Lagrange formulation the initial configuration of each element is used as reference system, while in the co-rotated ghost reference each element has a reference system equal to the initial configuration that follows the element as a rigid body. The Green strain is used as strain measure, and the corresponding stress measure is the $2^{nd}$ Piola-Kirchoff stress. The bar element is a 3D-element with three translational DoFs at each of the two nodes. Rotations are included in the beam element formulation as well, hence it has three translational and three rotational DoFs at each node. The nodal DoFs of the elements are illustrated in Figure 3.2 [35].

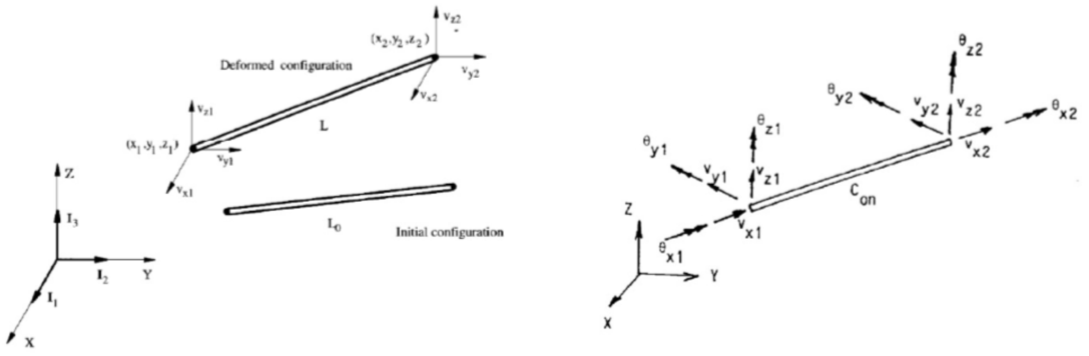

(a) Bar element

(b) Beam element

Figure 3.2: Nodal DoFs for the 2-noded Riflex bar and beam element

For the static analysis a full non-linear analysis can be performed in Riflex. In the non-linear analysis the static equilibrium must be satisfied by a complete set of nodal displacements, which in the Riflex Theory

Manual [35] is expressed by:

$$\mathbf{R}^S(\mathbf{r}) = \mathbf{R}^E(\mathbf{r}), \tag{3.2.1}$$

where $\mathbf{r}$ is the nodal displacement vector containing all the nodal degrees of freedom of the system, $\mathbf{R}^S(\mathbf{r})$ is the internal reaction force vector and $\mathbf{R}^E(\mathbf{r})$ is the external load vector. $\mathbf{R}^S(\mathbf{r})$ and $\mathbf{R}^E(\mathbf{r})$ are assembled from the force contribution from each of the elements in the system and will in general be depending non-linearly on $\mathbf{r}$. The way of solving the static equilibrium equation numerically is by applying the external loads step-wise and find the static configuration at each step by iterations. The displacement vector of the previous load step is used as the initial solution when performing iterations for the current external load vector. For the non-linear analysis the Newton-Raphson method can be applied for performing iterations, either in its true form where the incremental stiffness matrix is updated for each iteration cycle or, to reduce the computational effort, the method is modified to keep the incremental stiffness matrix constant over various iteration cycles. It can be chosen which initial configuration that will be be used for the non-linear analysis, but in practice only the stress-free configuration is used. Independent of the initial configuration the static loads on the structure must be applied in an order and by incremental steps which are defined by the user. One should be aware that the number of load steps might affect whether or not a stable static solution is reached, as well as the order of applying the loads should be chosen so that instability problems are not encountered.

Both linear and non-linear dynamic time-domain analysis are included in Riflex. These analyses involve solving the dynamic equilibrium equation, which in general is a non-linear system of differential equations given in the Riflex Theory Manual [35] as:

$$\mathbf{R}^I(\ddot{\mathbf{r}}, \mathbf{r}, \mathbf{t}) + \mathbf{R}^D(\dot{\mathbf{r}}, \mathbf{r}, \mathbf{t}) + \mathbf{R}^S(\mathbf{r}, \mathbf{t}) = \mathbf{R}^E(\dot{\mathbf{r}}, \mathbf{r}, \mathbf{t}). \tag{3.2.2}$$

In Equation (3.2.2) the internal force vector $\mathbf{R}^S$ is the same as in the static equilibrium in Equation (3.2.1), while the external force vector $\mathbf{R}^E$ now also includes forces that vary with time in addition to the static forces. $\mathbf{R}^I$ is the inertia force vector which is composed of both the structural mass forces, the added mass forces (a consequence of the acceleration of the surrounding fluid due to the presence of the structure) and the mass matrix related to an eventual internal fluid. The last term in the dynamic equilibrium equation is the damping force vector $\mathbf{R}^D$ which includes the structural damping force, the hydrodynamic damping force and the forces from eventual discrete dashpot dampers. The non-linearity of the system can be seen by the displacement dependent inertia and damping force vectors, as well as the coupling that exists between the external loads and the position and velocity of the structure.

To solve the dynamic equilibrium equation, step-by-step numerical time integration is performed. In Riflex the integration is done based on the Newmark $\beta$-family which is formulated at time t and t + $\Delta\tau$ by the following relations for the structural displacements, velocities and accelerations:

$$\begin{aligned} \dot{\mathbf{r}}_{t+\Delta\tau} &= \dot{\mathbf{r}}_t + (1-\gamma)\ddot{\mathbf{r}}_t\Delta\tau + \gamma\ddot{\mathbf{r}}_{t+\Delta\tau}\Delta\tau \\ \mathbf{r}_{t+\Delta\tau} &= \mathbf{r}_t + \dot{\mathbf{r}}_t\Delta\tau + (\frac{1}{2}-\beta)\ddot{\mathbf{r}}_t(\Delta\tau)^2 + \beta\ddot{\mathbf{r}}_{t+\Delta\tau}(\Delta\tau)^2. \end{aligned} \tag{3.2.3}$$

Here the increment $\Delta\tau = \theta\Delta t$ where $\Delta t$ is the time increment and $\theta \geq 0$. The inclusion of $\theta$ is actually a modification of the Newmark $\beta$-method called the Wilson $\theta$-method, where the Newmark $\beta$-family members correspond to $\theta$ equal to 1. It is commonly accepted that the family members corresponding to $\gamma = 1/2$ is best to use as it does not provide numerical damping. If $\beta$ is set equal to 1/4 the constant average acceleration method is applied, which is unconditionally stable. These methods are applicable for both the non-linear and linear time integration. Since non-linear dynamic analysis requires that the system mass, damping and stiffness matrices are assembled at each time step it is computationally time consuming. By linearization of the system matrices at the static equilibrium position a linearized time domain analysis can be performed, where these matrices are kept constant through the analysis. This approach is much less time consuming than the non-linear analysis, and provides a satisfactory level of accuracy for some systems. It should be noted that it most convenient when the main source of non-linearities is related to external hydrodynamic damping (which is included in the linearized analysis) and not to structural non-linearities.

This section provides a brief introduction to the theory applied in Riflex, and for better understanding of Riflex and the various analyses it is suited for, it is referred to the Riflex Theory Manual [35].

### 3.2.2 Riflex structure

In this section the several parts which constitute the Riflex program are explained. Riflex is divided into five modules, namely the INPMOD, the STAMOD, the DYNMOD, the FREMOD and the OUTMOD. To run an analysis in Riflex the user needs to define input-files for all the modules except the FREMOD module. Only the INPMOD, the STAMOD and the DYNMOD are relevant for consideration in this thesis. A simple illustration of the Riflex structure is shown in Figure 3.3 [36].

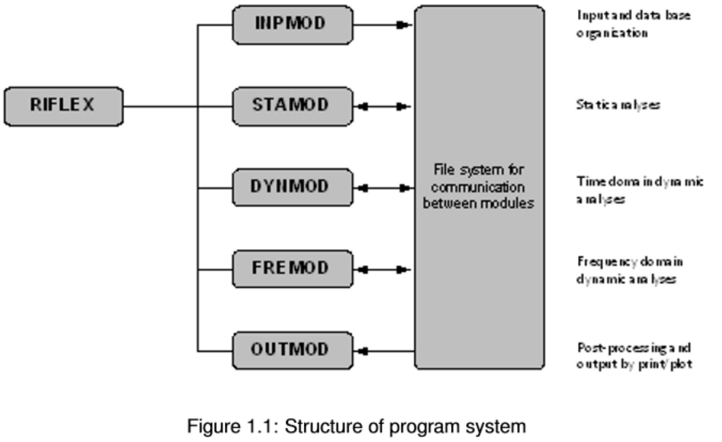

Figure 3.3: Illustration of the Riflex structure

First INPMOD will be looked into. This module reads the input data generated by the user and stores the information so that it can be used for the proceeding analyses. Hence, when the INPMOD has been run it does not need to be run again to perform the static and dynamic analyses. The input data must include all information about the geometry and orientation of the structure, the material properties, the number of elements, the boundary conditions, the loads that should be applied, the environmental conditions and so on. Establishing the input to INPMOD has been crucial in this thesis. The importance of understanding what is given as input to the analyses and how Riflex treat the information cannot be underestimated, and a considerable amount of time has been spent studying the Riflex User Manual [36] to understand the various parts of the input-file.

Static analyses are performed in STAMOD. STAMOD reads the input data stored in a database by INPMOD and generates the mesh of the structure and other necessary parameters for the static analysis.

The output from STAMOD can be used to understand the static behaviour of the structure, as well as it is used to define the initial configuration for the dynamic analysis. In this project the STAMOD input-file was, among other things, used to impose the tension in the riser by subjecting one of the end nodes of a tension force.

In DYNMOD time domain dynamic analyses are performed and dynamic responses, natural frequencies and modeshapes may be computed. These results are based on the environmental data, the static configuration given from STAMOD and other data stored in DYNMOD. The results from the dynamic analysis are stored for post-processing in OUTMOD. The input-file to DYNMOD was in this thesis used for specifying the desired output from the dynamic analysis, as well as controlling the parameters of the numerical integration.

### 3.2.3 Implementation in Riflex

In INPMOD the consistent units used throughout the Riflex analyses were set, and all input parameters in Riflex were scaled according to the definitions in Table 3.1:

Table 3.1: Units in Riflex analysis

| **Quantity** | Time | Length | Mass | Force |
|---|---|---|---|---|
| **Unit** | s | m | Mg | kN |

The riser is modelled with one super-node at each end of a line, with positions in the global coordinate system as shown in Figure 3.4. The boundary conditions were imposed by the super-nodes and were the following:

- Translations in global x- and z-direction were fixed at both ends.
- Translation in global y-direction was fixed in the upper end (y=0) and free in the lower end.
- Rotation about the global y-axis was fixed at both ends, while rotations about both the global x- and z-axis were free.

Note that the boundary conditions are not indicated in Figure 3.4 as the illustration is only meant to indicate the position of the super-nodes and the initial configuration of the riser. Also observe that the diameter/length ratio is not realistic for a slender pipe.

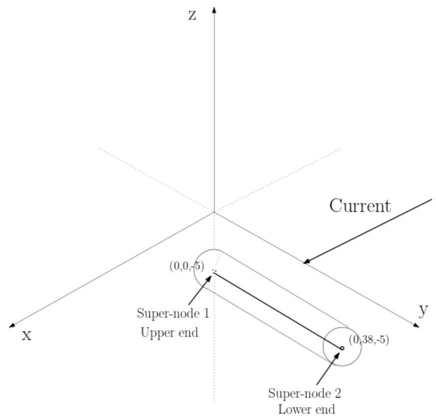

Figure 3.4: Illustration of the initial configuration and position of the riser in the global coordinate system

The mass of the test riser was modelled as if the riser was dense, i.e. the mass of the fluid inside the riser was included in the mass given as input to Riflex. The mass of the strakes was added to this mass for the straked sections.

To implement the hydrodynamic load model presented in Section 3.1 the hydrodynamic load coefficients needed to be calculated and included in the input-file to INPMOD. In the input-file it was specified which hydrodynamic load model to apply. The bare sections were modelled with the axis-symmetric CRS1 cross-section, while the straked cross-sections were modelled with the CRS2 cross-section with two symmetry planes. Illustrations of the two cross-section types with their local coordinate systems are shown in Figure 3.5. The CRS2 cross-section was chosen as an attempt to include the effect of damping by the strakes, as it includes hydrodynamic coefficients in all three local directions x, y and z. Note that all linear drag coefficients were set to zero for both the cross-section types.

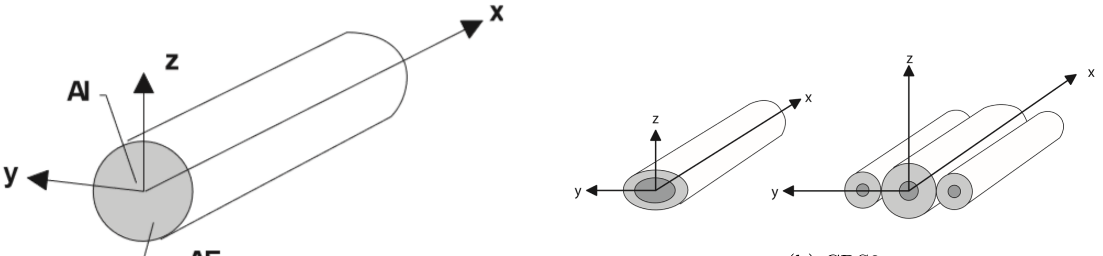

(b) CRS2

(a) CRS1

Figure 3.5: Illustrations of the applied Riflex cross-section types

### Hydrodynamic loads on bare pipe sections

As input to define the hydrodynamic loads, Riflex allows non-dimensional hydrodynamic coefficients for the CRS1 cross-section and these were found according to the explanations in Section 3.1. Only the normal quadratic drag coefficient remain to establish. For the cases in the benchmark experiment "NDP

High Mode VIV test" [31] the Reynolds number was within the sub-critical flow regime when considering a bare pipe section. From Figure 3.1, assuming the pipe is smooth, the normal drag coefficient was found to be 1.2. Sarpkaya [37] investigated the drag coefficient of rigid bare circular cylinders for low Keulegan-Carpenter (KC) numbers by experiments in a U-shaped oscillating flow tunnel. It was found that the drag coefficient was in the range 0.5 to almost 2, depending on the KC-number and the parameter $\beta = \frac{R_e}{KC}$. Note that a flexible pipe, which will vibrate both cross-flow and in-line, is considered in this thesis. Figure 3.1 and the results from [37] are based on the flow around rigid pipes and have hence served as rough estimates. The initial value of the drag coefficient, prior to calibration, was set to 1.2 based on these.

### Hydrodynamic loads on straked pipe sections

The non-dimensional hydrodynamic coefficients for the straked sections were computed by use of the equations presented in Section 3.1. But for the CRS2 cross-section, Riflex does not allow the user to give non-dimensional coefficients as input. Instead they must be given on the form specified by Riflex, and the coefficients are given below with the same notation as used in the Riflex User Manual [36]. The quadratic drag coefficients $CDX$, $CDY$ and $CDZ$ were established by:

$$\begin{aligned} CDX &= \frac{1}{2}\rho S_{2D} C_{dx} \\ CDY &= \frac{1}{2}\rho B_y C_{dy} \\ CDZ &= \frac{1}{2}\rho B_z C_{dz}. \end{aligned} \tag{3.2.4}$$

$S_{2D}$ is the cross-sectional wetted surface taken as $\pi D$, $B_y$ and $B_z$ are the projected areas per unit length in the y- and z-direction taken as the sum of the outer diameter of the riser and the height of one strake, $D + H$. $C_{dx}$, $C_{dy}$ and $C_{dz}$ are the non-dimensional drag coefficients and $\rho$ is the fluid density.

The added mass coefficients $AMX$, $AMY$ and $AMZ$ for the CRS2 cross-section must have unit mass per length and were computed by:

$$\begin{aligned} AMX &= \rho A C_{mx} \\ AMY &= \rho A C_{my} \\ AMZ &= \rho A C_{mz}. \end{aligned} \tag{3.2.5}$$

Here $A$ is the outer cross-sectional area of the bare riser, $\pi\frac{D^2}{4}$. The presence of strakes was neglected in the calculation of the added mass coefficients, as the total cross-sectional area of strakes was about 4% of $\pi\frac{D^2}{4}$. $C_{mx}$, $C_{my}$ and $C_{mz}$ are the non-dimensional added mass coefficients.

As well the tension in the riser needed to be included in the model. As the two ends of the riser represent conditions that are relatively difficult to model exactly, springs and other components were simply replaced by a tension applied as a constant specified force (in STAMOD) in the lower end of the pinned-pinned beam, see Figure 2.5. The tension applied in the simulations was the mean effective tension measured at the riser ends during the steady-state period of each of the benchmark experiments.

In the NDP experiment the riser was exposed to a current and no waves, hence the wave amplitude, required as input to INPMOD, was set very small. The current was either uniform or sheared and was moving in the positive global x-direction as seen in Figure 3.4.

## 3.3 Validation of strakes coefficients

As stated by Nestegård et al. [33] the formulations of the hydrodynamic coefficients for the straked pipe sections presented in Section 3.1.1 remain to be experimentally validated. From these formulations the following hydrodynamic coefficients were found for the strakes used in the relevant NDP experiments ($P/D = 17.5$, $H/D = 0.25$ and $N = 3$), assuming a normal drag coefficient for bare pipe equal to 1.2:

Table 3.2: Non-dimensional hydrodynamic coefficients for straked riser section

| **Parameter** | **Magnitude** |
|---|---|
| Drag coefficient for flow in tangential direction [-] | 0.0383 |
| Drag coefficient for flow in normal direction [-] | 1.9350 |
| Added mass coefficient for flow in tangential direction [-] | 0.0021 |
| Added mass coefficient for flow in normal direction [-] | 1.5078 |

Note that the coefficients for flow in tangential direction corresponds to $C_{dx}$ and $C_{mx}$ presented in Section 3.2.3. The coefficients for flow in normal direction, i.e. local y- and z-direction, corresponds to $C_{dy} = C_{dz}$ and $C_{my} = C_{mz}$ as the analytical formulas do not distinguish cross-flow and in-line.

In order to evaluate the validity of the equations for estimating the hydrodynamic coefficients for flow in normal direction for straked pipe sections, the work by Senga et al. [38] was considered. He performed forced oscillation tests in the sub-critical regime in order to obtain hydrodynamic coefficients for two types of straked cylinders, where one of the strakes geometries was identical to the strake geometry considered in this thesis: pitch to diameter ratio $P/D = 17.5$, height to diameter ratio $H/D = 0.25$ and $N = 3$ strakes. In the experiments the cross-flow amplitudes were twice the in-line amplitudes ($\frac{A_{CF}}{A_{IL}} = 2$), the in-line oscillation frequencies were twice the cross-flow oscillation frequencies ($\frac{f_{CF}}{f_{IL}} = 0.5$) and a phase difference $\alpha = [0, 45, 90, ..., 315, 360]$ between the cross-flow and in-line motions was applied (Note: this $\alpha$ must not be confused with the $\alpha$ in the TD VIV model). Different motion amplitudes and oscillation frequencies were applied, and the resulting drag and added mass coefficients with non-dimensional cross-flow oscillation frequency $\hat{f}_{osc} = 0.147$ are shown as function of the phase difference $\alpha$ in Figure 3.6. This oscillation frequency was very close to the center frequency $\hat{f}_0 = 0.144$ of the synchronization region of the TD VIV load model and was hence found most relevant. Recall that, as explained in Section 3.1, the TD VIV load model applies for bare sections, but it was assumed that the excitation in the bare sections will dominate the response also in the straked sections as energy travels along the pipe. It was hence fair to assume the strakes will oscillate with a non-dimensional frequency about 0.144 in the Riflex simulations.

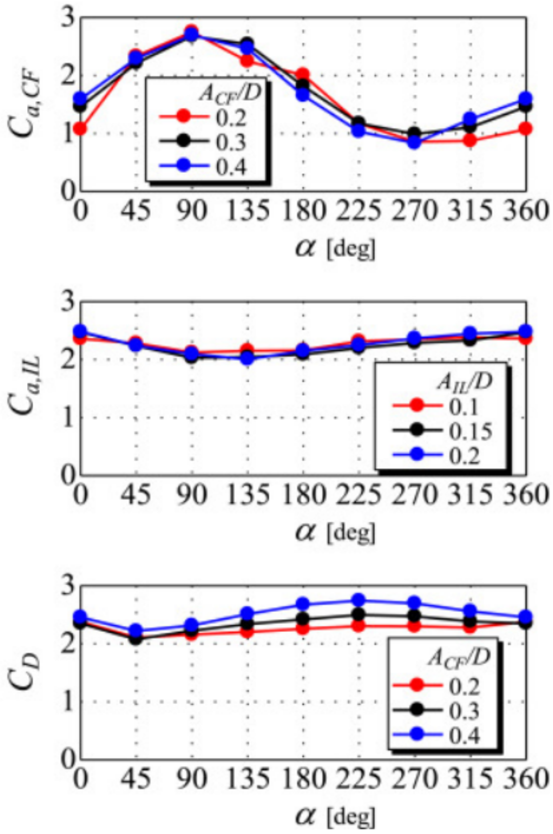

Figure 3.6: Senga et al.: Added mass and drag coefficients found from forced oscillation tests

The cross-flow added mass coefficient oscillates around 1.5 which was in good correspondence with the added mass coefficient found from the analytical formulas. However, the in-line added mass had a mean larger than two (about 2.2) so the assumption of having equal added mass coefficients cross-flow and in-line was not exact. The drag coefficient was also larger than two and hence larger than the value obtained from the analytical formulas.

It should be noted that the drag coefficients found from forced oscillation tests normally are larger than for stationary cylinders and that it cannot be expected that the analytical formula captures this effect. Senga also performed towing of a stationary cylinder in two directions (forth and back), and the mean of the measured drag coefficients was about 1.63. One should note that the drag coefficient was about 1.58 in one direction and 1.67 in the other direction, which revealed that some uncertainty is related to the results from the model tests. The number of strake turns was only 1.5, and normally it is desired that a strake model has an integer number of turns or has a sufficient number of strake turns to represent the hydrodynamic coefficients of a real straked pipe.

Overall the analytic formulas were found to fit reasonably well to the experimental data. However, as the in-line added mass coefficient deviated from the cross-flow added mass coefficient in the experiments it would be appropriate to investigate the effect of applying different added mass coefficients cross-flow and in-line in the simulations. It should also be noted that the analytical drag coefficient in normal direction is highly dependent on the drag coefficient for bare pipe (see Equation (3.1.3)), which is illustrated in Table 3.3. With reference to Section 3.2.3, the drag coefficient for bare sections was set to 1.2, but calibration of the hydrodynamic coefficients for bare pipe (see Section 3.6) might alter it. This will, if being consistent, lead to a changed drag coefficient for the straked section.

Table 3.3: Dependency of drag coefficient for straked section on drag coefficient for bare section

| **Drag coefficient for straked section[-]** | **Drag coefficient for bare section[-]** |
|---|---|
| 1.29 | 0.8 |
| 1.45 | 0.9 |
| 1.61 | 1 |
| 1.77 | 1.1 |
| 1.94 | 1.2 |
| 2.1 | 1.3 |

## 3.4 Structural and numerical model

The riser tested in the NDP experiments was modelled by a finite element formulation in order to obtain the system stiffness, damping and mass matrices (**K**, **C** and **M**). In order to include structural damping, Rayleigh damping was used:

$$\mathbf{C} = \alpha_1 \mathbf{M} + \alpha_2 \mathbf{K}. \tag{3.4.1}$$

Decay tests in air of a bare riser were performed in order to find the natural frequencies up to 4th order and the structural damping was reported [31] to be 0.4% or less than critical damping. $\alpha_1$ was set to 0 and $\alpha_2$ to $10^{-4}$, which corresponds to damping ratios below 0.4% at all fundamental cross-flow frequencies. As the fundamental in-line frequency is typically seen at two times the fundamental cross-flow frequency the damping ratio was almost 0.8% at the largest fundamental in-line frequency. It is however typical that higher order modes are associated with higher damping ratios, and as only the damping ratios for the first 4 modes were reported, the higher damping ratios were found acceptable.

As explained in Section 3.8.2 convergence with respect to the number of elements was not achieved. Instead the choice of number of elements was based on having at least ten elements contained in each half period of a mode shape. From the bare pipe simulations the highest observed mode shape of the in-line response was mode 25, hence the structure was divided in 500 elements. The beam element based on small strain theory described in Section 3.2.1 was used. For calculation of the cross-flow and in-line response, numerical time integration of the dynamic equilibrium equation was performed:

$$\mathbf{M}\ddot{\mathbf{r}} + \mathbf{C}\dot{\mathbf{r}} + \mathbf{K}\mathbf{r} = \mathbf{R}^E, \tag{3.4.2}$$

where $\mathbf{r}$, $\dot{\mathbf{r}}$ and $\ddot{\mathbf{r}}$ are the nodal displacement, velocity and acceleration vector, respectively, and $\mathbf{R}^E$ is the external force vector containing the hydrodynamic loads described in Section 2.5.2 and 3.1. The size of the time step and the length of the simulations were for each simulated case set with respect to the fundamental cross-flow period found in the NDP experiments: each such period contained 40 time-steps and 400 periods were simulated for each case. In order to remove transients the first 200 of these periods were removed. Equilibrium iterations were performed at each time-step by the pure Newton-Raphson method. The maximum number of iterations per time-step was set to the default 10, and the required accuracy of displacements for the iterations to stop was set to $10^{-5}$. The dynamic analysis was started from static equilibrium which was achieved from running the static analysis by an incremental loading procedure. The structure was loaded with specified forces, volume forces and current forces, in that order, with ten increments for each of the three procedures. For each increment Newton-Raphson iterations were performed (with maximum ten iterations) to achieve the equilibrium position to an accuracy of $10^{-6}$.

## 3.5 Analysis procedure

This section provides an overview of how simulations have been run, how simulation data was extracted from Riflex and post-processed in Matlab. As well the processing of the raw data from the NDP experiments and how the simulation data and the experimental data are compared, are presented.

### 3.5.1 Running Riflex and extracting results

The simulations were run in batch-mode from Matlab, where a script for automatically running the desired simulations and storing the simulation data was used. A separate script was used for post processing. The simulation data was obtained by specifying the desired data output in the input-file to DYNMOD:

- Nodal displacements in the global x-, y- and z-direction for all nodes were written to an ASCII-file every second time step.
- The element curvature about the local y- and z-axis at both ends of each beam element was written to an ASCII-file every second time step.

The raw data (strains and accelerations) from the NDP experiments were provided in mat-files, and from this the stresses and fatigue were computed from strains and accelerations were integrated in order to obtain displacements.

Examples of input-files to INPMOD, STAMOD and DYNMOD are shown in Appendix A, and all relevant Matlab-files are explained in Appendix B.

### 3.5.2 Filtering

Before validation of the simulations could be done, band-pass filtering was applied to both the simulation data and the NDP experimental data. The response in the NDP experiments contained slowly varying components from the test rig which needed to be filtered out in order to avoid them from dominating the VIV related response. It was in [31] found that filtering away components below $0.75Hz$ for all cases was appropriate. As well the band-pass filtering was done in order to separate the fundamental response (cross-flow at $1\omega$ and in-line at $2\omega$) from the total response, which may contain significant contributions from higher harmonics.

In order to establish appropriate frequency bandwidths the Fourier transform of the experimental strain time series was plotted, and the fundamental cross-flow frequency $\omega$ was identified at the sensor with largest response (evaluated in terms of the standard deviation of stress). In addition, measurements from three fixed sensors were considered: sensor 5, 19 and 36, i.e. one at each end of the riser and one close to the mid-span. This was done in order to make sure that both the low and high frequencies exited in the low/high speed part of the riser when exposed to shear flow were not removed when filtering. The sensor positions are given in Table 4.1. It was decided to set the lower cut-off frequency as a function of the Strouhal number for each case, as done in [31], and the upper cut-off frequency as a function of the fundamental frequency so that fundamental frequency response and total response were distinguished. The Strouhal number was set to 0.17, and in the shear flow cases the maximum speed was used for computing the Strouhal frequency. The same procedure was done with the simulation data, but here the slowly varying in-line components discussed in Section 3.8.1 had to be considered as well. In order to remove the unwanted low-frequency response, and not remove VIV related signals, the bandwidths shown in Figure 3.4 were found appropriate. "Exp" refers to the NDP experimental data, while "Sim" refers to the simulation data.

Table 3.4: Frequency bandwidths for filtering of NDP experimental data and simulation data
$f_s$ is the Strouhal frequency, $f$ is the fundamental cross-flow frequency $\omega$ in $Hz$

| | **Exp: bare** | **Exp: 41% straked** | **Exp: 62% straked** | **Sim** |
|---|---|---|---|---|
| CF ($1\omega$) | $\frac{1}{3}f_s$-$1.5f$ | $\frac{1}{6}f_s$-$1.5f$ | $\frac{1}{8}f_s$-$1.5f$ | 0.5Hz-$1.5f$ |
| IL ($2\omega$) | $\frac{2}{3}f_s$-$2.5f$ | $\frac{1}{3}f_s$-$2.5f$ | $\frac{1}{4}f_s$-$2.5f$ | $0.5f$-$2.5f$ |

It was found in [8] that the response for the pipes with partial strake coverage (for many cases) was dominated by the highest shedding frequency of the bare part of the riser. The response for the partial strake coverage scenarios in sheared current is hence expected to be dominated by much lower frequencies than for the bare pipe scenarios. Consequently a lower high-pass frequency is chosen for the 41% and 62% partial strakes scenarios than for the bare scenarios in order to not remove these components.

### 3.5.3 Spectral analysis and time series

The spectra and time series of the cross-flow and in-line displacement and curvature were plotted for each simulated case. It was made sure transients were removed by looking at the time series, and by discrete Fourier transform (DFT) in Matlab, applying a fast Fourier transform (FFT) algorithm, the spectra were obtained. Note that the FFT algorithm returns the symmetric two-sided spectrum, so in order to obtain the one-sided spectrum the energy contained at positive frequencies in the two-sided spectrum is multiplied with two. The Fourier transform of a discrete signal $x = [x_1, x_2, ..., x_N]$ in the time domain is given by:

$$X(k) = \sum_{n=0}^{N-1} x(n) e^{-i2\pi \frac{nk}{N}}, \tag{3.5.1}$$

where $i$ is the imaginary unit. In addition to choosing filtering bandwidths the spectra were used for identifying and comparing the active cross-flow and in-line frequencies in the predictions and the experiments. As well both the spectra and time series were useful when looking into the appearance of the slowly varying components in the in-line displacement response discussed in Section 3.8.1.

### 3.5.4 Dominating frequency

The dominating frequencies cross-flow and in-line were in this thesis taken as the peak frequencies in the stress spectra at the positions along the riser with maximum stress standard deviation cross-flow and in-line. Note that in the cases with partial strake coverage the dominating frequencies were taken from the maximum stress response in the bare section. The method used for determining the dominating frequency involved that the dominating frequencies cross-flow and in-line not necessarily were extracted from the same point along the riser. Correspondingly, the dominating frequencies in the simulations did not have to be extracted from the same positions as the dominating frequencies in the experiments. Plots of the predicted dominating frequencies cross-flow and in-line as functions of current speed were made and compared with the measurements from the NDP experiments.

### 3.5.5 Standard deviation and mean standard deviation along riser

The displacements and stresses were for each case stored in matrices where each column contained the time series at a point along the riser. The standard deviation (std) of each column was taken so that a vector with the std at each data point along the riser was created. For a vector $x = [x_1, x_2, ..., x_N]$ with $N$ scalar observations in time the standard deviation $\sigma$ is defined as:

$$\sigma = \sqrt{\frac{1}{N-1}\sum_{n=1}^{N}(x(n) - \bar{x})^2}, \tag{3.5.2}$$

where $\bar{x}$ is the mean of $x$. Plotting this versus the length of the riser was a useful measure of the predicted and measured response amplitudes over time, as well as it provided an indication of which mode that was dominating and if travelling or standing waves dominated the response. Both cross-flow and in-line displacements and stresses were considered.

To provide a general overview and evaluate the response amplitude of more than one simulated case at the time, the mean along the riser of the standard deviations of the time series, $\bar{\sigma}$, was found and plotted against the current speed. Let $\sigma_v$ be a vector containing the standard deviations at $M$ positions along the riser, then $\bar{\sigma}$ is given by:

$$\bar{\sigma} = \frac{1}{M}\sum_{m=1}^{M}\sigma_v(m). \tag{3.5.3}$$

This was done for both cross-flow and in-line displacements and stresses. In the simulations the part of the riser between the first and the last sensor in the experiments was considered when computing $\bar{\sigma}$. This is illustrated in Figure 3.7 for displacement, and an equivalent procedure was applied for stress with respect to strain gauge positions both cross-flow and in-line.

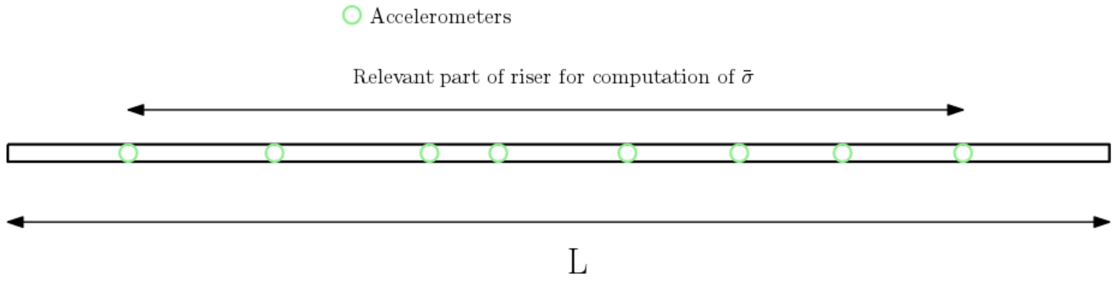

Figure 3.7: Illustration of part of riser considered for computing $\bar{\sigma}$

### 3.5.6 Fatigue damage

All structures in the ocean are subjected to dynamic loads induced by wind, waves and currents. The magnitude of the dynamic loads might be far below yield, but their cyclic behaviour will cause microscopic imperfections in the material which over time leads to gradual crack growth. Eventually the crack becomes so large that the cross-section no longer has capacity to withstand the loads and failure occurs. This phenomenon is referred to as fatigue and is important with respect to estimating the lifetime of a marine structure.

For predicting the fatigue life of a structure given certain environmental conditions, a material response model must be chosen in order to evaluate how the structure will respond to the long term stress distribution it is exposed to. Either a fracture mechanics approach, which focuses on the propagation of a crack and its local stresses, or a SN-curve approach can be applied as response model. In this thesis the SN-curve approach has been used and is what will be focused on in the next sections.

### Cross-flow and in-line stress computation

To be able to estimate the fatigue damage a stress (or strain) history must be created. The circular cross-section in Figure 3.8 is considered (same as right-handed local coordinate system used in Riflex), and only the axial stress contribution is taken into account. The axial stress $\sigma$ at a point of a thin-walled circular cross-section is generally a function of the local loads and the angular position within the cross-section:

$$\sigma = \frac{N_x}{A} + \frac{M_y}{I_y}z + \frac{M_z}{I_z}y = \frac{N_x}{A} + \frac{M_y}{I_y}r\text{sin}\theta + \frac{M_z}{I_z}r\text{cos}\theta, \tag{3.5.4}$$

where $N_x$ is the axial force, $A$ is the area of the cross-section, $M_y$ and $M_z$ are the bending moments and $I_y$ and $I_z$ are the second area of moments about the local y-axis and z-axis, respectively.

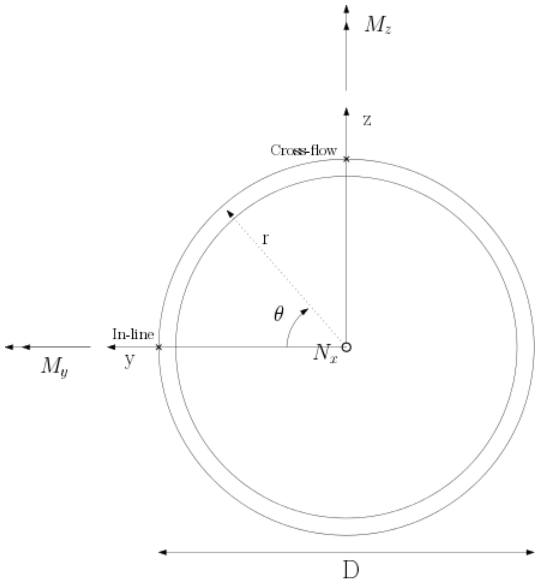

Figure 3.8: Coordinate system for computation of stress time series

In this thesis only the so-called cross-flow and in-line stress $\sigma_{CF}$ and $\sigma_{IL}$ are considered, corresponding to the stress at the outer fibre at $\theta = 90°$ and $\theta = 0°$. The variation of the stress contribution from the $N_x$-term is assumed negligible compared to the other terms. As explained in Section 3.5.1 the curvature $\kappa_y$ and $\kappa_z$ about the local y- and z-axis are given as output from Riflex, so it is more relevant expressing $\sigma_{CF}$ and $\sigma_{IL}$ in terms of curvature than moment:

$$\begin{aligned} \sigma_{CF} &= E \cdot \kappa_y \frac{D}{2} \\ \sigma_{IL} &= E \cdot \kappa_z \frac{D}{2}. \end{aligned} \tag{3.5.5}$$

Here the relation between moment and curvature presented in Equation (2.2.2) was used.

In experiments the strains at desired positions at the edge of the cross-section are typically measured by strain gauges. Strain gauges were positioned at $\theta = 90°$ and $\theta = 0°$ at several positions along the riser (presented in Table 4.1) in the benchmark experiment NDP High Mode VIV tests [31], and the measured strains were simply converted to stresses by multiplying with Young's modulus.

### SN-curve approach

When computing the fatigue damage of a structure exposed of cyclic loads it is common engineering practice to ignore the mean of the varying stress and consider only the stress variation as important for crack growth. The SN-curve approach is based on data from laboratory experiments where simple test specimens are subjected to stress ranges of varying magnitude until failure is reached. The SN-curves relate the number of cycles to failure $N$ to the stress range $\Delta\sigma$ by:

$$N = K\Delta\sigma^{-m}, \tag{3.5.6}$$

which is typically given in log-log scale:

$$\log(N) = \log(K) - m * \log(\Delta\sigma). \tag{3.5.7}$$

Here $\log(K)$ is the interception of the $\log(N)$-axis, and the SN-curve and $m$ is the slope of the SN-curve. A one-sloped SN-curve was applied for the fatigue assessment of the NDP experiments and simulations, with the parameters given in Table 3.5:

Table 3.5: SN-curve parameters

| **log(K)** | **m** |
|---|---|
| 11.63 | 3 |

### Stress cycle counting

In order to use the SN-curves to determine the fatigue damage the stress cycles, with associated ranges, must be counted, as the stress history in general will not be a simple periodic loading with constant amplitude. The objective of cycle counting is to split the complex stress history into discrete events of loading cycles. This permits evaluation of the damage caused by each loading cycle. There exist several counting methods, such as the mean crossing-range technique (modified version of the level-crossing method) and the rainflow counting method [39]. The rainflow counting method was proposed by Matsuishi and Endo [40] and is the most popular cycle counting method. The procedure for rainflow counting is given below and is illustrated by the stress time series in Figure 3.9.

- Each rainflow begins at the beginning of the time series and successively at the inside of every peak and valley.
- A rainflow initiating at a peak (or a valley) drops down until it reaches opposite a peak more positive (or a valley more negative) than the peak (or the valley) it started from. Illustrated in Figure 3.9 by the counted half-cycles 1-2-4, 2-3, 4-5-7, 5-6 and 8-9.
- A rainflow also stops when it meets the rainflow from a roof above. Illustrated in Figure 3.9 by the counted half-cycles 3-2', 6-5' and 9-8'.

- A rainflow must terminate at the end of the time series. Illustrated in Figure 3.9 by the counted half-cycle 7-8-10.
- The horizontal length of each rainflow is counted as a half cycle with that stress range.

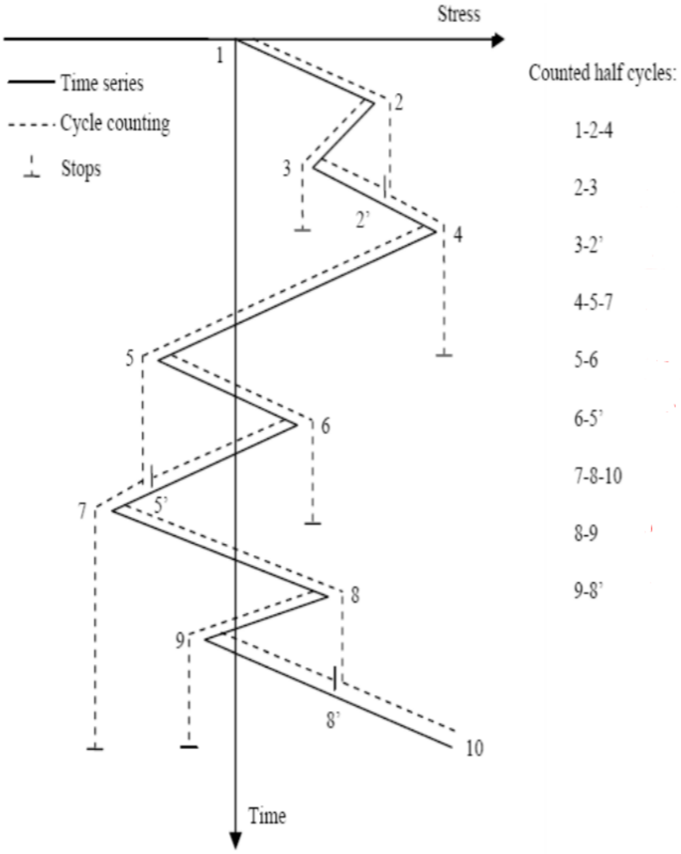

Figure 3.9: Illustration of rainflow counting

In order to perform the cycle counting the rainflow counting routine from the WAFO [41] Matlab toolbox was used.

### Linear fatigue damage accumulation - The Palmgren-Miner rule

The Palmgren-Miner rule is commonly used for estimating the fatigue damage from a long-term stress distribution. It assumes that fatigue damage accumulates linearly. When stress cycle counting has been performed, and the long-term stress distribution is expressed by a stress histogram with $k$ stress range blocks, the Palmgren-Miner rule can be applied, expressing the total accumulated fatigue damage $D$ as:

$$D = \sum_{i=1}^{k} \frac{n_i}{N_i}. \tag{3.5.8}$$

Here $n_i$ is the number of cycles in stress range block $i$ and $N_i$ is the number of cycles to failure in stress range block $i$. Failure occurs when $D \geq 1$.

Typically the time scale of experiments or simulations are limited to seconds and minutes, while real structures are meant to operate for years. The annual accumulated fatigue damage $D_{year}$ was hence considered, and to estimate it the number of cycles $n_i$ were scaled linearly from the duration of the experiment or simulation $t$ to the duration of a year:

$$\begin{aligned} D_{year} &= \sum_{i=1}^{k} \frac{n_{i,year}}{N_i} \\ n_{i,year} &= \frac{n_i \cdot 365 \cdot 24 \cdot 60 \cdot 60}{t}. \end{aligned} \tag{3.5.9}$$

With the rainflow cycles counted, a script from the WAFO [41] toolbox was used to find the total Palmgren-Miner damage at each node along the riser in the simulations and at each sensor in the experiments.

**Fatigue safety factors**

In order to assess the accuracy of the model predictions the ratio $R_D$ between the predicted and measured annual maximum fatigue damage along the riser was taken for each simulated case:

$$R_D = \frac{\text{Predicted maximum fatigue damage}}{\text{Measured maximum fatigue damage}} \tag{3.5.10}$$

$R_D$ stated whether a prediction was conservative or not; if $R_D > 1$ the prediction was conservative and if $R_D < 1$ the prediction was non-conservative. It was desired that the model itself was able to obtain conservative fatigue estimates, but safety factors were in some cases needed and for each simulated case the safety was given as $\eta = 1/R_D$. A general safety factor should however be applied, at least within a set of simulations. Thorsen [28] introduced two such general safety factors, where the first was based on the most non-conservative prediction within a simulation set, $\eta_{max}$, and the other was the median of the safety factors within a simulation set, $\eta_{med}$. $\eta_{max}$ ensured that all maximum fatigue estimates were conservative (the most non-conservative will be accurate), but could lead to very large estimates of the most conservative predictions. $\eta_{med}$ on the other hand assured that 50% of the fatigue estimates were conservative.

## 3.6 Calibration of hydrodynamic coefficients

It was desired to have a model with one set of empirical parameters able to predict the cross-flow and in-line VIV response in both uniform and shear flow. In order to achieve this, calibration of selected empirical TD VIV parameters through simulations of a bare pipe exposed to both uniform and sheared current, with varying current speed, were performed. The results of the simulations were compared to the corresponding NDP experiments.

### 3.6.1 Initial TD VIV model

The parameters related to the TD VIV model were initially taken equal to those of the 4th paper of the doctoral thesis by Ulveseter [3] (the paper had not yet been accepted for journal publication so a direct reference to the paper could not be made), as this paper used the NDP experiments with bare pipes for benchmarking. Here the cross-flow and in-line excitation coefficients were chosen so that good correspondence between the results from experiments and simulations, with respect to the mean of the root mean square of strain along the riser, was obtained. The initial hydrodynamic parameters are presented in Table 3.6, where the TD VIV parameters are not given with the notation used in the Riflex User Manual [36], but with the same notation as in Section 2.5.2: $C_{v,y}$ and $C_{v,x}$ are the cross-flow and in-line excitation coefficients, respectively, $\hat{f}_0$ is the center and $\hat{f}_{min}$ and $\hat{f}_{max}$ are the boundaries of the synchronization range given as non-dimensional frequencies. $\alpha$ is the dimensionless parameter restricting the in-line response frequency with respect to two times the cross-flow response frequency. $C_{hh}$ is the higher harmonic load coefficient set to zero as higher harmonics are not studied in this thesis.

Table 3.6: Initial model: hydrodynamic coefficients for bare riser section

| **Parameter** | **Magnitude** |
|---|---|
| Quadratic drag coefficient in tangential direction [-] | 0 |
| Quadratic drag coefficient in normal direction [-] | 1.2 |
| Added mass per unit length in tangential direction [-] | 0 |
| Added mass per unit length in normal direction [-] | 1 |
| Hydrodynamic diameter [m] | 0.027 |
| $C_{v,y}$ [-] | 0.85 |
| $C_{v,x}$ [-] | 0.75 |
| $\hat{f}_0$ [-] | 0.144 |
| $\hat{f}_{min}$ [-] | 0.08 |
| $\hat{f}_{max}$ [-] | 0.208 |
| $\alpha$ [-] | 0.15 |
| $C_{hh}$ [-] | 0 |

Ulveseter [3] calibrated the TD VIV model considering only the uniform flow cases of the NDP experiments. It was hoped that the same set of parameters would give good results also for the shear flow cases. Simulations of the shear flow cases where hence performed, and a comparison with the measurements (Meas) showed that the predicted stress response (Pred) was underestimated, especially at higher speeds as seen in Figure 3.10. Similar results are seen for the displacements, and it was clear that a new calibration of the model parameters had to be done.

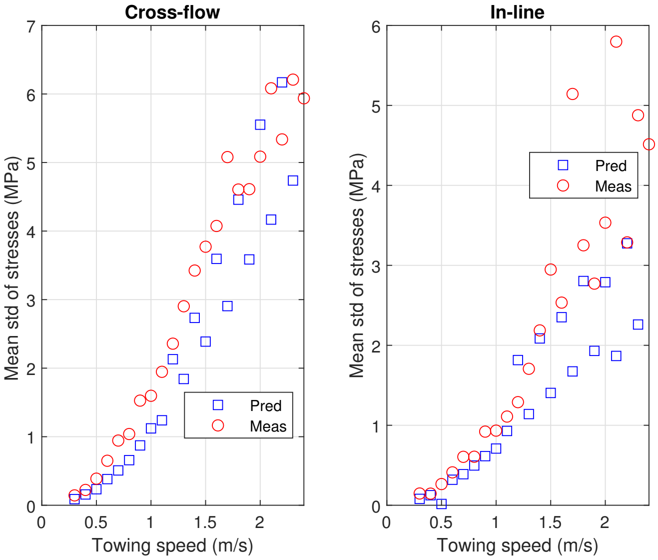

Figure 3.10: Mean standard deviation (std) of cross-flow and in-line stresses for shear flow cases with initial model
Maximum of sheared current profile: 0.3-2.4 $m/s$

### 3.6.2 Calibration procedure

A real marine riser will be exposed to waves and currents varying with both time and depth. A riser exposed to uniform flow hence represents ideal conditions, and even though a perfect shear flow is not seen in real conditions it is considered the most realistic of the two. Therefore it was decided to calibrate with respect to the shear flow cases and evaluate if the resulting parameters from the calibration provided acceptable results also for the uniform flow cases. The mean stress standard deviation along the riser was focused on during the calibration, having also the fatigue and displacements in mind.

It had to be decided which of the parameters in the TD VIV model that should be kept from the initial model and which that should be changed and calibrated. As it seemed like the dominating frequency was predicted quite well with the initial parameters, it was chosen not to alter the parameters related to the synchronization range, namely $\hat{f}_0$, $\hat{f}_{min}$, $\hat{f}_{max}$ and $\alpha$. The remaining parameters were the quadratic drag coefficient in normal direction, the added mass per unit length in normal direction, $C_{v,y}$ and $C_{v,x}$. As it seemed clear that the response was too low when exposed to shear flow with the initial parameters the following options were considered: reduce the damping, increase the excitation or a combination of the two. Reducing the damping involved reducing the quadratic drag coefficient in the normal direction, while increasing the excitation meant increasing $C_{v,y}$ and/or $C_{v,x}$.

Prior to calibration it was important to be aware of some features related to altering the quadratic drag coefficient. One of them was that the quadratic drag force is proportional to the square of the relative velocity between the structure and the flow, as presented in Equation (2.5.3), and altering it will hence have a larger impact at high than at low current speeds. As well the damping from quadratic drag typically influences the in-line response less than the cross-flow response due to the smaller amplitudes of vibration. Based on [37] the quadratic drag coefficient was allowed to be within the range 0.5-1.2.

It was desired to establish a relation between the VIV excitation coefficients $C_{v,y}$ and $C_{v,x}$ before initiating the calibration. The idea was that the vortex shedding forces $F_{v,y}$ and $F_{v,x}$ were the components in cross-flow and in-line direction of a vortex shedding force resultant $F_{res}$ as illustrated in Figure 3.11. The vortex shedding forces are then related by:

$$F_{res} = \sqrt{{F_{v,y}}^2 + {F_{v,x}}^2}. \tag{3.6.1}$$

$F_{res}$ was expressed in terms of $C_{res}$ in a similar way as $F_{v,y}$ and $F_{v,x}$ and an expression relating $C_{v,y}$ and $C_{v,x}$ was obtained:

$$C_{res} = \sqrt{{C_{v,y}}^2 + {C_{v,x}}^2}. \tag{3.6.2}$$

The expressions for $F_{v,y}$ and $F_{v,x}$ were presented in Equation (2.5.3) and a quick look at these expressions makes it clear that Equation (3.6.2) is too simple. The relation is however only used for calibration purposes, and calibrations were performed based on this relation. Thorsen [29] investigated cross-flow VIV with $C_{v,y} = 1.2$, while $C_{v,x}$ was not included and set to zero. Based on this it was decided initially to set $C_{res}$ to 1.2 and vary $C_{v,y}$ (and hence vary $C_{v,x}$ according to Equation (3.6.2)). It was decided not to alter $C_{res}$ too much from the initial value and 1.1 and 1.3 were set as lower and upper limits.

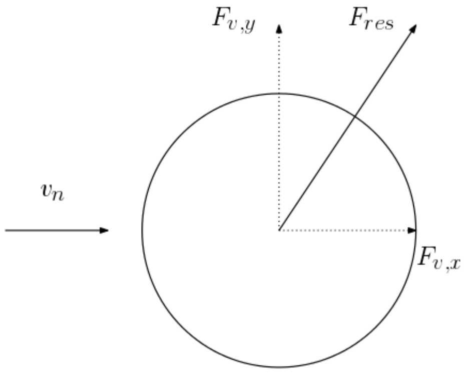

Figure 3.11: Illustration of relation between the cross-flow and in-line vortex shedding forces

## 3.7 Experiment experiences: filtering issues

For the cases with partially straked riser in shear flow some issues were encountered when it came to establishing appropriate bandwidths for filtering the NDP experimental data. One of the issues was related to the uniform flow cases, while the others were related to the shear flow cases with 62% strake coverage.

### 3.7.1 Filtering issue 1

In order to present the first issue the 41% partially straked NDP riser is considered. An effect was observed in the in-line displacement spectra at sensor 19 (close to the mid-span within the straked section, see Table 4.1) when the pipe was exposed of a uniform flow: a significant amount of energy was contained at a frequency about half the fundamental cross-flow frequency, which will be referred to as $\frac{1}{2}\omega$ from now on. It has not been figured out what causes this frequency contribution, but it might be that the increased static displacement of the straked riser section reduced the effective incoming speed, especially in the bare section close to the straked section, and caused a lower natural frequency to be excited. The $\frac{1}{2}\omega$-component was however not seen in the strain spectra and was small in the spectra at sensor 36 (in the bare section). In Figure 3.12 the cross-flow and in-line displacement spectrum with current speed $2.4m/s$ at sensor 19 and for both sensor 5, 19 and 36 are shown in order to illustrate the observation. Considering the fact that no such frequency components were present in the strain spectra (stress and fatigue were the main focus in this thesis) it was decided not to alter the filtering bandwidth presented in Table 3.4, i.e. not filter out the $\frac{1}{2}\omega$-component.

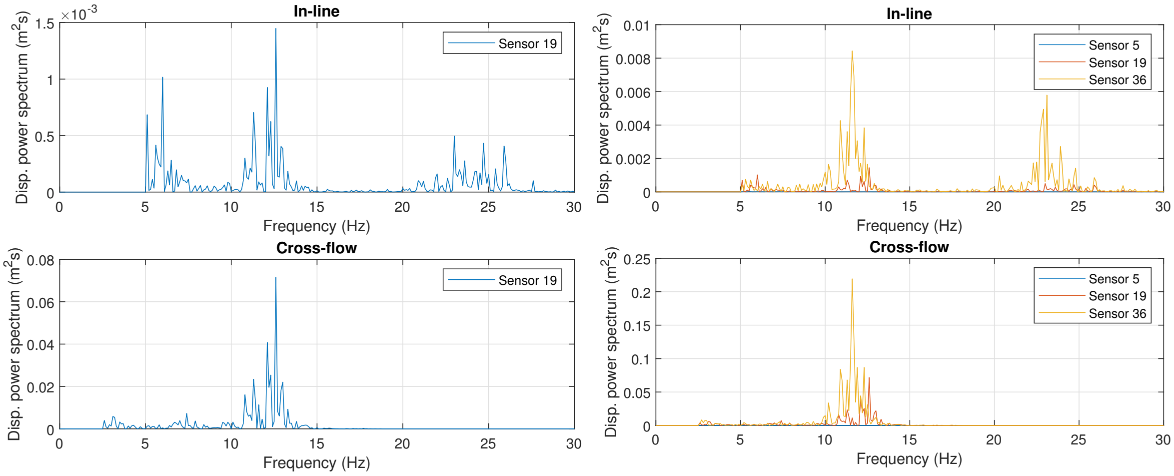

(a) Significant $\frac{1}{2}\omega$-component at sensor 19 (b) Negligible $\frac{1}{2}\omega$-component at sensor 36

Figure 3.12: Filtering issue 1: $\frac{1}{2}\omega$-component
41% strake coverage. Uniform flow. Speed: $2.4m/s$

### 3.7.2 Filtering issue 2

The second issue involved how the lower cut-off frequency should be determined in the shear flow experimental cases with 62% strake coverage. Since the strakes covered the part of the riser with highest current speeds the bare section was exposed to low speeds, and hence relatively low frequencies were expected to be excited. A significant component was observed in the in-line displacement spectra at about 0.8-$1.2Hz$ (from now on referred to as the $1Hz$-component) for the uniform flow cases, which was not expected. The $1Hz$-component was present cross-flow and in-line in both the stress and displacement spectra at higher current speeds in shear flow (again unexpected), which confirmed its presence in both uniform and shear flow. In Figure 3.13 the cross-flow and in-line displacement and strain spectra at selected sensors for both uniform and shear flow with current speed $2.2m/s$ are shown to illustrate the presence of the $1Hz$ component.

While filtering the $1Hz$-component away was the obvious choice for the uniform flow cases, it was likely to be VIV excitation in this frequency region for the shear flow cases with low current speed. A band-pass filter is not capable of recognizing the nature of the different frequency components, so it cannot separate the $1Hz$-component and VIV components in the same frequency region. This introduces an uncertainty when comparing simulations and experiments, as no $1Hz$-component was consistently predicted over the range of current speeds. It was in the end decided to set the lower cut-off frequency (see Table 3.4) lower than the dominating frequency in the simulations, which successfully filtered out the $1Hz$ component for higher current speeds. However the in-line response contribution was, in general, still largest from the lowest remaining frequencies even after applying this high-pass frequency. The presence of these slowly varying components are probably related to the rig response, and it has also previously been found, by

Kristiansen and Lie [42], that separating the rig response and the VIV response for these tests is difficult. Due to the small displacement and strain response for these tests they concluded that it was acceptable that a perfect divide could not be established.

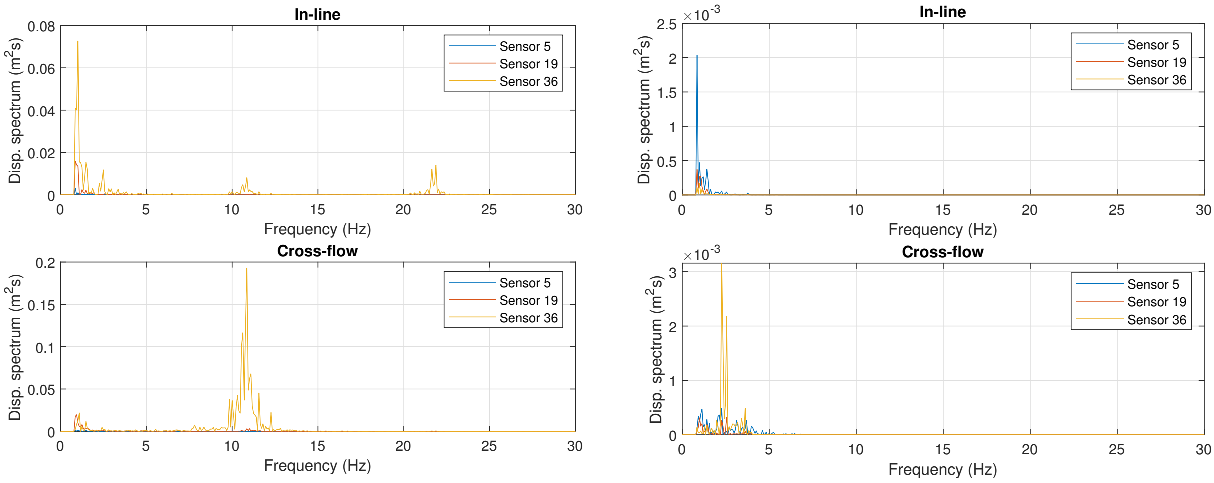

(a) Displacement power spectrum: uniform flow (b) Displacement power spectrum: shear flow

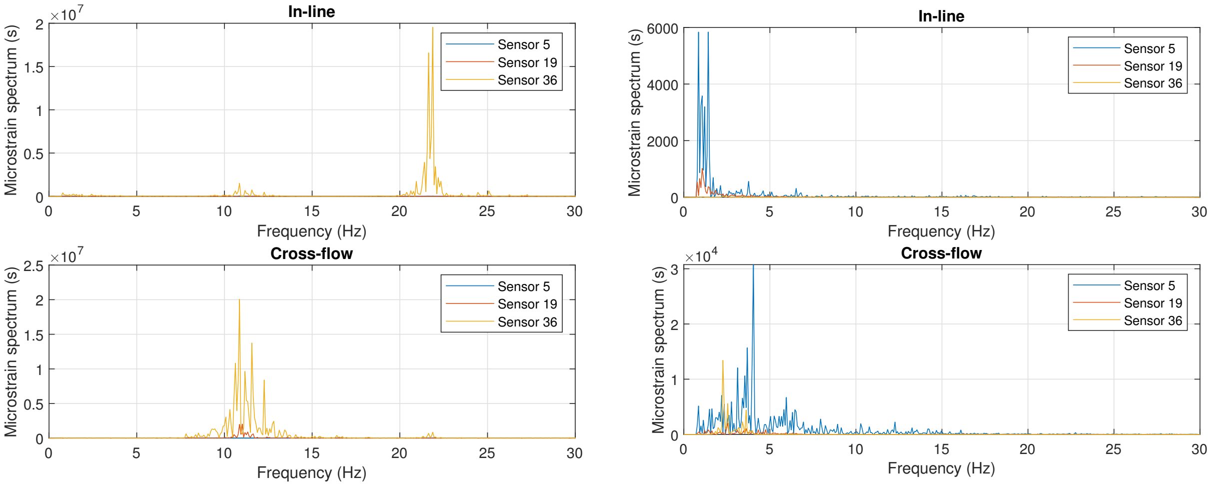

(c) Strain ($\frac{\mu m}{m}$) power spectrum: uniform flow (d) Strain ($\frac{\mu m}{m}$) power spectrum: shear flow

Figure 3.13: Filtering issue 2: $1Hz$-component
62% strake coverage. Speed: $2.2m/s$

### 3.7.3 Filtering issue 3

The third filtering issue was related to the upper cut-off frequency for the shear flow cases with 62% strake coverage. As explained in Section 3.5.2 the upper cut-off frequency was based on the fundamental cross-flow frequency $\omega$ found as the peak frequency at the position of maximum stress response and was set to $1.5\omega$. Now consider the cross-flow strain spectrum at the position of maximum stress response with current speed $2.4m/s$ in Figure 3.14 (a). $\omega$ was found as $3.4Hz$, and consequently the upper cut-off frequency was $5.1Hz$. A simple estimate of expected frequencies was done based on the Strouhal frequency: assuming the Strouhal number was 0.17 and that the highest speed in the bare section was 25% of the maximum current speed acting along the riser, the largest expected fundamental cross-flow frequency was $3.8Hz$. The signals in the range 3.8-5.1$Hz$, assumed to be higher order terms, were hence not removed, but are large enough to affect the response. It should also be noted that the spectrum in Figure 3.14 (a) indicates stochastic response. This was confirmed by dividing the entire strain time series in three equally long time intervals and plotting the spectra for each of these intervals as shown in Figure 3.14 (b). The upper cut-off frequency was kept as it was defined in Section 3.5.2, but one should be aware of the features explained in this section when evaluating the results.

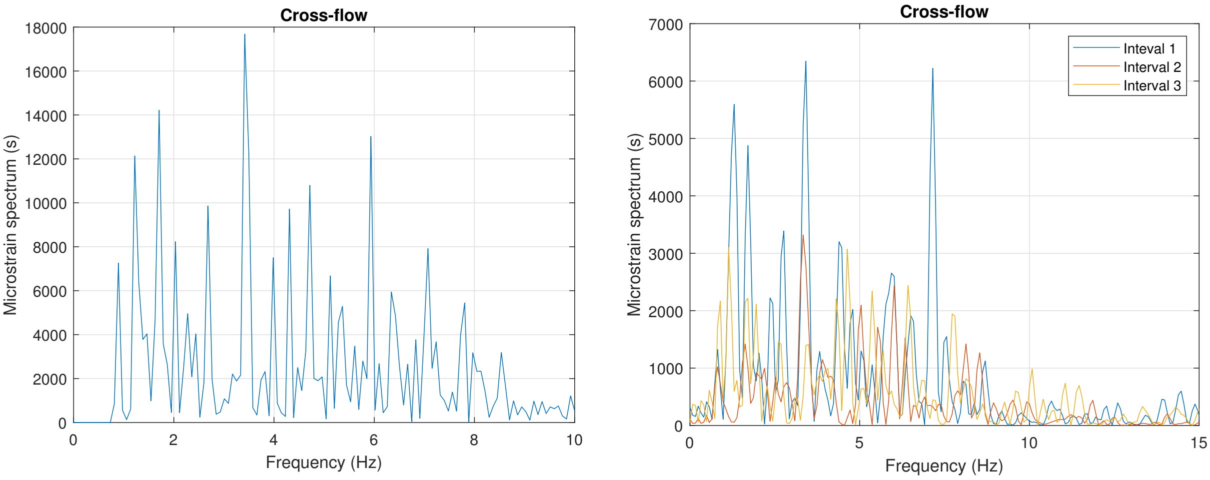

(a) Strain ($\frac{\mu m}{m}$) power spectrum from entire time series

(b) Strain ($\frac{\mu m}{m}$) power spectra from three time intervals

Figure 3.14: Filtering issue 3: broad-banded response
62% strake coverage. Shear flow. Speed: $2.4m/s$

## 3.8 Model experiences

During the thesis work several model observations were made which were not considered as results of the thesis, but that are convenient to be aware of for others that will use the model in further work. These observations are named model experiences and are presented in the next sections. All model experiences were acquired when simulating the NDP experiments presented in Chapter 4.

### 3.8.1 Slowly varying in-line component

When performing bare pipe simulations with the initial model presented in Table 3.6 it was soon discovered that the in-line displacement response contained a slowly varying component. The slowly varying in-line component was for some current speeds dominating the displacement response both for the uniform and shear flow cases. Especially in the uniform flow cases the slowly varying component was important, and at some current speeds it caused the in-line motion to be much larger than the cross-flow motion. An example is shown in Figure 3.15. In (a) the unfiltered and filtered in-line displacement spectra are shown, and the unfiltered spectrum shows that a lot of energy is contained at low frequencies which are not VIV related. (b) shows the presence of slowly varying components in the in-line displacement time series and that no such components are present cross-flow. For the shear flow cases the slowly varying components were for most cases present, but not equally dominating as for the uniform flow cases.

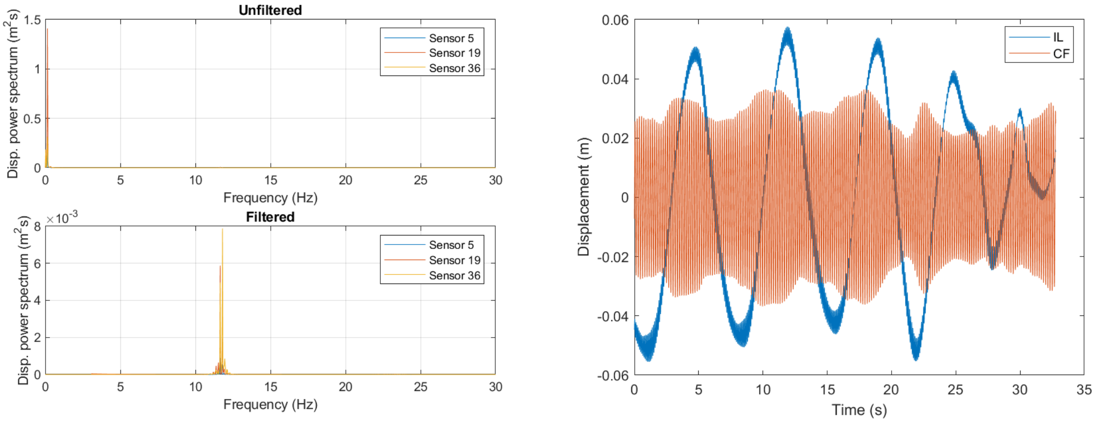

(a) In-line unfiltered and filtered displacement power spectrum

(b) Cross-flow and in-line displacement time series at sensor 19

Figure 3.15: Illustration of slowly varying in-line component for NDP uniform flow case with bare pipe Current speed: $1.1m/s$

Several exercises were done in order to remove the slowly varying in-line components:

- Structural mass proportional damping was introduced, which should affect low frequent response.
- The structural stiffness proportional damping was increased.
- The $\alpha$-parameter and synchronisation range were altered.
- Linear hydrodynamic damping was included in addition to quadratic damping in the Morison equation.

However, none of these attempts were completely successful. Neither changing the $\alpha$-parameter, the synchronization range or introducing linear hydrodynamic damping had any clear effect. Increasing the stiffness proportional damping was seen to have an effect at some speeds, but increasing it too much would introduce too large damping at the VIV related frequencies and hence not be physical. The most successful attempt was introducing mass proportional damping, and in Figure 3.16 the result of simulating the same case as in Figure 3.15 with Rayleigh damping constants $\alpha_1 = 0.05$ and $\alpha_2 = 10^{-4}$ is shown. The energy at very low frequencies has clearly been reduced, but still dominant low-frequent peaks are seen in the unfiltered displacement spectra.

It was difficult to predict at which frequency the most important slowly varying component occurs, as it varied from $0.01Hz$ to $0.3Hz$ over the range of simulated cases. The difference in damping ratio at these two frequency limits will be large, which makes it difficult to choose appropriate Rayleigh damping constants.

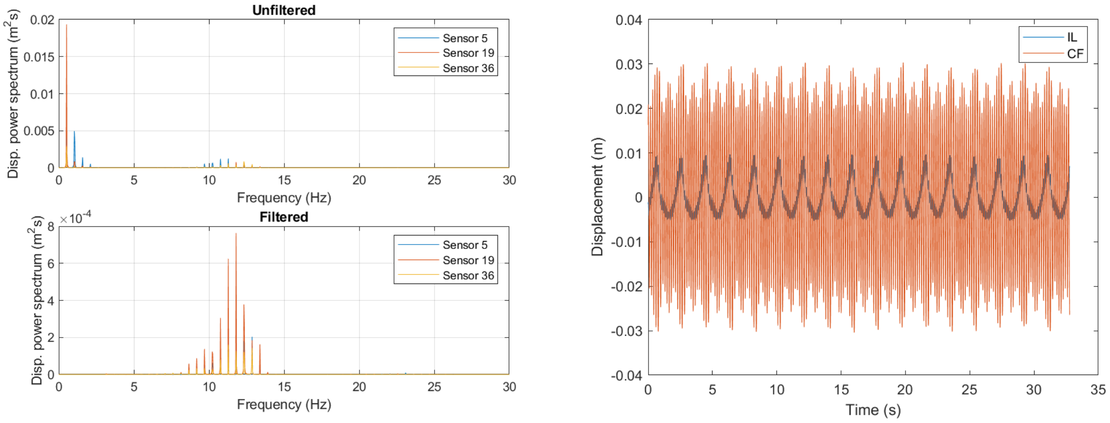

(a) In-line unfiltered and filtered displacement power spectrum

(b) Cross-flow and in-line displacement time series at sensor 19

Figure 3.16: Effect of mass proportional damping om slowly varying in-line component for NDP uniform flow case with bare pipe
Current speed: $1.1 m/s$

The slowly varying in-line components were found to be of small significance for curvature (and consequently strain and stress). This is illustrated in Figure 3.17 where the high-pass filtered and unfiltered curvature standard deviation both cross-flow and in-line are seen to be more or less equal. Slowly-varying components contribute little to fatigue, and it was decided that removing the slowly varying component was acceptable. The frequency bandwidths in Table 3.4 were found suitable for this, as the frequency of the slowly varying components was far below the lowest cut-off frequencies for all simulated cases. The reason for the presence of slowly varying components is suspected to be due to slowly varying drag amplification caused by the formulation of the load model in a local reference frame. It is an effect of the local-global reference frame transformation which Ulveseter provides an explanation of in the 4th paper of his doctoral thesis [3].

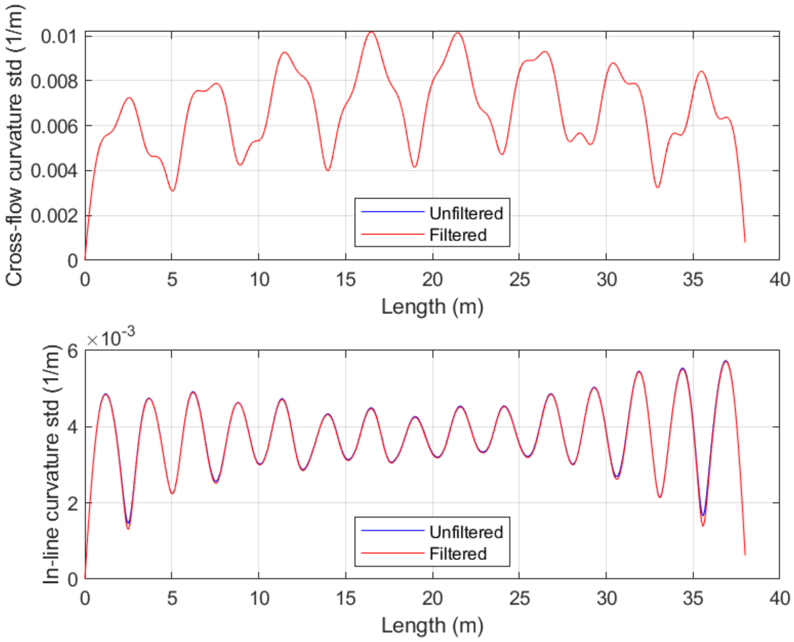

Figure 3.17: Representative case illustrating the small effect of slowly-varying in-line components with respect to curvature for a NDP uniform flow case with bare pipe
Current speed: 1.1m/s

### 3.8.2 Mesh convergence study

In order to choose an appropriate number of elements for the mesh of the riser, a convergence study was performed for the bare riser cases. Convergence was evaluated with respect to the cross-flow stress along the riser and at the location of sensor 19 in the NDP experiments, which is close to the mid-span (see Table 4.1 for the exact position). Both shear and uniform flow cases were investigated and one low, one high and one mean current speed were considered. The results are shown in Figure 3.18 and 3.19. Note that at which end of the riser the largest response was found in the uniform flow cases was random; since the model and the current were symmetric it was the initial phasing of the vortex shedding forces that determined if the largest response was found at the left or right end of the riser. To better visualize convergence the simulation data was processed so that the largest response is displayed at the left end for the three uniform flow cases.

The shear flow cases exhibited a higher degree of element convergence than the uniform flow cases. However, it was seen in the two shear flow cases with lowest speed that the solution alternated between two solutions, instead of approaching a single solution. Different dominating modes were associated with the two solutions, but they were seen to be of the same order of magnitude. In the uniform flow cases each mesh provided a unique solution for higher current speeds, while convergence was achieved in the low current speed case. The problem with achieving convergence by increasing the number of elements has to do with the fact that more information will be contained in the load model as the number of elements is increased. Due to the non-linearity of the load model the number of elements changes the problem, and it is not in the nature of the model to achieve element convergence.

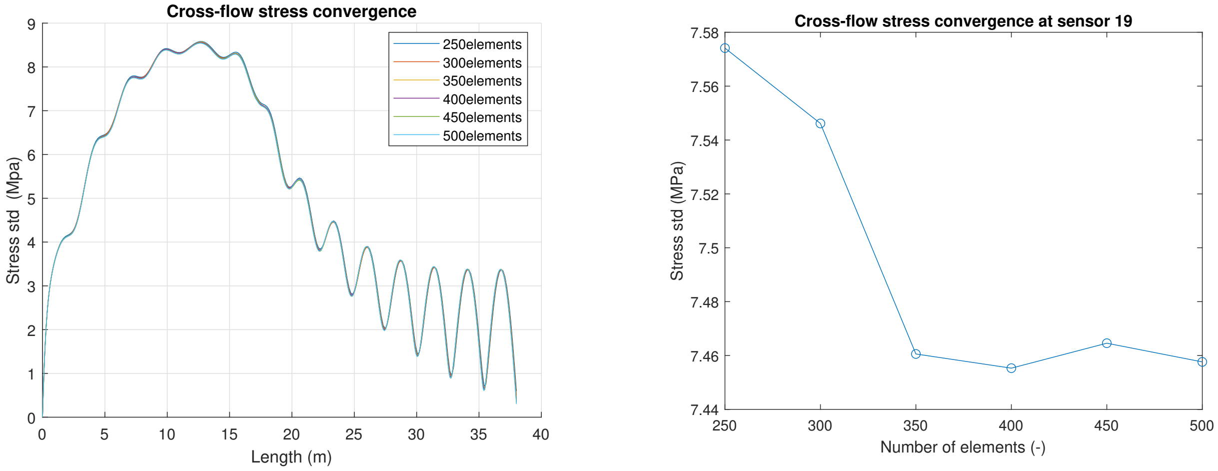

(a) Stress std along riser (b) Stress std at sensor 19 location

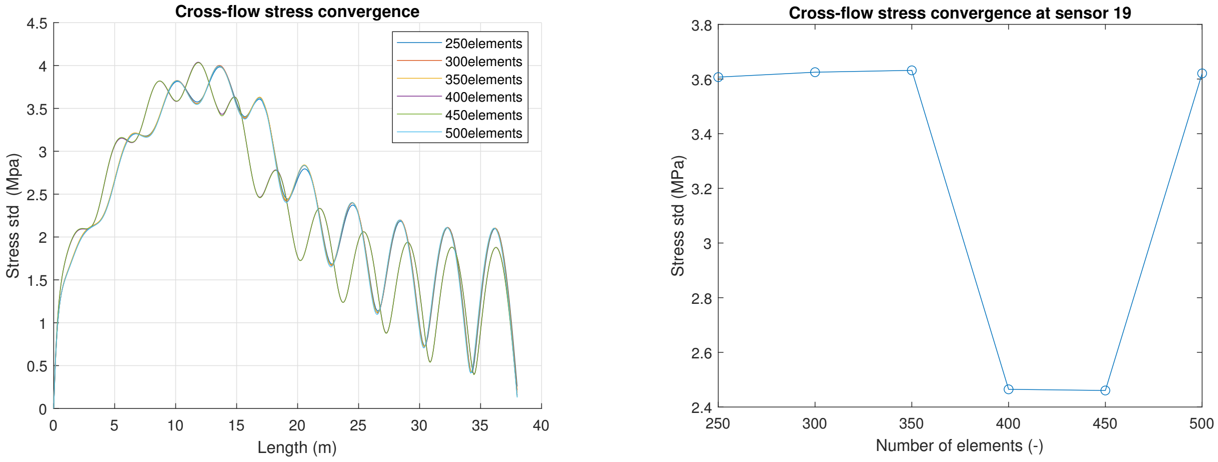

(c) Stress std along riser (d) Stress std at sensor 19 location

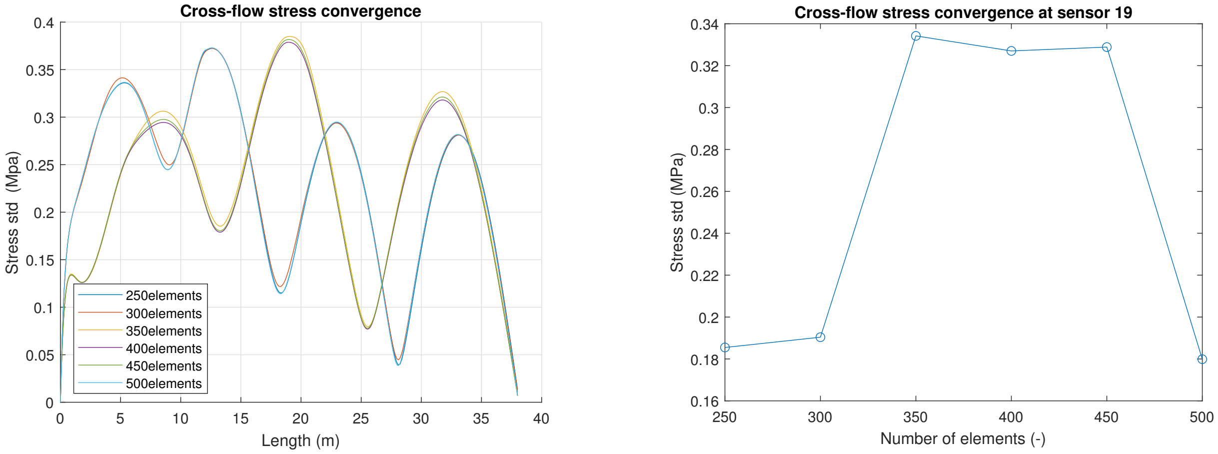

(e) Stress std along riser (f) Stress std at sensor 19 location

Figure 3.18: Cross-flow stress convergence for NDP shear flow cases
Current speeds: (a)-(b): $2.4m/s$, (c)-(d): $1.5m/s$, (e)-(f): $0.5m/s$

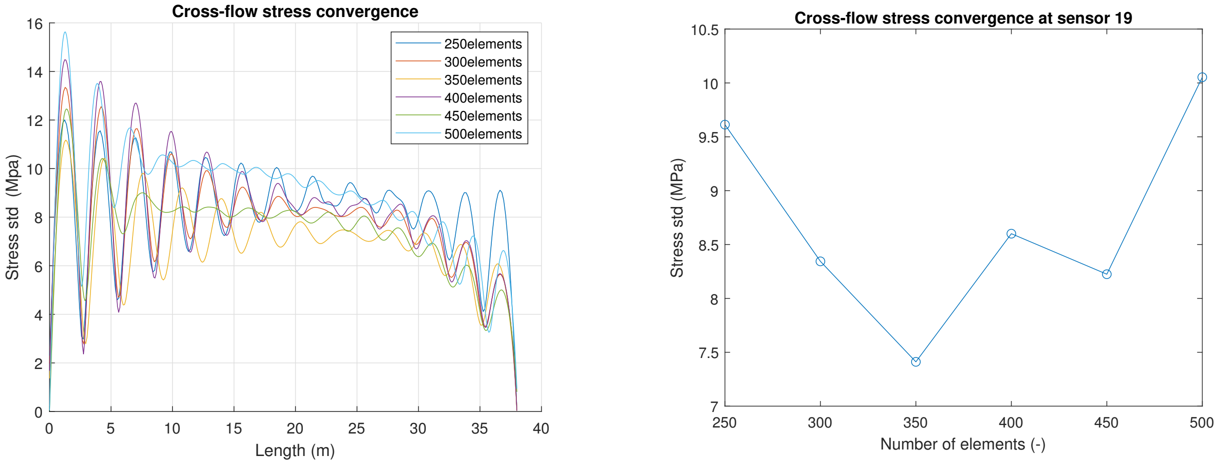

(a) Stress std along riser (b) Stress std at sensor 19 location

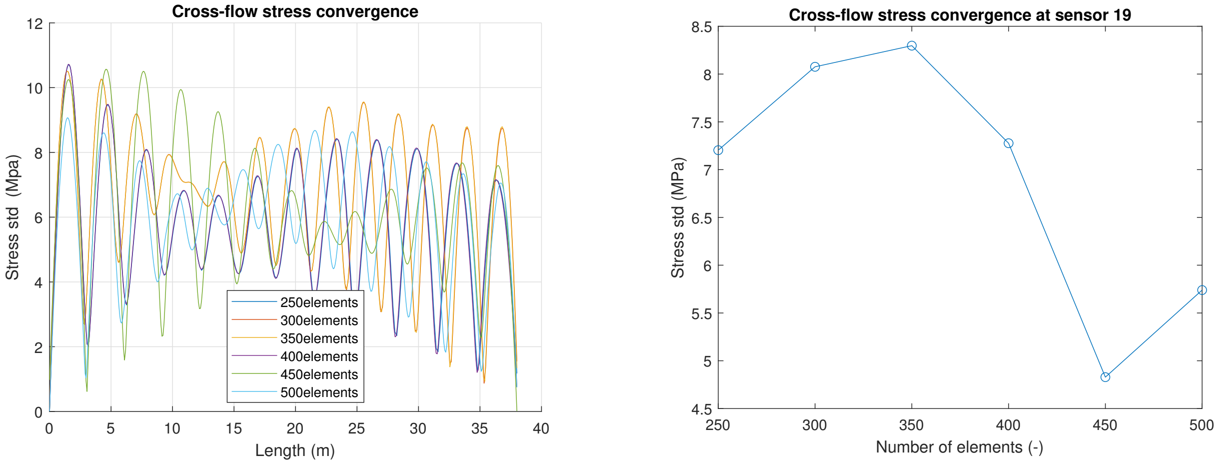

(c) Stress std along riser (d) Stress std at sensor 19 location

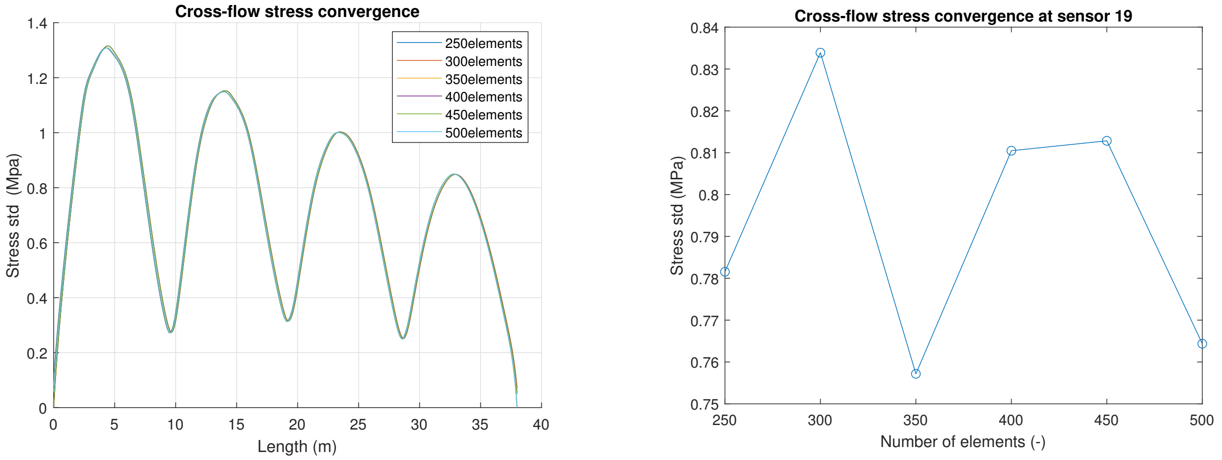

(e) Stress std along riser (f) Stress std at sensor 19 location

Figure 3.19: Cross-flow stress convergence for NDP uniform flow cases
Current speeds: (a)-(b): $2.4m/s$, (c)-(d): $1.5m/s$, (e)-(f): $0.5m/s$

### 3.8.3 Sensitivity study of the hydrodynamic coefficients in normal direction for straked riser sections

**Variation of the normal quadratic drag coefficient**

Some uncertainties were related to the computation of the quadratic drag coefficient for straked sections given as input to Riflex. It was found from the non-dimensional drag coefficient according to Equation (3.2.4), where a projected area per unit length $B_y/B_z$ had to be chosen. $B_y$ and $B_z$ were set equal and were in Section 3.2.3 set to $D+H$, i.e. the height of a strake was added to the diameter of the bare pipe. In reality the projected area per unit length will not be constant along the straked section due to the strakes are winded around the bare pipe and not aligned with the pipe axis. Hence a sensitivity study was performed in order to evaluate the effect of using different $B_y/B_z$.

Table 3.7: Quadratic drag force coefficients for three choices of projected area per length $B_y/B_z$ for straked riser section

| $\mathbf{B_y/B_z}$ | **Quadratic drag coefficient for straked riser section [kg/m$^2$]** |
|---|---|
| $D$ | 19.59 |
| $D+H$ | 24.49 |
| $D+2H$ | 29.39 |

Three choices of $B_y/B_z$ were considered: $D$, $D+H$ and $D+2H$, and the non-dimensional drag coefficient was computed based on a drag coefficient for bare pipe of 0.9. The associated drag coefficients for the three choices of $B_y/B_z$ are given in Table 3.7. Cases with 50% strake coverage exposed to both shear and uniform flow with six speeds from $0.3m/s$ to $2.3m/s$ were simulated. It was looked into both the displacement and stress response, but as the simulations showed the same trend for both displacements and stresses it was found appropriate to present only plots of the stress response. Plots of the cross-flow and in-line stress standard deviation for a representative shear and uniform flow case are seen in Figure 3.20 and 3.21, respectively. The shear flow cases show that if $B_y/B_z$ was increased the response was decreased in the straked pipe section (from 0 to $19m$), while the difference in response in the bare pipe section (from 19 to $38m$) was negligible. For the uniform flow cases the same trend was observed for the straked section as for the shear flow cases, but the effect on the bare section was seen to be larger. The predictions were of the same order of magnitude, but different modes were dominating the response. In order to illustrate this the spectra of the cross-flow and in-line stress at the position of maximum stress response are shown in Figure 3.22, where it is seen that a higher natural frequency was excited when performing simulations with the lowest drag coefficient. However, no clear tendency of whether a small or large drag coefficient excited a higher mode was observed over the range of cases considered; for some speeds the response in the case with highest drag coefficient excited a higher mode than the cases with lower drag coefficients.

Overall small differences were seen for the different choices of $B_y/B_z$, and it was hence decided to stick to the initial choice of $B_z/B_y = D+H$.

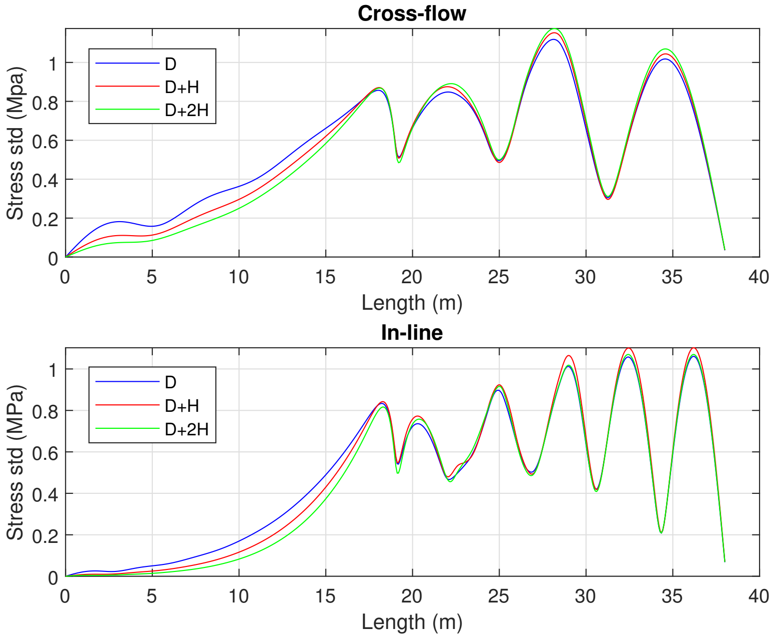

Figure 3.20: NDP shear flow case: stress std comparison of three alternatives for computing the quadratic drag coefficient
Current speed: $1.9 m/s$. Strake coverage: 50%

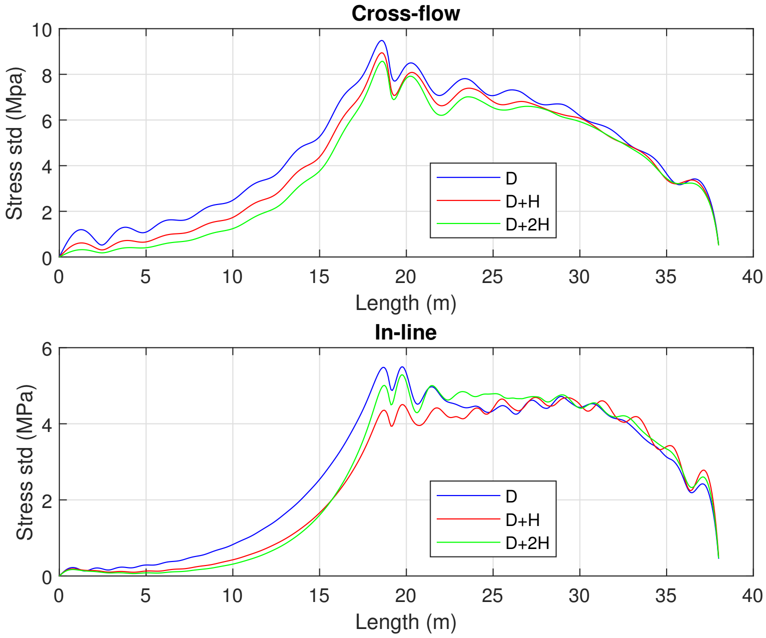

Figure 3.21: NDP uniform flow case: stress std comparison of three alternatives for computing the quadratic drag coefficient
Current speed: $1.9 m/s$. Strake coverage: 50%

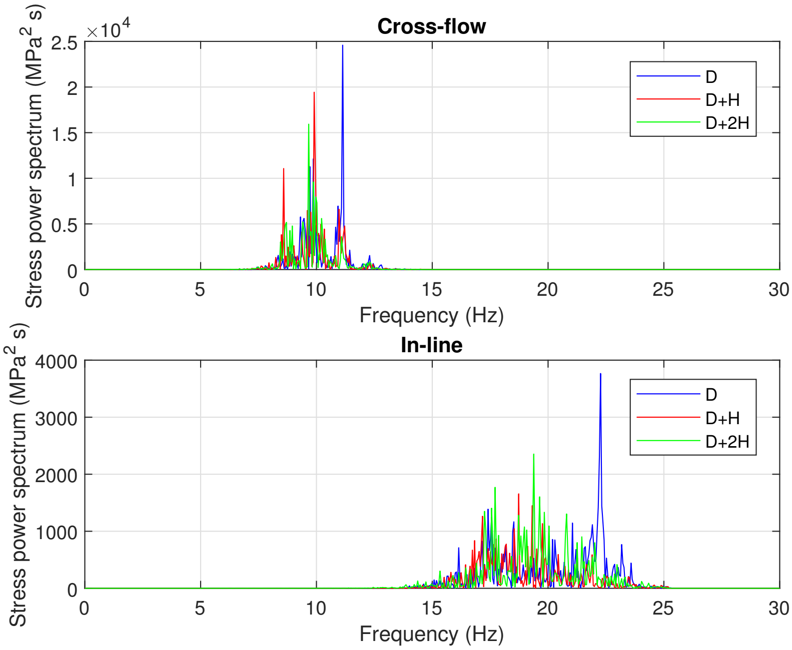

Figure 3.22: NDP uniform flow case: stress spectrum comparison of three alternatives for computing the quadratic drag coefficient
Current speed: $1.9m/s$. Strake coverage: 50%

### Different added mass coefficients in local y- and z-direction

In Section 3.3 it was discovered that experimental results yielded different added mass coefficients in cross-flow and in-line direction, while the analytical formulations did not distinguish between cross-flow and in-line. In this section the effect of applying different added mass coefficients in local y- and z-direction is evaluated. This is done by comparing simulations with the experimental cross-flow and in-line added mass coefficients (found by Senga [38]) and simulations where the analytical normal added mass coefficient (found from equations in Section 3.1.1) was applied in both local y- and z-direction. In Table 3.8 the added mass coefficients that were applied are presented. Both uniform and shear flow were considered with 22 speeds from $0.3$-$2.4m/s$, and the pipe had 50% strake coverage (i.e. covered with strakes from 0 to $19m$ in the presented plots).

Table 3.8: Experimental and analytical added mass coefficients for straked pipe section

| | **Experimental** | **Analytical** |
|---|---|---|
| **Added mass coefficient in local y-direction $\mathbf{C_{my}}$[-]** | 2.2 | 1.5 |
| **Added mass coefficient in local z-direction $\mathbf{C_{mz}}$[-]** | 1.5 | 1.5 |

The figures presented in this section contain legends where "Exp: $C_{my} \neq C_{mz}$" refers to the cases with experimental added mass coefficients, while "Ana: $C_{my} = C_{mz}$" refers to the cases with analytical added mass coefficients. To have an idea of which of the two alternatives that provided the best predictions the measurements from the NDP experiments were also included in the plots and were given the legend "Meas".

In general small effects were seen from applying the experimental added mass coefficients compared to applying the analytical added mass coefficients: the displacement and stress response level was of the same order of magnitude for all the evaluated cases. For all shear flow cases, except the two cases with highest speeds, the in-line response in the straked section was slightly larger when applying the experimental coefficients. Apart from that negligible differences were observed for these cases, which is illustrated by a representative case with current speed $2.2m/s$ in Figure 3.23. At the two highest current speeds slightly different predictions both cross-flow and in-line were obtained, see Figure 3.24.

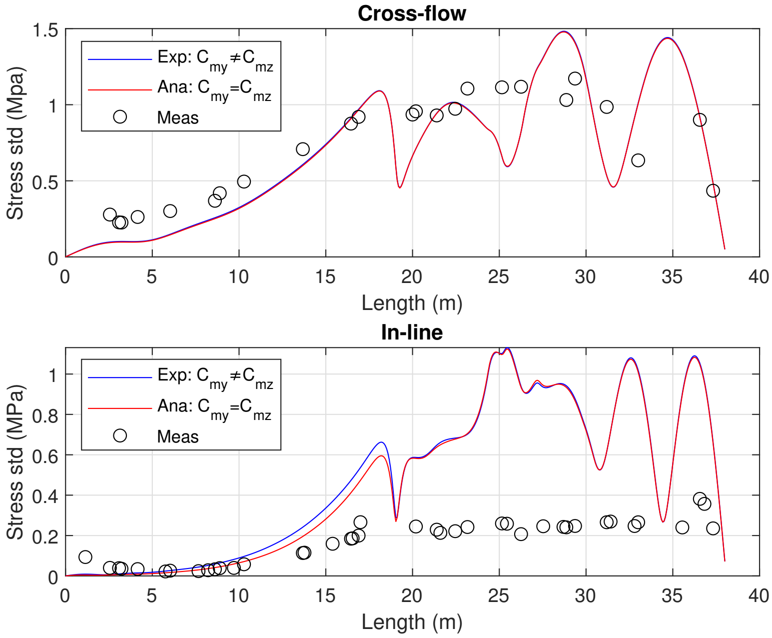

Figure 3.23: NDP shear flow case: Comparison of simulations with experimental and analytical added mass coefficients for straked section with small differences
Current speed: $2.2m/s$. Strake coverage: 50%

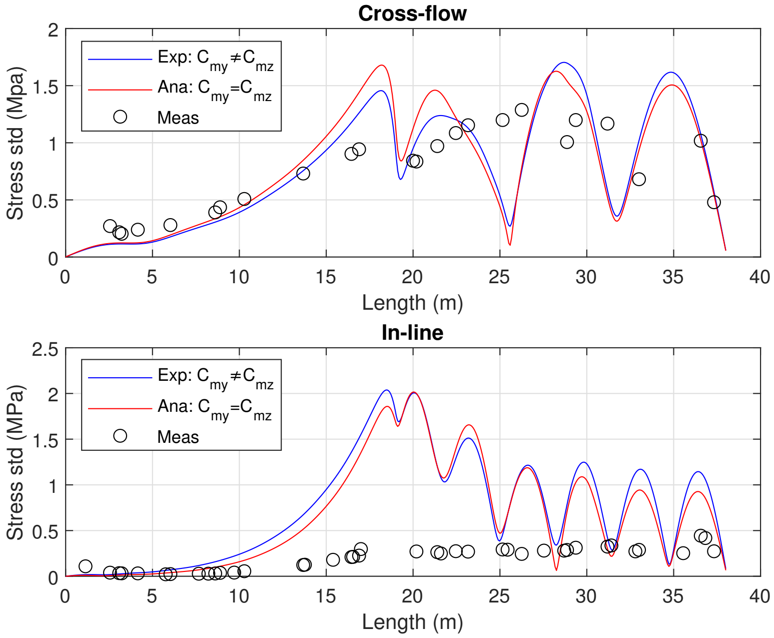

Figure 3.24: NDP shear flow case: Comparison of simulations with experimental and analytical added mass coefficients for straked section with clear differences
Current speed: $2.3 m/s$. Strake coverage: 50%

Two main trends were observed in the uniform flow cases:

1. If the in-line response in the straked section was larger with the experimental coefficients, negligible differences in the cross-flow response were seen. The in-line response in the bare section did in these cases not follow a clear trend.
2. If there were small differences in the in-line response in the straked section, the response in the bare section with the analytical coefficients were in general largest. Cross-flow the response with the experimental coefficients was largest for these cases over the entire length of the riser.

The two trends described above are illustrated in Figure 3.25 and 3.26. When it comes to comparing the predictions with the measurements, no clear improvement was seen when applying the experimental added mass coefficient in the local y-direction. Thus it was decided to move on with the added mass coefficients found from the analytical formulations.

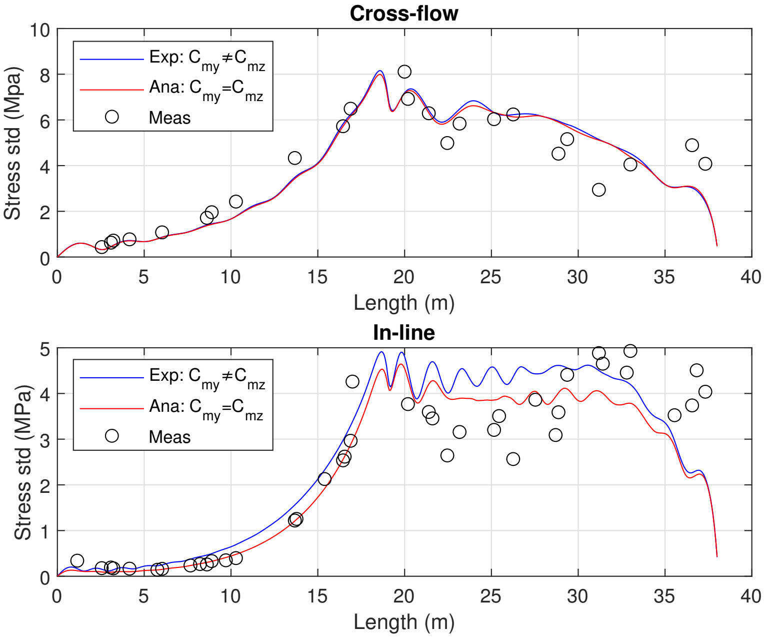

Figure 3.25: NDP uniform flow case: Comparison of simulations with experimental and analytical added mass coefficients for straked section: Trend 1
Current speed: $1.8m/s$. Strake coverage: 50%

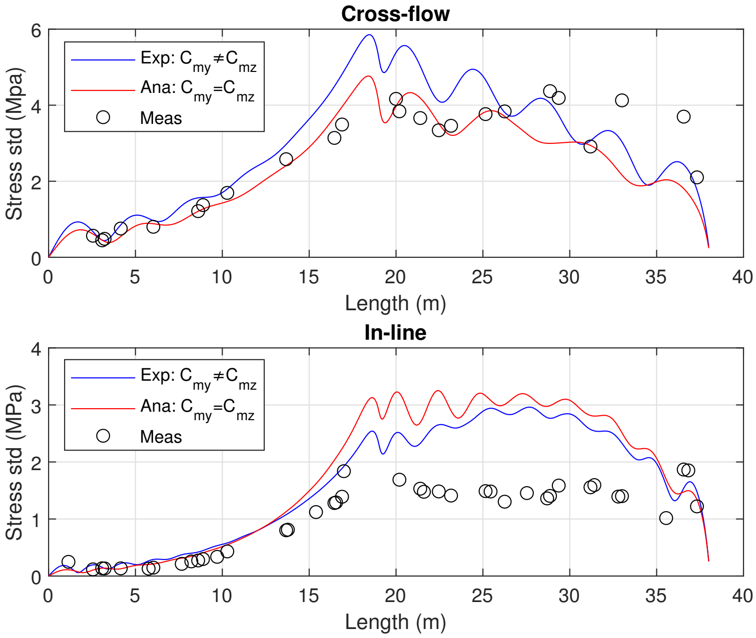

Figure 3.26: NDP uniform flow case: Comparison of simulations with experimental and analytical added mass coefficients for straked section: Trend 2
Current speed: $1.2m/s$. Strake coverage: 50%

## 3.9 Final load model with empirical constants

The empirical parameters that resulted from the calibration described in Section 3.6 are presented in Table 3.9 for the bare riser section and in Table 3.10 for the straked riser section. These are the parameters that were used for obtaining the results of this thesis. $C_{hh}$ was set to zero in all simulations, i.e. only the fundamental VIV response was investigated in this thesis. Also note that the calibration resulted in a quadratic drag coefficient equal to 0.9 and that the initial value of $C_{res} = 1.2$ was increased to $C_{res} = 1.3$, where $C_{v,x}$ was increased and $C_{v,y}$ was the same as in the initial model. In Table 3.10 the parameters given as input to INPMOD are bold, while the non-dimensional parameters are included here in order to better be able to compare the parameters for straked sections to the parameters for bare sections.

Table 3.9: Final model: Hydrodynamic coefficients for bare riser section

| **Parameter** | **Magnitude** |
|---|---|
| Quadratic drag coefficient in tangential direction [-] | 0 |
| Quadratic drag coefficient in normal direction [-] | 0.9 |
| Added mass per unit length in tangential direction [-] | 0 |
| Added mass per unit length in normal direction [-] | 1 |
| Hydrodynamic diameter [m] | 0.027 |
| $C_{v,y}$ [-] | 0.85 |
| $C_{v,x}$ [-] | 0.98 |
| $\hat{f}_0$ [-] | 0.144 |
| $\hat{f}_{min}$ [-] | 0.08 |
| $\hat{f}_{max}$ [-] | 0.208 |
| $\alpha$ [-] | 0.15 |
| $C_{hh}$ [-] | 0 |

Table 3.10: Final model: Hydrodynamic coefficients for straked riser section

| **Parameter** | **Magnitude** |
|---|---|
| Non-dimensional quadratic drag coefficient for local x-direction [-] | 0.0383 |
| **Quadratic drag coefficient for local x-direction [kg/m$^2$]** | **1.6253** |
| Non-dimensional quadratic drag coefficient for local y-direction [-] | 1.4513 |
| **Quadratic drag coefficient for local y-direction [kg/m$^2$]** | **24.4898** |
| Non-dimensional quadratic drag coefficient for local z-direction [-] | 1.4513 |
| **Quadratic drag coefficient for local z-direction [kg/m$^2$]** | **24.4898** |
| Non-dimensional added mass in local x-direction [-] | 0.0021 |
| **Added mass per length in local x-direction [kg/m]** | **0.0012** |
| Non-dimensional added mass in local y-direction [-] | 1.5078 |
| **Added mass per length in local y-direction [kg/m]** | **0.8633** |
| Non-dimensional added mass in local z-direction [-] | 1.5078 |
| **Added mass per length in local z-direction [kg/m]** | **0.8633** |

# Chapter 4

# Case study

The Norwegian Deepwater Programme (NDP) was a cooperation program that was formed in 1996 and completed in 2016. It consisted of oilfield licenses on the Norwegian continental shelf (NCS). The objective of the organization was to cooperate in order to ensure safe drilling and field development. Investigation of VIV was an important part of the work done by the NDP, which funded several experimental VIV projects according to Baarholm [43]. One of these projects was the "High Mode VIV model tests"-project performed at MARINTEK in the Offshore Basin in December 2003. The objectives for these tests were the following according to Trim et al. [8]:

- "Acquire data to improve understanding of high-mode VIV of long risers in different current profiles."
- "Provide benchmark information for calibration and validation of codes that predict riser response."
- "Assess suppression effectiveness of strakes with different geometries and different percentage coverage over the riser length."

This case study is based on the MARINTEK reports [31] and [44], which describe the experiments and present some results, as well as the paper by Trim et al. [8].

## 4.1 General set up

In the tests a $38m$ long fiberglass riser model with outer diameter $D_o = 0.027m$ and inner diameter $D_i = 0.021m$ was towed at 22 different speeds in both uniform and sheared current with water temperature 18°C. The speed range was 0.3-$2.4m/s$, i.e. experiments at speeds at every $0.1m/s$ within the interval were performed. The riser was not exposed of waves. The riser was open in the ends during the experiments, and was hence waterfilled. In Figure 4.1 (a) it is shown how an orthogonal right-handed coordinate system was defined for the tests, with origin in the bottom end of the riser with the x-axis pointing in the direction of the current. Figure 4.1 (b) and (c) illustrate how the stationary uniform and sheared currents are generated, namely by towing of the entire system at constant speed and by rotation of the upper riser end (the gondola side) with constant rotational speed about the origin.

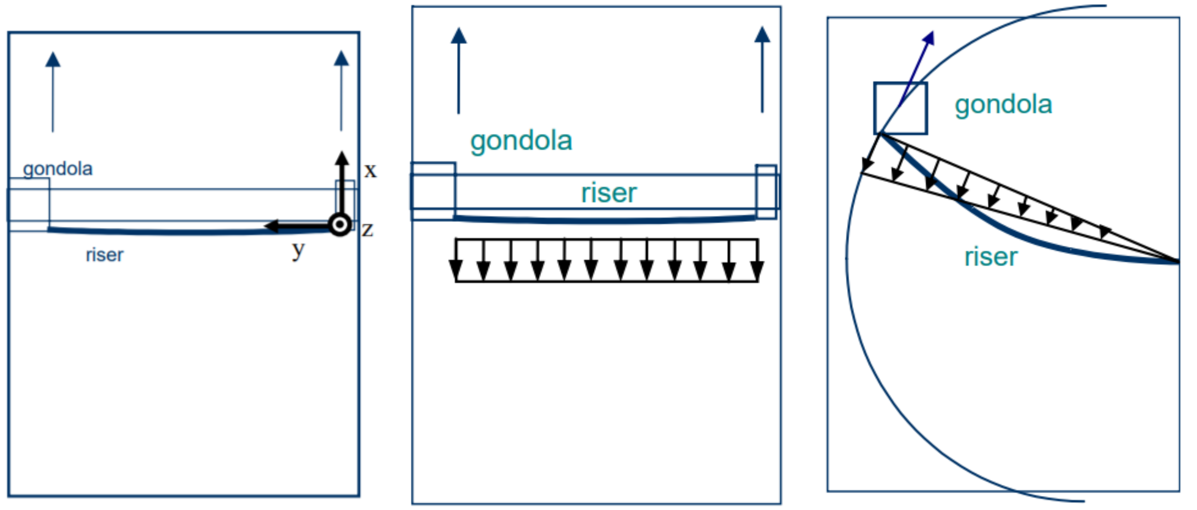

(a) Coordinate system (b) Realization of uniform speed distribution (c) Realization of shear speed distribution

Figure 4.1: Coordinate system and current realizations in the NDP High Mode VIV tests

The tests were performed both with a bare pipe and with helical strakes fitted to the pipe. Two types of strakes, both with $N = 3$ strakes, were tested: one with pitch to diameter ratio $(P/D)_1 = 17.5$ and height to diameter ratio $(H/D)_1 = 0.25$ referred to as 17.5D/0.25D and the other with $(P/D)_2 = 5$ and $(H/D)_2 = 0.14$ referred to as 5D/0.14D. Each of the two types of strake geometry involved a set of partial strake coverage configurations: 91%, 81%, 62% and 41%. It should be noted that due to the need of various instruments for measurements along the riser, 100% coverage was not possible to achieve. This means that the 91% coverage case corresponds to when the entire riser was covered with strakes, except the instrumentation gaps. Equivalently 41% and 62% coverage refer to when the upper 50% and 75% of the riser were covered with strakes.

In order to perform the experiments the test riser had to be connected to a test rig. The rig-riser interaction should be limited as the connected features will not be present for a real riser offshore. This was achieved by attaching clump weights at the two riser ends. The clump weights were connected to the crane/gondola (depending on the riser end) by pendulum arms and a vertical spring, see Figure 4.2. The clump weights each had a mass equal to $520kg$, causing the bending modes of the the pendulum arms to be low-frequent, i.e. outside of the riser bending mode frequency range. In addition the clump weight at the upper end of the riser included a heave compensator with two sets of springs with a total stiffness of $9333N/m$. The purpose of the heave compensator was to control the natural frequencies and stiffness in the riser axial direction.

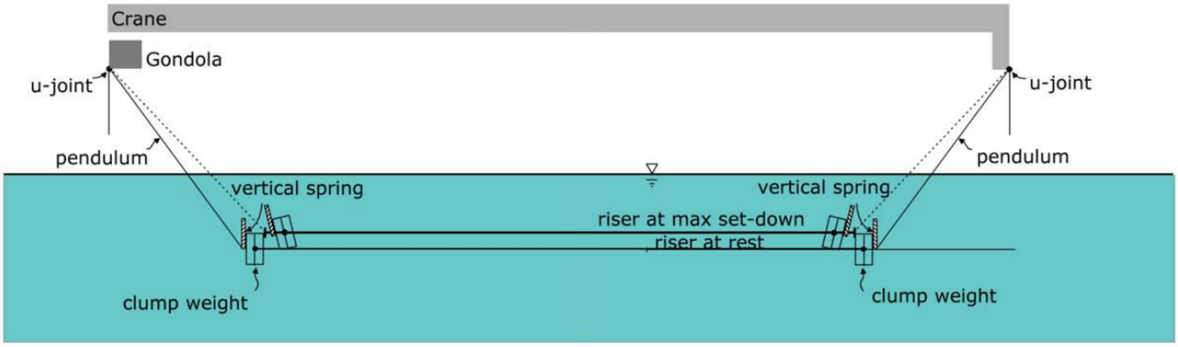

Figure 4.2: Simple schematic of the test rig for the NDP High Mode VIV tests

As previously mentioned, real marine risers typically have tension-dominated bending modes, and this was achieved in the tests by setting the diameter of the riser model low and hence reducing the bending stiffness. For the experiments with strake coverage the bending stiffness for the strakes was found to be of the same order of magnitude as for the riser and thus neglected due to the tension domination of the riser eigenfrequencies. A pre-tension of $3000N$ was applied to the test riser, making sure realistic conditions were established. The tension in the riser was increased from the pre-tension due to the in-line drag force induced by the incoming flow, and the mean effective tension was within the range 3600-$6300N$ for all tests.

A large number of instruments were used to measure the VIV response of the test riser, and there could have been more had it not been for the limitations regarding the internal space of the riser and the size of the sensor cables. The instrumentation gaps are not equally spaced along the riser, but an algorithm was used to achieve good positioning of the sensors. The two main instruments used were accelerometers and strain gauge transducers positioned along the riser. There were eight accelerometers measuring in-line and cross-flow accelerations and 24 and 40 strain gauge transducers cross-flow and in-line, respectively. In Table 4.1 the positions of the sensors are shown.

Table 4.1: Sensor positions along the test riser measured from the top end
SCF/SIL: cross-flow/in-line strain gauge, ACC: accelerometer

| **Sensor number** | **Sensor type** | **Position** [m] | **Sensor number** | **Sensor type** | **Position** [m] |
|---|---|---|---|---|---|
| 1 | SIL | 1.143 | 21 | SCF/SIL | 20.193 |
| 2 | SCF/SIL | 2.555 | 22 | ACC/SCF/SIL | 21.393 |
| 3 | SCF/SIL | 3.084 | 23 | SIL | 21.603 |
| 4 | SCF/SIL | 3.224 | 24 | SCF/SIL | 22.460 |
| 5 | ACC/SCF/SIL | 4.155 | 25 | SCF/SIL | 23.165 |
| 6 | SIL | 5.759 | 26 | ACC/SCF/SIL | 25.153 |
| 7 | SCF/SIL | 6.030 | 27 | SIL | 25.442 |
| 8 | SIL | 7.664 | 28 | SCF/SIL | 26.254 |
| 9 | SIL | 8.216 | 29 | SIL | 27.532 |
| 10 | ACC/SCF/SIL | 8.609 | 30 | SIL | 28.698 |
| 11 | SCF/SIL | 8.889 | 31 | ACC/SCF/SIL | 28.863 |
| 12 | SIL | 9.703 | 32 | SCF/SIL | 29.365 |
| 13 | SCF/IL | 10.285 | 33 | SCF/SIL | 31.191 |
| 14 | ACC/SCF/IL | 13.676 | 34 | SIL | 31.415 |
| 15 | SIL | 13.772 | 35 | SIL | 32.796 |
| 16 | SIL | 15.393 | 36 | ACC/SCF/SIL | 33.005 |
| 17 | SCF/SIL | 16.452 | 37 | SIL | 35.549 |
| 18 | SIL | 16.547 | 38 | SCF/SIL | 36.559 |
| 19 | ACC/SCF/SIL | 16.891 | 39 | SIL | 36.824 |
| 20 | SCF/SIL | 19.997 | 40 | SCF/SIL | 37.322 |

## 4.2 Results of the experiments

Both the strake geometries exhibited good capabilities in regard to reducing VIV. The 17.5D/0.25D geometry reduced the in-line and cross-flow response of the test riser the most, and the difference in VIV suppression effectiveness between the two geometries was clearest for the cases with uniform current. For the experiments with high riser coverage, 91% and 82%, small differences with respect to strakes suppression performance were seen, but when reducing the coverage to 62% and 41% the performance was significantly decreased in uniform flow. In shear flow 62% coverage did not reduce the suppression performance much compared to 82% and 91%, while 41% were seen to partly suppress the response, but not as much as the configurations with higher coverage. The in-line fatigue damage turned out to be equally important as cross-flow fatigue damage, underlining the importance of including the in-line contribution to VIV fatigue prediction tools.

## 4.3 Cases studied in the thesis

As the experiments with high riser coverage almost completely suppressed VIV it would make little sense to simulate these cases with the TD VIV model. It was considered more interesting to look into the cases with less strake coverage so the cases with 41% and 62% strake coverage in uniform and sheared current were selected, in addition to the cases with bare pipe. Note that only every second current speed in the range $0.3 - 2.4 m/s$ was tested with 62% strake coverage. As the 17.5D/0.25D strakes geometry is most commonly used in the industry and considering the fact that it exhibited better suppression efficiency than the 5D/0.14D strakes geometry, it was the geometry that was studied in this thesis. The cases to be studied, with parameters relevant for input to the simulation model, are presented in Table 4.2 and 4.3.

Table 4.2: Physical properties of the NDP test riser

| Parameter | Magnitude |
|---|---|
| Riser length $[m]$ | 38 |
| Riser outer diameter $[m]$ | 0.027 |
| Riser inner diameter $[m]$ | 0.021 |
| Strake pitch $[m]$ | 17.5D |
| Strake height $[m]$ | 0.25D |
| Outer diameter of fins $[m]$ | 0.033 |
| Strake coverage [%] | 0/41/62 |
| Bending stiffness, EI $[Nm^2]$ | 599 |
| Young's modulus, E $[N/m^2]$ | $36.2 \cdot 10^9$ |
| Axial stiffness, EA $[N]$ | $8.19 \cdot 10^6$ |
| Torsional stiffness, GJ $[Nm^2/rad]$ | 491 |
| Mean effective tension, T $[N]$ | 3600-6300 |
| Tension capacity $[N]$ | 50 000 |
| Mass bare test riser $[kg/m]$ | 0.933 |
| Mass straked test riser $[kg/m]$ | 1.233 |

Table 4.3: Environmental data for test cases

| Parameter | Magnitude |
|---|---|
| Water temperature $[°C]$ | 18 |
| Water density $[kg/m^3]$ | 1000 |
| Water kinematic viscosity $[m^2/s]$ | $10^{-6}$ |
| Air density $[kg/m^3]$ | 1.2 |
| Air kinematic viscosity $[m^2/s]$ | $1.5 \cdot 10^{-5}$ |
| Water depth $[m]$ | 10 |
| Current speed (uniform/shear) $[m/s]$ | 0.3-2.4 |

Note that the bending stiffness $EI$ was found from a bending test with the test riser and that the bending stiffness contribution from the strakes is neglected. Young's modulus and the axial stiffness were found from $EI$ and the cross section geometry of the test riser. The presence of strakes is not included in the cross section geometry for these calculations. The mass of the straked riser given in Table 4.2 is the sum of the mass contributions from the fiber glass test riser, the water inside the riser, the mass of the sensor cables and the mass of the strakes. Also be aware that the tension capacity given here was found by a strength test of a pipe section, and at this tension level the pipe section had not yet collapsed.

# Chapter 5

# Results and discussion

An evaluation of the model performance is presented in this chapter. The evaluation is mainly focused on the model's capability of predicting cross-flow and in-line stresses and fatigue, but also displacements are evaluated by comparison with the results of the selected NDP experiments presented in Section 4.3. The results were obtained by use of the load model parameters given in Table 3.9 and 3.10. First the bare pipe cases are considered, before the 41% and 62% partial strake coverage cases are looked into. Note that the instrumentation gaps that were present between the strakes in the NDP experiments (see Section 4.1) were not accounted for in the Riflex simulations: 50% and 75% strake coverage without gaps were simulated. A wide range of scenarios are evaluated here: both shear and uniform flow with current speeds from 0.3-2.4$m/s$. The evaluation is done in order to reveal how robust the model is for bare pipe simulations, as well as investigating if accurate predictions of VIV response for pipes with partial strake coverage are achievable.

Many of the plots in this chapter contain labels: "Sim" and "Exp" represent the results from the time domain simulations and the NDP experiments, respectively, and some plots have an extension "CF" and "IL" which refer to cross-flow and in-line. The current speed will in some cases simply be referred to as $U$ and $\sigma_{disp}$ is the displacement standard deviation. For the presentation of the results a notation system is used, where each case is associated with a single notation. The notations will consist of three terms:

- **0/41/62.** This term refers to the level of strake coverage. 0 refers to the bare pipe cases, 41 to the cases with 41% strake coverage and 62 to the cases with 62% strake coverage.
- **U/S.** This term refers to whether the pipe is exposed to a uniform or sheared current. U refers to uniform current and S refers to linearly sheared current.
- **0.3-2.4.** This term refers to the current speed. If a linearly sheared current is considered this term refers to the maximum speed.

All the case notations are presented in Table 5.1.

Table 5.1: Case notations

| **Current profile** | **Current speed [m/s]** | **Bare** | **41% strake coverage** | **62% strake coverage** |
|---|---|---|---|---|
| Uniform | 0.3 | 0U0.3 | 41U0.3 | |
| | 0.4 | 0U0.4 | 41U0.4 | 62U0.4 |
| | 0.5 | 0U0.5 | 41U0.5 | |
| | 0.6 | 0U0.6 | 41U0.6 | 62U0.6 |
| | 0.7 | 0U0.7 | 41U0.7 | |
| | 0.8 | 0U0.8 | 41U0.8 | 62U0.8 |
| | 0.9 | 0U0.9 | 41U0.9 | |
| | 1.0 | 0U1.0 | 41U1.0 | 62U1.0 |
| | 1.1 | 0U1.1 | 41U1.1 | |
| | 1.2 | 0U1.2 | 41U1.2 | 62U1.2 |
| | 1.3 | 0U1.3 | 41U1.3 | |
| | 1.4 | 0U1.4 | 41U1.4 | 62U1.4 |
| | 1.5 | 0U1.5 | 41U1.5 | |
| | 1.6 | 0U1.6 | 41U1.6 | 62U1.6 |
| | 1.7 | 0U1.7 | 41U1.7 | |
| | 1.8 | 0U1.8 | 41U1.8 | 62U1.8 |
| | 1.9 | 0U1.9 | 41U1.9 | |
| | 2.0 | 0U2.0 | 41U2.0 | 62U2.0 |
| | 2.1 | 0U2.1 | 41U2.1 | |
| | 2.2 | 0U2.2 | 41U2.2 | 62U2.2 |
| | 2.3 | 0U2.3 | 41U2.3 | |
| | 2.4 | 0U2.4 | 41U2.4 | 62U2.4 |
| Sheared | 0.3 | 0S0.3 | 41S0.3 | |
| | 0.4 | 0S0.4 | 41S0.4 | 62S0.4 |
| | 0.5 | 0S0.5 | 41S0.5 | |
| | 0.6 | 0S0.6 | 41S0.6 | 62S0.6 |
| | 0.7 | 0S0.7 | 41S0.7 | |
| | 0.8 | 0S0.8 | 41S0.8 | 62S0.8 |
| | 0.9 | 0S0.9 | 41S0.9 | |
| | 1.0 | 0S1.0 | 41S1.0 | 62S1.0 |
| | 1.1 | 0S1.1 | 41S1.1 | |
| | 1.2 | 0S1.2 | 41S1.2 | 62S1.2 |
| | 1.3 | 0S1.3 | 41S1.3 | |
| | 1.4 | 0S1.4 | 41S1.4 | 62S1.4 |
| | 1.5 | 0S1.5 | 41S1.5 | |
| | 1.6 | 0S1.6 | 41S1.6 | 62S1.6 |
| | 1.7 | 0S1.7 | 41S1.7 | |
| | 1.8 | 0S1.8 | 41S1.8 | 62S1.8 |
| | 1.9 | 0S1.9 | 41S1.9 | |
| | 2.0 | 0S2.0 | 41S2.0 | 62S2.0 |
| | 2.1 | 0S2.1 | 41S2.1 | |
| | 2.2 | 0S2.2 | 41S2.2 | 62S2.2 |
| | 2.3 | 0S2.3 | 41S2.3 | |
| | 2.4 | 0S2.4 | 41S2.4 | 62S2.4 |

To avoid confusion regarding which part of the riser is exposed to high or low speed in the shear flow cases, the shear current as function of riser length is shown in Figure 5.1. The current speed along the riser $U(z)$ is normalized by the the maximum current speed $U_{max}$.

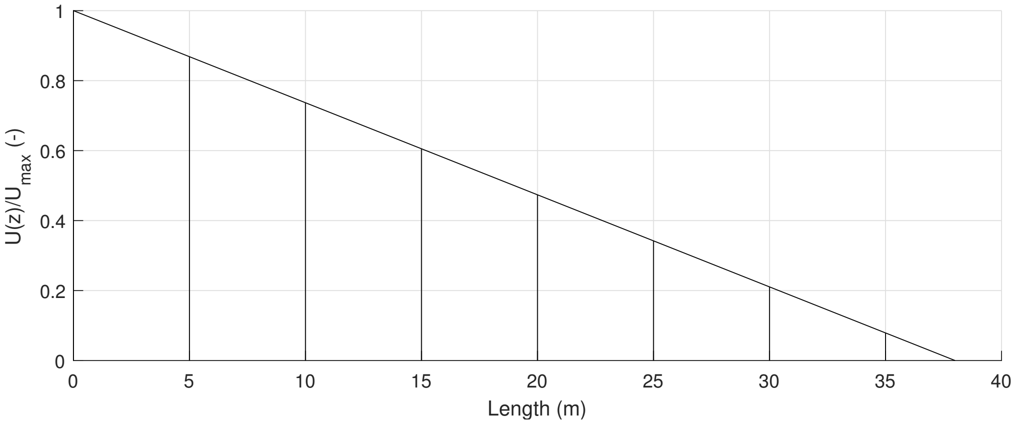

Figure 5.1: Shear current as function of riser length

## 5.1 Bare pipe

Prior to investigating the model performance for the cases with strake coverage it had to be verified that the model could predict the VIV response of bare pipes, which this section is devoted to.

### 5.1.1 Shear flow

Figure 5.2 shows how the dominating frequency both cross-flow and in-line depend on the current speed. The close agreement between the cross-flow dominating frequencies from the experiments and the simulations gives a good indication that the synchronization range, defined by $\hat{f}_0$, $\hat{f}_{min}$ and $\hat{f}_{max}$, and the structural model are defined properly. Also the in-line dominating frequencies are predicted well, which confirms that the in-line synchronization model (with $\alpha = 0.15$) is well defined and that the experimental agreement is good both cross-flow and in-line.

Observe how the cross-flow dominating frequency may be almost equal for two or three adjacent current speeds (e.g. experiment 1.9-2.1$m/s$) before the dominating frequency jumps to a new level (2.2-2.4$m/s$). A feature when a pipe is exposed to shear flow is that a range of natural frequencies may be exited. The same natural frequency may hence still be the dominating frequency even though higher natural frequencies are exited when the maximum speed is increased. Increasing the current speed further may introduce even higher natural frequencies and, if they dominate, cause a jump in the level of dominating frequency. This is illustrated by the predicted cross-flow stress power spectrum at the position of maximum stress response for case 0S2.3 and 0S2.4 in Figure 5.3. Note that the largest deviations between simulation and experiment results are seen when the model predicts that the jump occurs at wrong speed (e.g. at 2.4$m/s$). On the other hand, the model manages quite well to capture this effect and that is considered more important than that the jump is predicted 0.1$m/s$ "too late" or "too soon" for some cases.

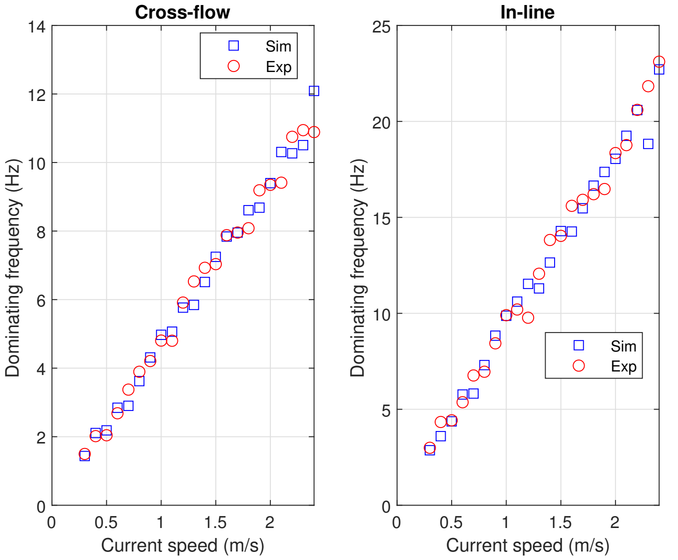

Figure 5.2: Dominating frequencies for bare pipe in shear flow for current speeds 0.3-2.4$m/s$

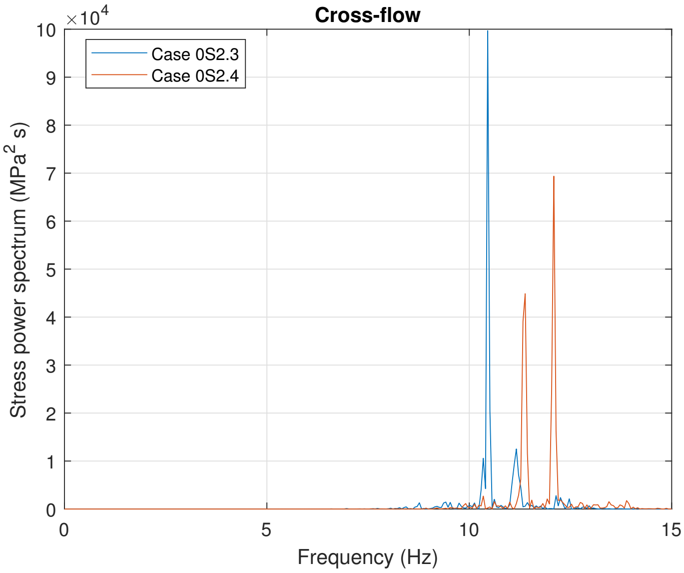

Figure 5.3: Feature of shear flow conditions: jump in dominating frequency when increasing the current speed

The space averaged values of the stress standard deviation as function of current speed are presented in Figure 5.4 (a). It shows a clear improvement from the results with the initial hydrodynamic load parameters presented in Section 3.6.1, and both the cross-flow and in-line stress are predicted well for speeds lower than 1.5$m/s$. For higher speeds conservative results are obtained cross-flow, while some in-line measurements, such as U=1.7$m/s$ and U=2.1$m/s$, are much larger than at the adjacent speeds which causes very non-conservative predictions. If these exceptional observations are set side the predictions are seen to be quite accurate. In Figure 5.4 (b) it is illustrated that the maximum annual fatigue damage is predicted very well for most speeds cross-flow. The largest disagreements are observed at the highest and lowest speed, where the prediction is conservative at U=2.4$m/s$ and non-conservative at U=0.3$m/s$. However, that the model predicts that the structure endures 100 000 years and the measurements show that failure occurs after 10 000 years has no practical significance. In-line the fatigue damage is either predicted well, or overestimated, for most speeds. The largest non-conservative predictions are found at U=1.7$m/s$ and U=2.1$m/s$, which reflects the observations made for the in-line stress. Figure 5.4 (b) also illustrates the importance of predicting both the cross-flow and in-line response; the fatigue damage is of the same magnitude cross-flow and in-line.

In Figure 5.5 the spatial variability of the fatigue damage for three selected cases is shown. Both cross-flow and in-line the damage is predicted quite accurately for the two lowest speeds where the predictions are even aligned over a large part of the riser length. For U=2.3$m/s$ there is reasonably good agreement cross-flow, while the damage in-line is too low in the part of the riser with low current speed. These plots reveal something the plot in Figure 5.4 did not; the maximum fatigue prediction looks relatively good, but over the length of the riser the fatigue prediction is not so accurate. Travelling waves are clearly influencing the response both cross-flow and in-line for higher current speeds, especially in the high speed part of the riser. This applies for both the experiments and the simulations, but the point of maximum fatigue damage cross-flow is not predicted accurately as it is found close to the mid-span, while in the experiments it is seen closer towards the end with maximum current speed.

In order to confirm that also the displacements are predicted with acceptable accuracy, the mean of the cross-flow and in-line displacement standard deviation are presented in Figure 5.6. Too high predictions are seen for low speeds cross-flow, but apart from that the magnitude of the displacement response is predicted well both cross-flow and in-line.

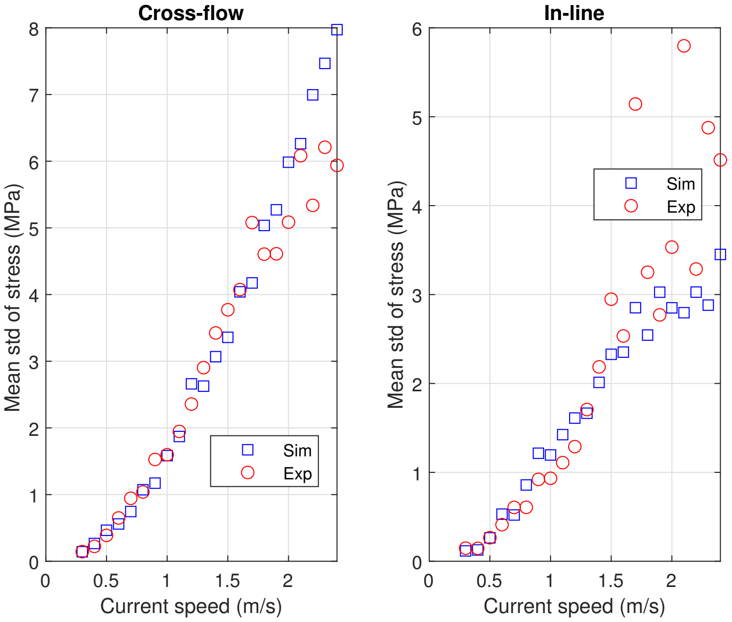

(a) Mean of stress standard deviation along riser

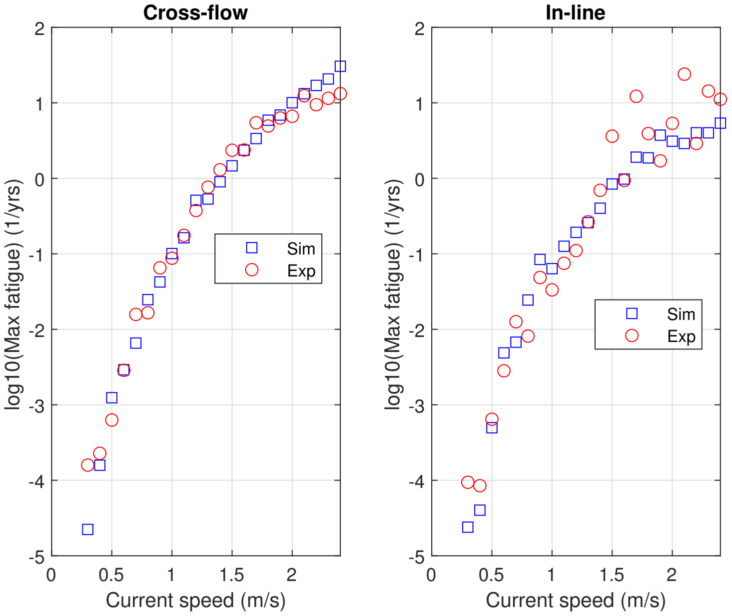

(b) Maximum fatigue along riser

Figure 5.4: Mean of stress std and maximum fatigue damage along bare riser in shear flow for current speeds 0.3-2.4$m/s$

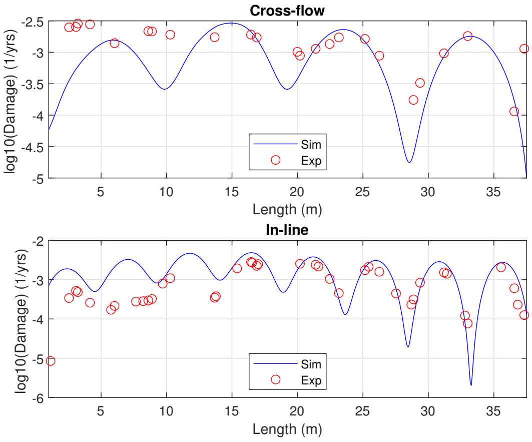

(a) Case 0S0.6

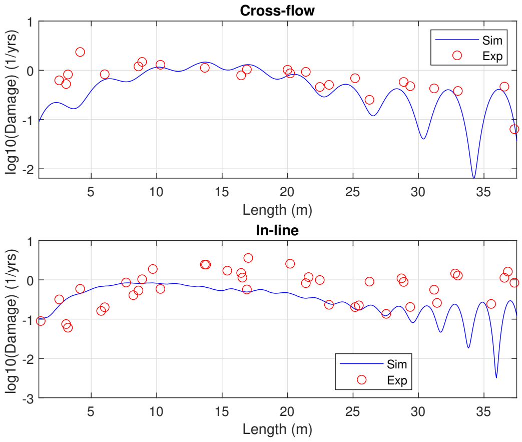

(b) Case 0S1.5

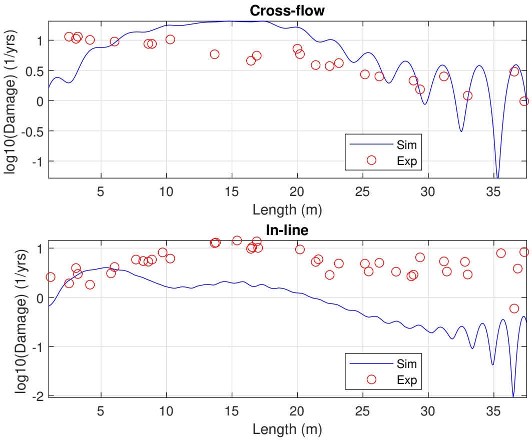

(c) Case 0S2.3

Figure 5.5: Annual fatigue damage along bare riser for three shear flow cases

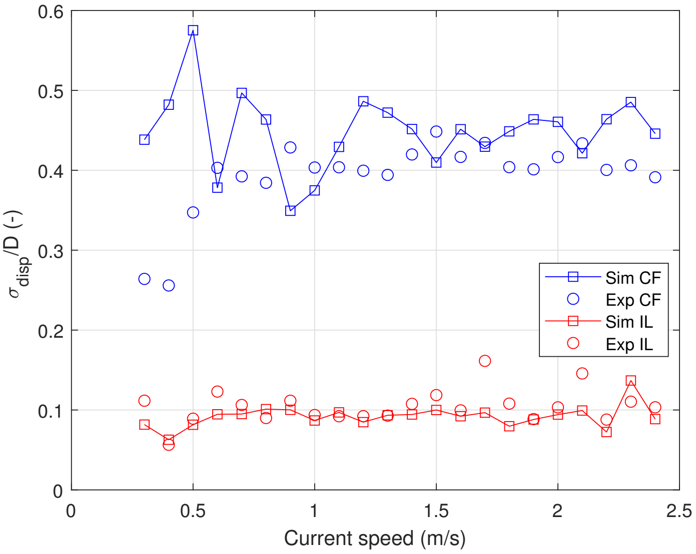

Figure 5.6: Mean of displacement standard deviation for bare pipe in shear flow. Normalized by diameter

### 5.1.2 Uniform flow

Figure 5.7 shows that the dominating frequencies are overestimated for speeds larger than $1.2m/s$ and well predicted for lower speeds both cross-flow and in-line. This indicates that $\hat{f}_0$ is slightly too large, but due to the close experimental agreement for dominating frequencies in shear flow and that too large dominating frequencies will contribute to conservative fatigue predictions, and not the opposite, it was decided not to alter the synchronization range parameters.

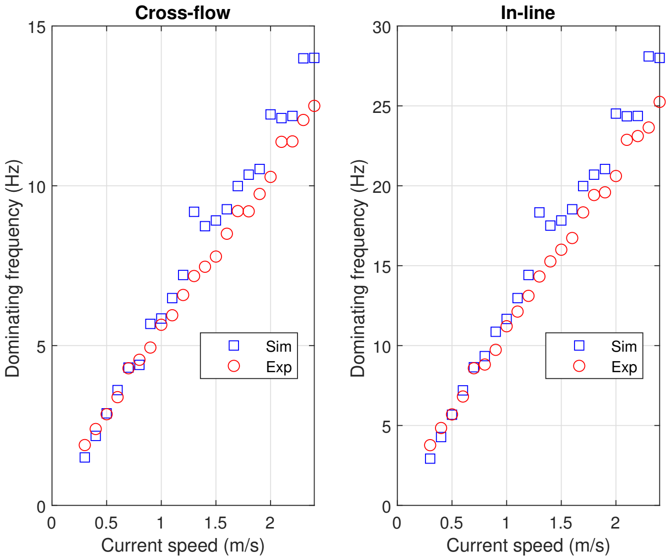

Figure 5.7: Dominating frequencies for bare pipe in uniform flow for current speeds 0.3-2.4$m/s$

The mean value of cross-flow and in-line stress standard deviation are plotted in Figure 5.8 (a). For current speeds lower than $1m/s$ reasonably good predictions are observed both cross-flow and in-line, but for higher current speeds the predictions cross-flow are increasingly overestimated. In-line the predictions at higher current speeds are in general conservative, but somehow unstable; the response variation between adjacent current speeds is large. In Figure 5.8 (b) the maximum annual fatigue damage cross-flow and in-line along the riser are shown. With the dominating frequencies predicted too large and a general trend of overestimated stresses, the maximum fatigue predictions are as expected larger than the experimental results. Also it should be noted that in some of the cases (e.g. U=$1.6m/s$) where the in-line mean stress predictions are too low the maximum fatigue damage is predicted conservatively, probably due to a combination of the overestimated dominating frequency and that the maximum stress is predicted with higher accuracy than the mean stress.

Figure 5.9 shows the axial distribution of fatigue damage for three selected cases. The magnitude of the fatigue damage is predicted very well for the lowest speed, but unlike for shear flow the predictions do not follow the measurements. For higher speeds the overestimation of cross-flow fatigue damage increases, which confirms the observation for maximum fatigue damage from Figure 5.8 (b). In-line there are observed large variations in the predicted fatigue damage along the riser which are not seen to the same extent for the measured results. During the calibration of the quadratic drag coefficient it was observed that these variations were increased as the quadratic drag coefficient was decreased.

As a measure of the vibration amplitude the mean of the cross-flow and in-line displacement standard deviation, normalized by diameter, are briefly considered. Figure 5.10 shows the same general trend that was observed for stresses; the cross-flow response is too high. In-line the trend is that the response magnitude is slightly too low.

Compared to the shear flow cases the experimental agreement is clearly not equally satisfactory. In Section 3.6 it was stated that the calibration was done based on obtaining good predictions for the shear flow cases and at least acceptable results for the uniform flow cases. From an engineering point of view it can be stated that conservative results are acceptable results, and the results in uniform flow are (partly) justified by this argument. Anyway it would be interesting in the future to apply an optimization algorithm in order to determine the hydrodynamic coefficients that give the best fit to experimental data in both shear and uniform flow.

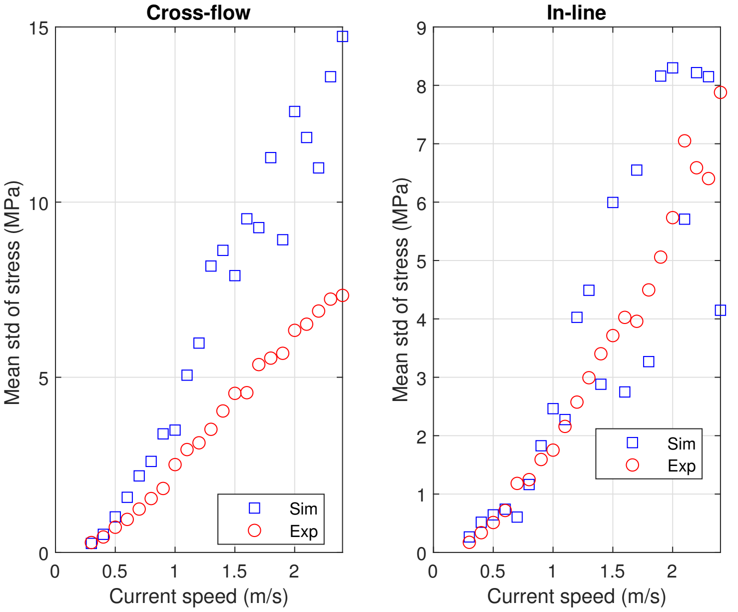

(a) Mean of stress standard deviation along riser

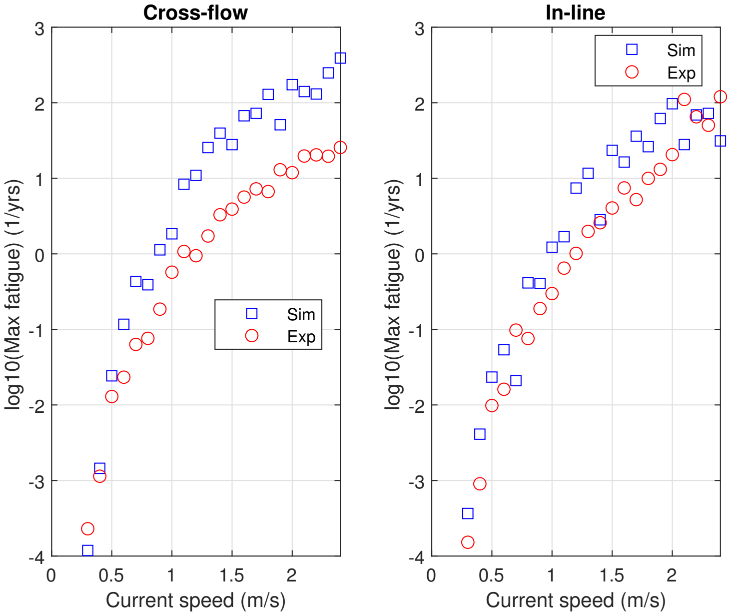

(b) Maximum fatigue along riser

Figure 5.8: Mean of stress std and maximum fatigue damage along bare riser in uniform flow for current speeds 0.3-2.4$m/s$

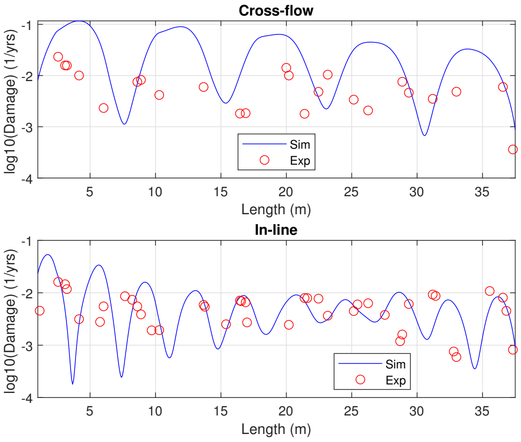

(a) Case 0U0.6

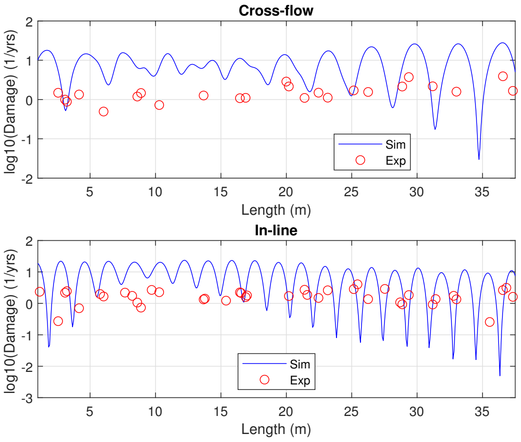

(b) Case 0U1.5

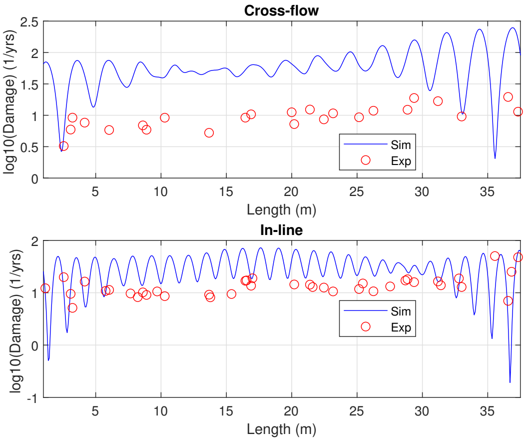

(c) Case 0U2.3

Figure 5.9: Annual fatigue damage along bare riser for three uniform flow cases

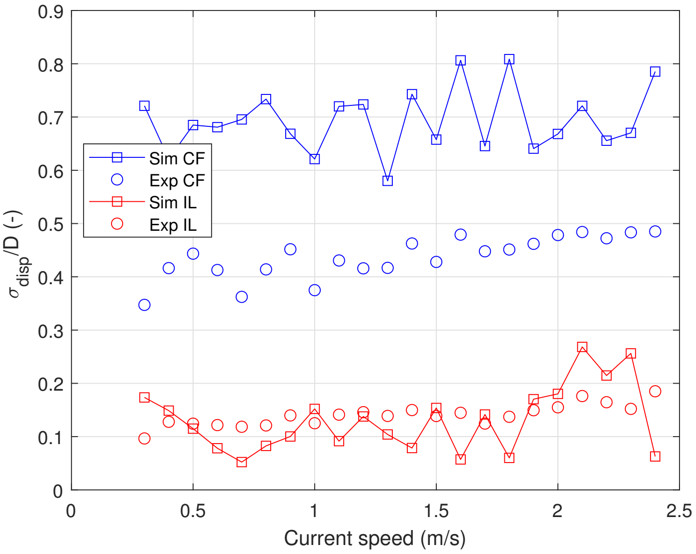

Figure 5.10: Mean of displacement standard deviation for bare pipe in uniform flow. Normalized by diameter

### 5.1.3 Fatigue safety factors

It was observed that the predictions of maximum fatigue damage for most cases both in shear and uniform flow were conservative. Some predictions were however non-conservative, and hence the maximum and median safety factor introduced in Section 3.5.6 are presented in Table 5.2 to illustrate the need of safety factors. The predictions were not equally good in shear and uniform flow, neither cross-flow and in-line, and to distinguish the simulations into four simulation sets is hence natural.

Table 5.2: Maximum fatigue damage safety factors
Conservative for all ($\eta_{max}$) and 50% ($\eta_{med}$) of the cases

| | **Shear flow** | | **Uniform flow** | |
|---|---|---|---|---|
| | Cross-flow | In-line | Cross-flow | In-line |
| $\eta_{max}$ | 7.14 | 8.26 | 1.94 | 4.65 |
| $\eta_{med}$ | 0.96 | 1.48 | 0.14 | 0.38 |

The general trend of conservative results is reflected well in the median safety factor which on average is below 1. Also the difference in the quality of the predictions between shear flow and uniform flow cases is seen in the median safety factor: shear flow is considerably more accurate as the safety factors are 0.96 and 1.48. The maximum safety factor represents the worst prediction with respect to conservatism. Lower values are found for the uniform flow cases than for the shear flow cases, which is not surprising as the fatigue damage in general was predicted too large in uniform flow. For shear flow the most non-conservative cross-flow prediction was the case with U=0.3$m/s$ as seen from Figure 5.4. Closer inspection of this case shows that the measurement closest to the low speed end of the riser is almost a factor 10 larger than the other measurements. The reliability of this measurement is hence questionable, and ignoring it yields an accurate prediction of the maximum fatigue damage. Consequently the required maximum safety factor will be reduced to 2.39. A safety factor of 8.26 was required in-line for the shear flow case with U=2.1$m/s$, which is a result of the previously discussed large measured in-line stress seen in Figure 5.4 (a). In further work it should be investigated why the in-line stress at some uniform current speeds is underestimated when the general trend is too large predictions. As well it is of concern that very good results are predicted for the shear flow cases, while the same model provides too conservative results in uniform flow, especially cross-flow. This indicates that different model parameters are required in shear and uniform flow, which reduces the robustness of the model.

## 5.2 41% and 62% strake coverage

With the confirmation that the VIV response is predicted with acceptable accuracy (or at least conservatively) for bare pipes, the combined load model for bare and straked sections was applied. Note that a presentation of safety factors will not be given here as the predictions in general are accurate or conservative, except in some cases with low current speeds associated with very low maximum fatigue damage.

### 5.2.1 Shear flow

Dominating frequency is plotted as a function of current speed in Figure 5.11 for 41% strake coverage. First, observe the effect of strakes on dominating frequencies both cross-flow and in-line in both simulations and experiments; they are reduced significantly compared to their magnitude in the bare pipe cases. On average they are reduced by a factor 0.39/0.50 cross-flow and 0.38/0.42 in-line in the simulations/experiments. This was expected considering the fact that the maximum current speed acting on the bare pipe section was reduced by a factor 2 due to the strakes presence in the upper half of the riser (not considering the effect the static displacement has on the effective current speed along the riser). Note that the dominating frequencies for the 62% strake coverage cases are not presented. This is due to the large influence the strakes have in these experiments with respect to responding frequencies: the spectra are seen to be broad-banded even in the bare section, which leads to an almost random choice of dominating frequency within this band. It was hence found that a comparison of the dominating frequencies in the simulations and the experiments is rather confusing. Anyway, a similar reduction of the frequencies governing the response for the 62% strake coverage cases were seen in both the simulations and the experiments. Also, recall the issues related to filtering of the cases with 62% strake coverage presented in Section 3.7.3 which introduces an uncertainty which must be kept in mind when evaluating stress, displacement and fatigue in this section.

Moving on, the jumps in cross-flow dominating frequency that were seen for the bare pipe are also seen for 41% strake coverage. There are however fewer jumps due to the fact that increasing the maximum speed along the riser with $0.1 m/s$ only increases the maximum speed in the bare section with $0.05 m/s$. Consequently the same mode, with associated dominating frequency, dominates for a large range of current speeds, since the shedding frequency is not altered much, until the current speed reaches a level where the next mode dominates. As for the bare pipe cases it is not captured exactly at which current speed the jump in dominating frequency occurs: the model predicts the jump $0.3 m/s$ "too late" here, which is $0.15 m/s$ when considering the current speed on the bare section, while the jump was predicted $0.1 m/s$ "too late" or "too soon" for the bare pipe. Taking into account that the prediction is in good agreement with the measurement when the jump is made, this is acceptable. In-line the agreement is reasonably good at low speeds, while the quality of the predictions is lower when increasing the speed.

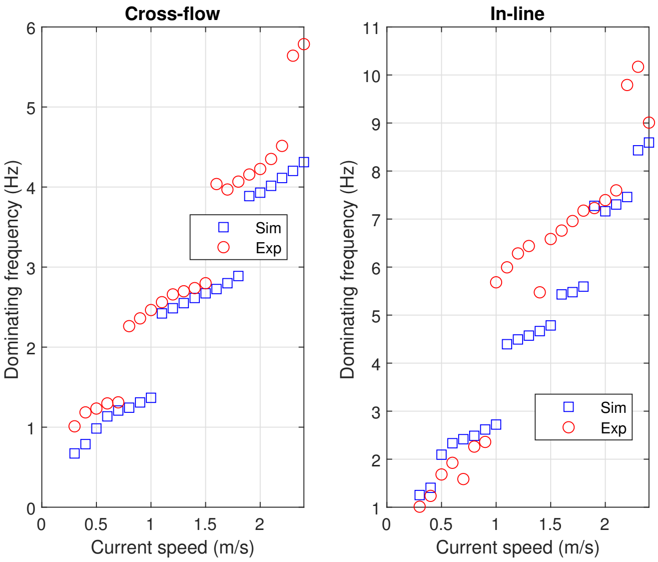

Figure 5.11: Dominating frequencies for pipe with strakes in shear flow for current speeds 0.3-2.4$m/s$

In Figure 5.12 the mean value of the simulated stress standard deviation is plotted as a function of the current speed both cross-flow and in-line and compared to experiments. First observe that the order of magnitude of the stresses is significantly smaller with 41% strake coverage than for the bare pipe case (see Figure 5.4) and further reduced with 62% strake coverage, which shows that strakes effectively reduce the response. Cross-flow the predictions and the measurements compare quite well for the 41% strake configuration. However, underestimates are seen at U=1.6-1.8$m/s$ and these are probably connected to the late predicted change of mode (seen from dominating frequency plot). In-line the stress response is on the other hand predicted too large for all speeds except the smallest. The predictions cross-flow for the 62% strake configuration are in general slightly too high, while in-line they are significantly larger than the measurements.

Moving on to the maximum fatigue damage along the riser, see Figure 5.13, more or less the same observations as for the stress are made. Cross-flow the average ratio between the predictions and the measurements, $\bar{R}_D$, is 1.01 with 41% suppression coverage, which indicates very accurate results, while $\bar{R}_D = 2.72$ with 62% coverage. In-line the predictions are very conservative for most speeds with 41% strake coverage, which reflects the too high stress predictions. For the 62% strake coverage cases the predictions do not compare well with the experiments, but at least these cases are associated with extremely low fatigue damage also in the experiments: on average the riser will survive more than 100 000 years. It is not of major relevance to have a model that can predict such small responses, and also taking into account the uncertainties related to treating the experimental data this is accepted. The rather large conservatism observed in-line for the 41% strakes coverage cases is more disappointing considering the good agreement cross-flow and the good results in shear flow with bare pipe. It seems that a different damping formulation is required in-line than cross-flow, as the damping seems to be too small in-line.

To assess the performance of the model more in detail the fatigue damage along the riser for three current speeds is shown in Figure 5.14. It is observed that both the predicted and measured fatigue damage is largest towards the bare (low-speed) end of the riser for higher speeds with 41% strake coverage. The model predicts a similar behaviour when the strake coverage is increased to 62%, but the experimental fatigue damage is largest in the straked end and is reduced as the speed becomes lower towards the bare section. With higher percentage coverage than about 75% it has from model tests been observed that the straked section controls the VIV behaviour, and a different physical behaviour is observed than for the cases where the bare section governs the response [7]. Recall that 62% coverage represents 75% coverage with 13% loss of coverage due to instrumentation gaps, which is on the limit of where the straked section from experience starts to dominate. This is the most likely explanation for the different behaviour in the predictions and the measurements: the predictions are not able to capture the changed physical behaviour observed in the experiments with 62% coverage, hence the similar trend as with 41% coverage. The frequency domain prediction tool VIVANA is actually limited to handle cases up to 75% coverage [7], which underlines that too high strake coverage is problematic to deal with.

In order to have an impression of how strakes affect the displacement response amplitude the average displacement standard deviation along the riser is plotted as a function of the current speed in Figure 5.15. For all current speeds the predictions are conservative for the 41% coverage cases. Since the displacement predictions with bare pipe in shear flow were quite accurate, this underlines the importance of investigating the energy dissipation from the straked section when assessing the model. When the coverage is increased to 62% the response becomes extremely small and supports that the model performance in shear flow with high percentage strake coverage is not of significant practical interest.

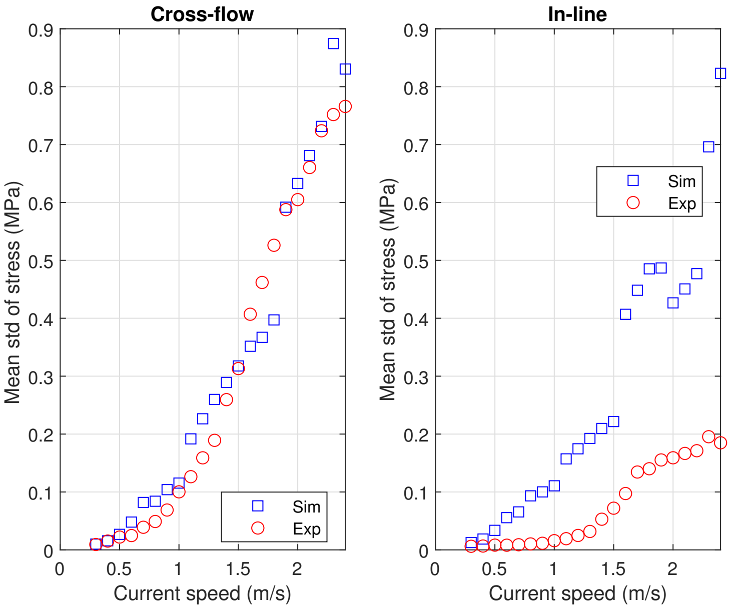

(a) 41% strake coverage

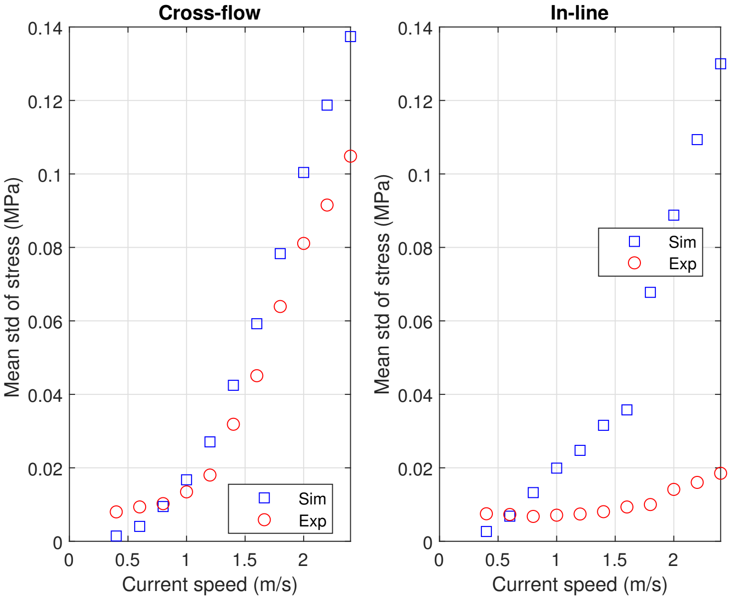

(b) 62% strake coverage

Figure 5.12: Mean of stress std along straked riser in shear flow for current speeds 0.3-2.4$m/s$

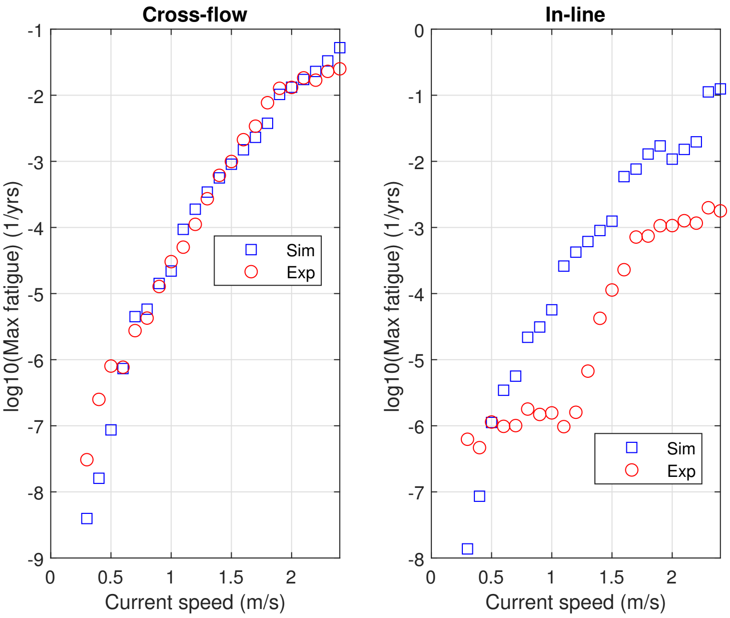

(a) 41% strake coverage

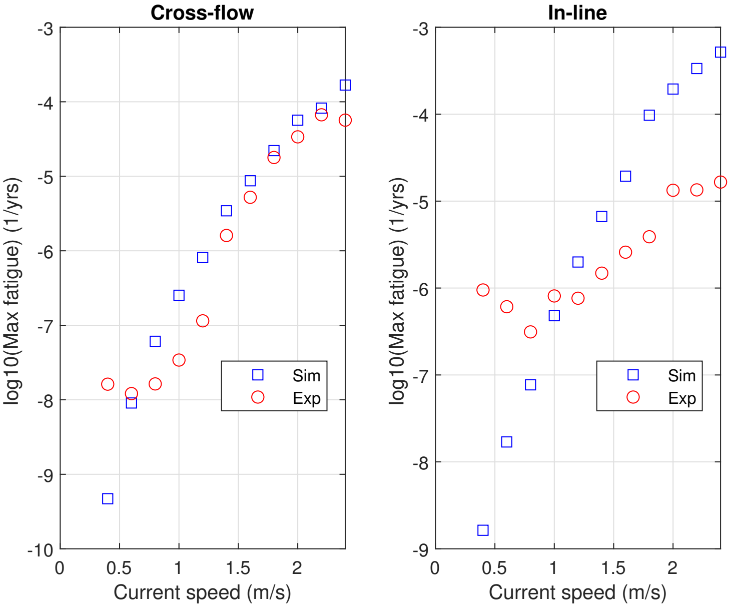

(b) 62% strake coverage

Figure 5.13: Maximum fatigue damage along straked riser in shear flow for current speeds 0.3-2.4$m/s$

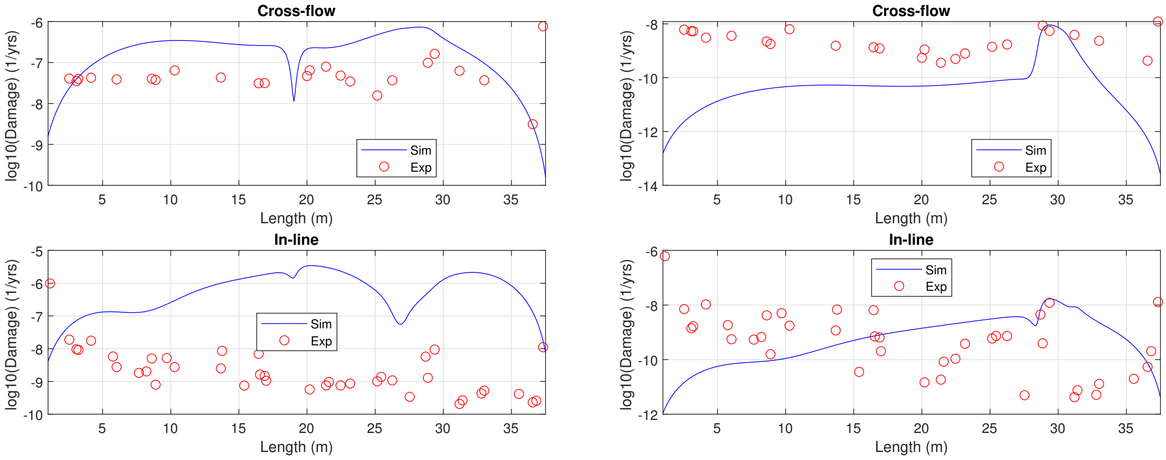

(a) Case 41S0.6 (b) Case 62S0.6

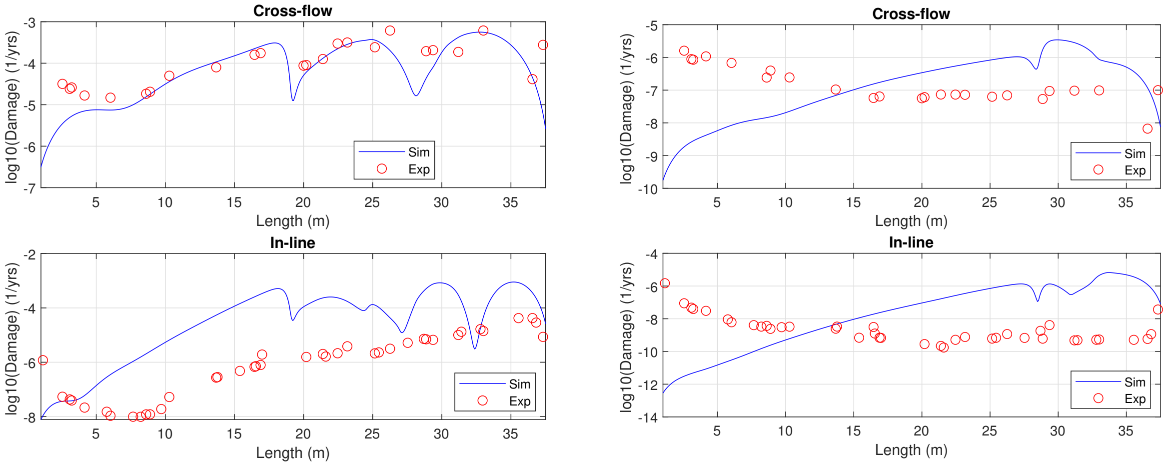

(c) Case 41S1.4 (d) Case 62S1.4

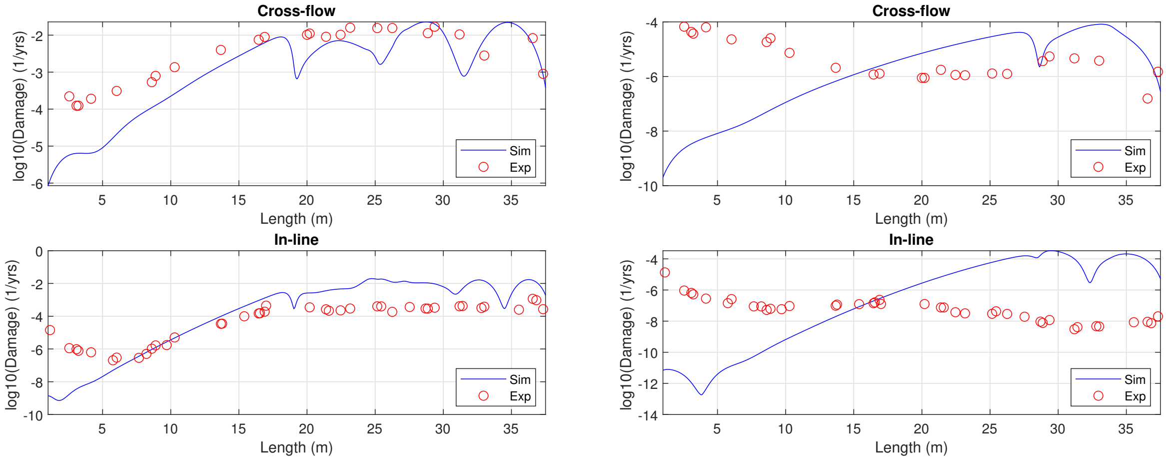

(e) Case 41S2.2 (f) Case 62S2.2

Figure 5.14: Annual fatigue damage along straked riser for three shear flow speed cases

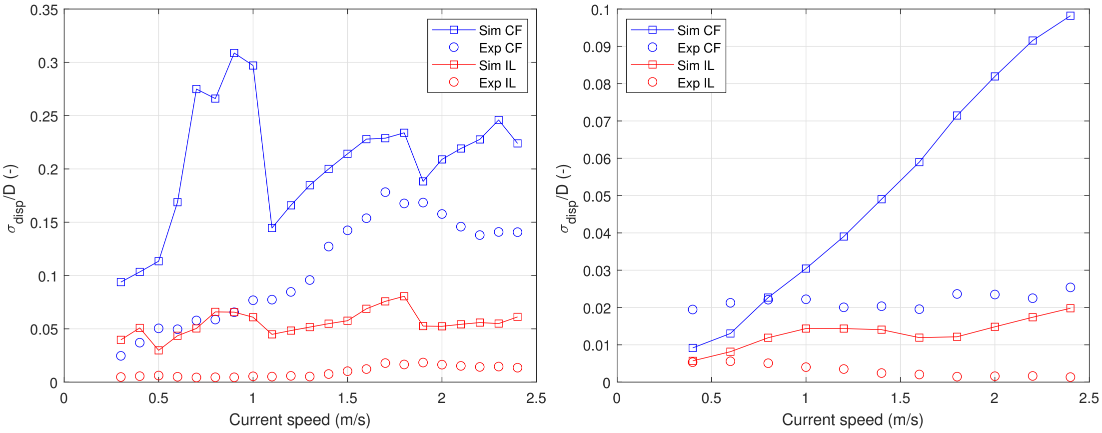

(a) 41% strake coverage

(b) 62% strake coverage

Figure 5.15: Mean of displacement standard deviation along straked riser in shear flow. Normalized by diameter

### 5.2.2 Uniform flow

Dominating frequency is plotted as a function of the current speed for the two strake configurations in Figure 5.11. As for the bare riser cases, a more or less linear trend for the dominating frequency is observed for both the configurations cross-flow and in-line. In opposition to the shear flow cases the dominating frequencies are of about the same order of magnitude as for the bare pipe cases, which is expected as the current speed in the bare section remains the same (again ignoring the effect of larger static displacement caused by the increased drag of the straked section). Observe that there is one clear exception for this with the 41% strake configuration in the measurements at U=2.4$m/s$. This is due to energy transfer from cross-flow to in-line, causing a in-line frequency component at the fundamental cross-flow frequency $\omega$ which dominates the response at $2\omega$ at the position of maximum stress response.

Moving on, the agreement between the predictions and the measurements is reasonably good. A tendency of predicting the dominating frequency slightly too low for speeds below $2m/s$ is observed for the 41% strake coverage cases, while over-predictions are observed above $2m/s$. It should be noted that both the predictions and measurements display response variability at higher speeds. This results in broad-banded spectra, which the method used for determining the dominating frequency is vulnerable to, but the plots show that the model at least predicts the dominating frequency in the correct range. Increasing the strake coverage to 62% results in more or less the same prediction quality, where the dominating frequencies are predicted too low at the highest current speeds.

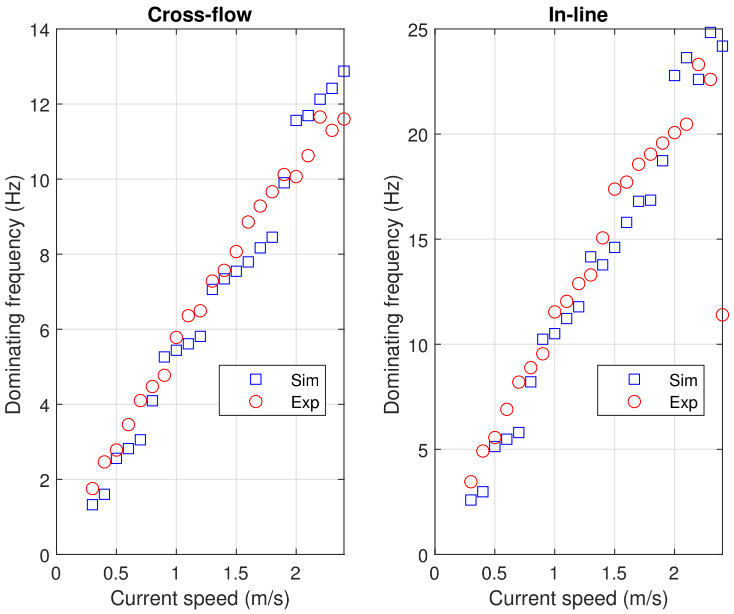

(a) 41% strake coverage

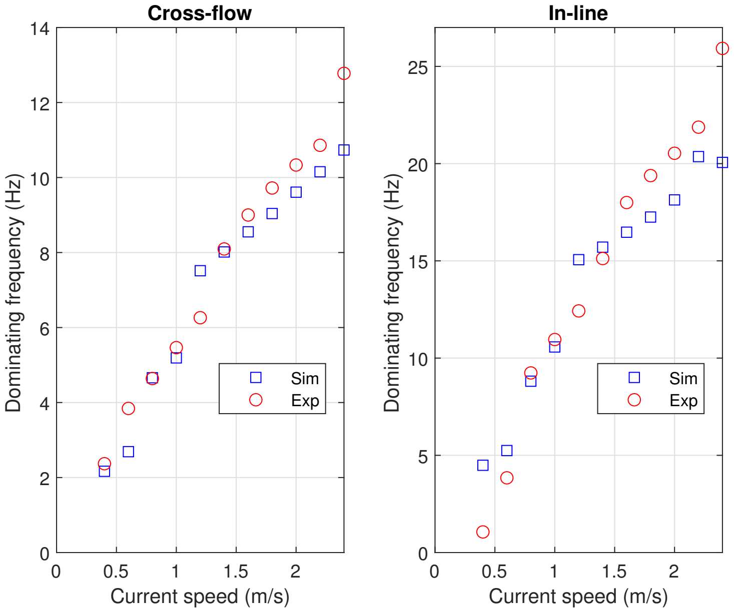

(b) 62% strake coverage

Figure 5.16: Dominating frequencies for pipe with strakes in uniform flow for current speeds 0.3-2.4$m/s$

The predictions of cross-flow stress standard deviations are seen to be very accurate for both the strake configurations, see Figure 5.17. Recall that the stress was predicted very conservatively for the bare pipe cases, hence the high quality of these results are somewhat surprising. This might have to do with the fact that when introducing strakes the bare section where the vortex shedding excitation takes place becomes much smaller and consequently the vortices that are shed off (ideally) with same phase along the riser become fewer. This reduces the global vortex-induced forces, the response is reduced and the model seems to be better suited for the straked than the bare configuration. In-line a general tendency of too large predictions is seen for both the strake configurations, where the predictions are more accurate with 41% coverage than with 62% coverage.

A comparison of the predicted and measured maximum fatigue damage along the riser as a function of the current speeds is presented in Figure 5.18. First, observe that the fatigue damage has not been reduced as much from the bare pipe cases as in the shear flow cases, even though the mean stress level is reduced. This is due to the oscillation frequency remains more or less the same as in the bare pipe cases, at least in the bare section where the maximum fatigue damage is found. This basically shows that in uniform flow a very high percentage strake coverage is needed in order to increase the fatigue life significantly. With 41% coverage the cross-flow predictions are very accurate for most speeds, but at the largest and smallest speeds the predictions are non-conservative. At the largest speeds, U=2.1-2.3$m/s$, there is one sensor measuring a significantly larger cross-flow fatigue damage than the other sensors which causes the apparent low prediction. This is illustrated in Figure 5.19 (e), where it is observed that the overall level of fatigue damage is predicted well, except at this sensor. The low maximum fatigue estimate at lower speeds, U=0.3-0.4$m/s$, can on the other hand not be justified by a similar argumentation as the predictions in general are smaller than the measurements over the riser length. These under-predictions are obviously not desirable, but are accepted due to the low magnitude of the damage at these speeds. Observe that also in-line the results are good with 41% coverage, with a slight tendency of over-prediction. With 62% coverage the predictions and measurements compare well cross-flow and are over-estimated in-line.

For assessing the model predictions more thoroughly the fatigue damage along the riser length for 3 current speeds are plotted and shown in Figure 5.19. The general impression is that the results are very accurate, especially for high speeds, which supports the good results observed for maximum fatigue damage. Much better spatial agreement is observed both cross-flow and in-line than in shear flow, where it was reflected on introducing a different damping formulation in-line than cross-flow. The results in uniform flow do not suggest this, however a suggestion for future work is to consider the energy transfer between the strakes-section and the fluid in order to assess if this is required.

The quality of the predicted amplitude of vibration is again represented by the mean value of the displacement standard deviation along the riser, see Figure 5.20. Very good agreement between predictions and measurements is observed in-line for both strake configurations, while cross-flow the predictions are slightly too high with 41% coverage (on average about $0.07D$‘=1.9$mm$ larger than the measurements) and not perfectly accurate, but realistic, with 62% coverage.

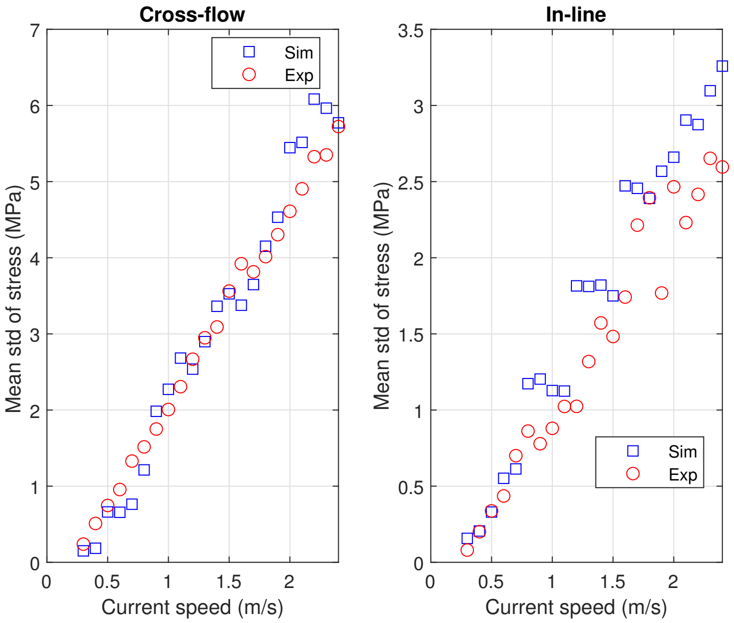

(a) 41% strake coverage

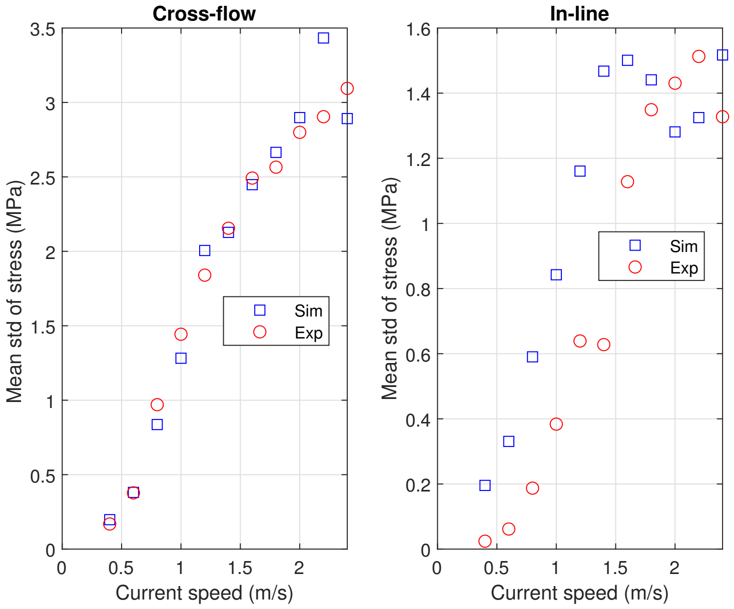

(b) 62% strake coverage

Figure 5.17: Mean of stress std along straked riser in uniform flow for current speeds 0.3-2.4$m/s$

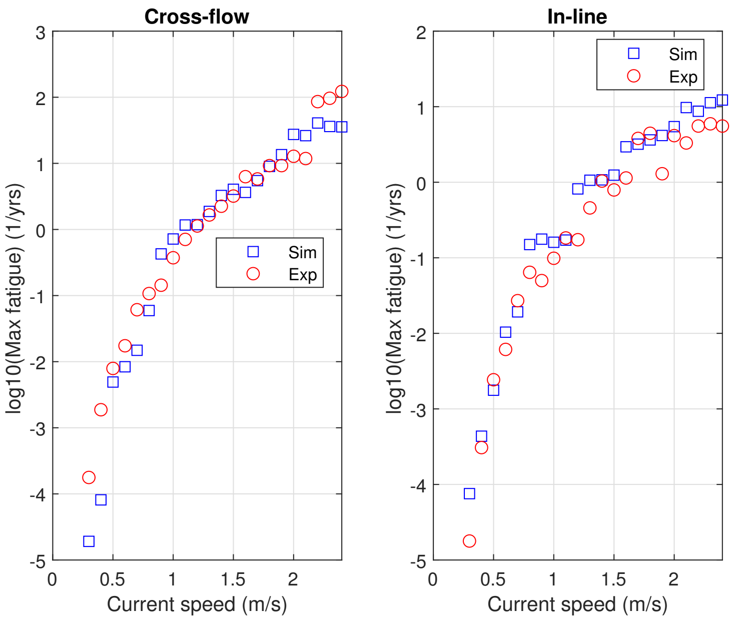

(a) 41% strake coverage

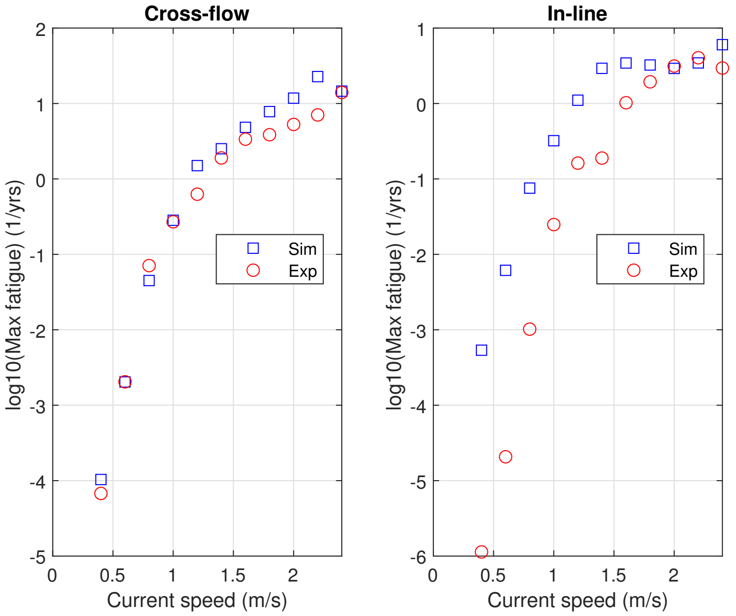

(b) 62% strake coverage

Figure 5.18: Maximum fatigue damage along straked riser in uniform flow for current speeds 0.3-2.4$m/s$

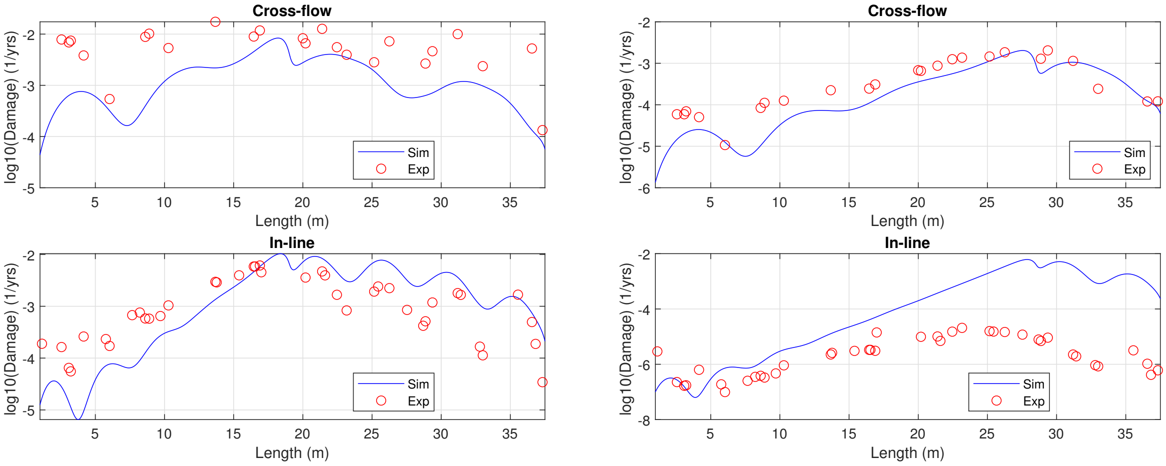

(a) Case 41U0.6 (b) Case 62U0.6

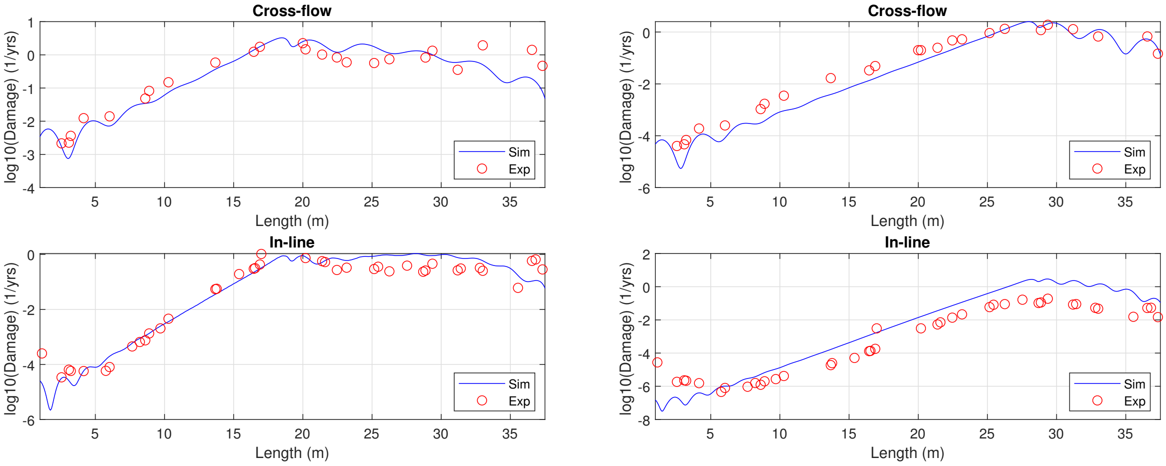

(c) Case 41U1.4 (d) Case 62U1.4

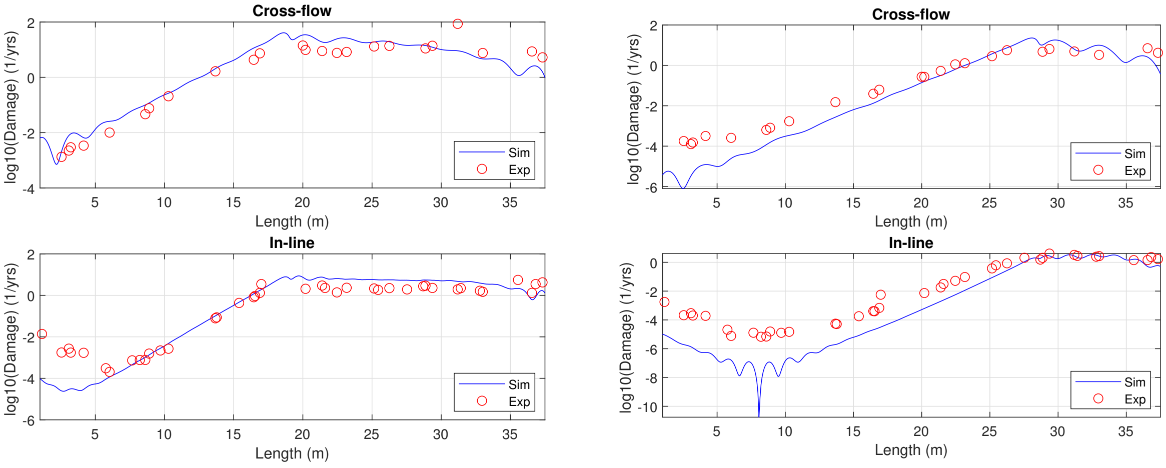

(e) Case 41U2.2 (f) Case 62U2.2

Figure 5.19: Fatigue damage along straked riser for three uniform flow speed cases

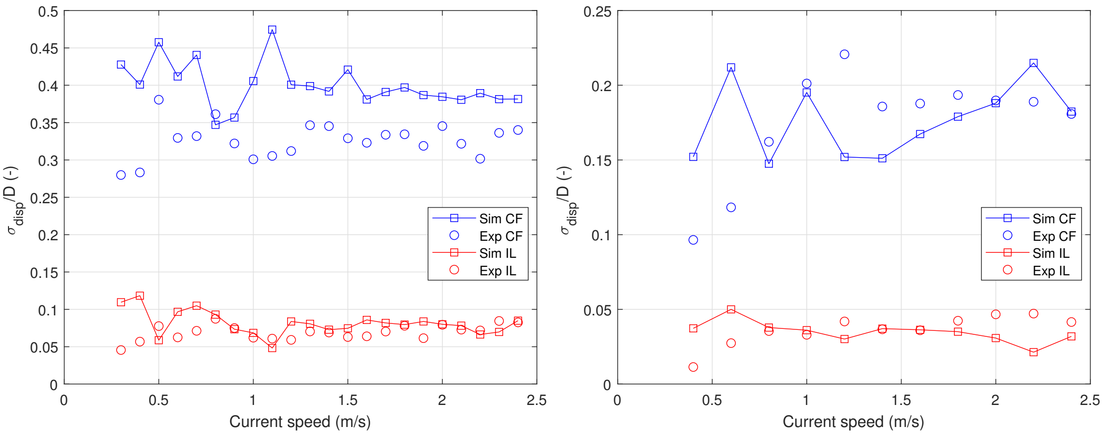

(a) 41% strake coverage

(b) 62% strake coverage

Figure 5.20: Mean of displacement standard deviation along straked riser in uniform flow. Normalized by diameter

## 5.3 Summary of results

The results with respect to maximum fatigue damage along the riser for all the cases considered are given in Figure 5.21, and the parameters that define the hydrodynamic model used for obtaining these results are found in Table 5.3 and 5.4. Note that the parameters for the straked section are dimensionless and must be converted to the input format required by Riflex as explained in Section 3.2.3.

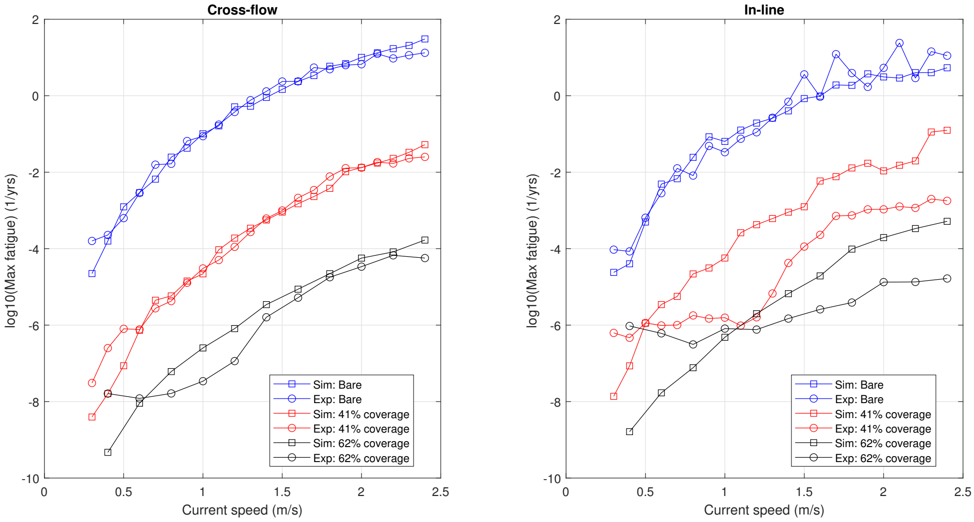

(a) Shear flow

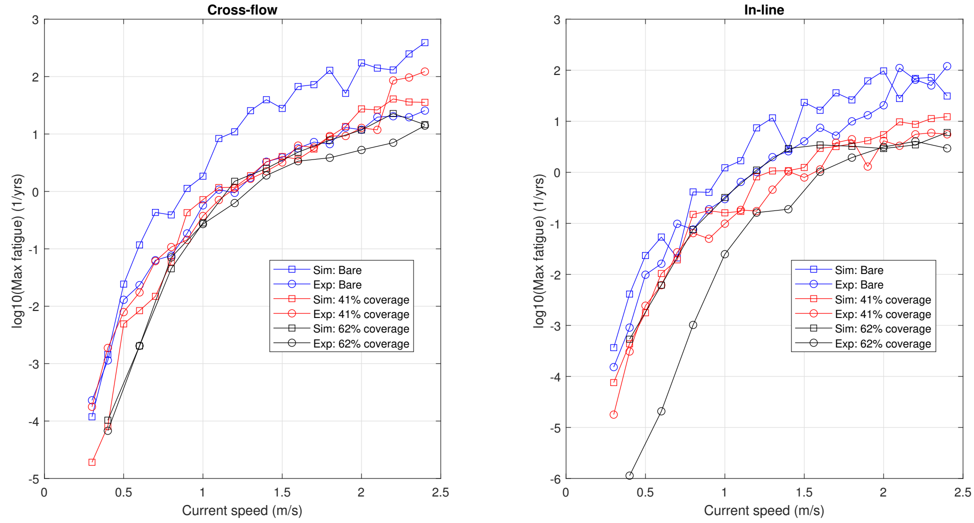

(b) Uniform flow

Figure 5.21: Maximum fatigue damage along riser for all considered cases

Table 5.3: Final model: Hydrodynamic coefficients for bare riser section

| **Parameter** | **Magnitude** |
|---|---|
| Quadratic drag coefficient in normal direction [-] | 0.9 |
| Added mass per unit length in normal direction [-] | 1 |
| $C_{v,y}$ [-] | 0.85 |
| $C_{v,x}$ [-] | 0.98 |
| $\hat{f}_0$ [-] | 0.144 |
| $\hat{f}_{min}$ [-] | 0.08 |
| $\hat{f}_{max}$ [-] | 0.208 |
| $\alpha$ [-] | 0.15 |
| $C_{hh}$ [-] | 0 |

Table 5.4: Final model: Hydrodynamic coefficients for straked riser section

| **Parameter** | **Magnitude** |
|---|---|
| Non-dimensional quadratic drag coefficient for local x-direction [-] | 0.0383 |
| Non-dimensional quadratic drag coefficient for local y-direction [-] | 1.4513 |
| Non-dimensional quadratic drag coefficient for local z-direction [-] | 1.4513 |
| Non-dimensional added mass in local x-direction [-] | 0.0021 |
| Non-dimensional added mass in local y-direction [-] | 1.5078 |
| Non-dimensional added mass in local z-direction [-] | 1.5078 |

# Chapter 6

# Conclusions and further work

## 6.1 Conclusions

The main purpose of this thesis was to establish a hydrodynamic load model, defined by a single set of parameters, which in combination with a structural and numerical model is able predict the VIV response of both bare and partially straked risers in uniform and shear flow. An analytical hydrodynamic load model concept for straked sections has been adopted. When applied with the TD VIV model for bare sections, predictions of the response for partially straked risers are feasible.

Simulations of selected cases from the NDP model tests [8] have been performed and showed that the model is capable of reproducing the fundamental VIV response very accurately for a large number of cases with both bare and partially straked risers. In general the model produces conservative results when it fails to make accurate predictions, however there is in some cases observed non-conservative predictions when the riser is exposed to low current speeds. The associated fatigue damage was in these cases very small and will not be governing the design of a real marine riser, so the under-predictions were accepted.

In particular the results with 41% strake coverage were satisfying, which demonstrated clearly that the proposed model for strakes is promising. Also with 62% strake coverage the results were relatively good in uniform flow, while some uncertainties were related to the processing of the model test data in shear flow, which somewhat reduced the significance of these results. It is known from model tests that with too large strake coverage the straked section governs the VIV behaviour, which causes the physical behaviour to be different than when the bare section controls the response. The experimental cases with 62% strake coverage in shear flow seems to display such behaviour, which the model is not able to predict. This indicates that the model has a upper limit for the percentage strake coverage it can handle, which is expected considering the simplicity of the hydrodynamic load model formulation for strakes. As the model is given by Morison's equation, without any VIV excitation terms, no VIV induced forces can origin from the straked part. In reality vortices are shed off from the tip of the strakes, and there is always some VIV excitation in the straked part. Due to the low correlation of the vortex shedding along the straked part the excitation is however insignificant compared to the VIV excitation from the bare section, unless a large part of the pipe is covered with strakes. Anyway, it is of little interest to include such a feature to the model since strakes usually become very effective as suppression device in the cases where the bare section no longer controls the VIV behaviour.

The hydrodynamic load model for bare riser sections already required eight empirical inputs (in [3]) and it was desired to avoid making the hydrodynamic load model for strakes too complicated, e.g. by introducing more parameters that require tuning. Only analytical parameters depending on the strakes geometry were introduced, which made sure the increase of complexity was minimal.

At last some significant observations regarding the TD VIV model, but not directly related to the scope of work, were detected during the thesis work. These features have not been documented previously, but may cause some confusion when they are encountered and are hence mentioned here. First, a significant slowly varying in-line displacement response component was discovered which caused unphysical response. Several attempts were made in order to remove it, without success, and as it was not of importance for the stress response or fatigue it was filtered out from the simulation data. Second, different steady-state solutions with different element mesh sizes were obtained in some cases, i.e. standard mesh element convergence could not be achieved. This is related to the non-linearity of the load model formulation, but does not reduce the integrity of the model.

## 6.2 Further work

In this thesis the riser was modelled as a pinned-pinned beam with constant tension, while in the experiments some tension variations were observed. A potential improvement is hence to model the boundary conditions more exact in order to capture the dynamic behaviour, i.e. to model the heave compensator at one end of the riser and better include the tension variations in the riser. This model is illustrated in Figure 6.1, where the beam segment of length $L$ represents the riser and the beam segment with length $l$ represents the heave compensator by an axial spring with stiffness $k = (EA)_s/l$. The two beam segments are connected by a joint. Note that the axial stiffness $EA_s$ of the latter beam segment does not have to correspond to the axial stiffness of the riser, but must be chosen so that $k = \frac{(EA)_s}{l}$ is equal to the stiffness of the heave compensator $9333N/m$. The beam segment with length $l$ must be given a very large bending stiffness $(EI)_s$ so that the right end of the riser is not allowed to move out of the plane or vertically in the plane. The constant tension $T$ should be changed from case to case in order to make sure that the total tension in static condition is equal to the mean tension measured at the riser ends. It should be mentioned that in the selected NDP experiments the tension variations were seen to be much smaller than the mean tension level (never more than about 5%), so it can be questioned how large the effect of including the tension variation will be. An uncertainty will however be removed, and it is hence worth investigating.

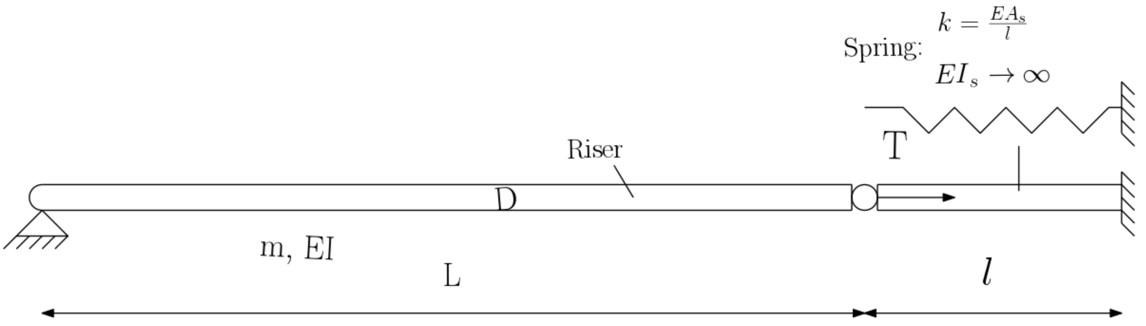

Figure 6.1: Alternative modelling of the NDP test riser

As was discussed by Thorsen [2] and Ulveseter [3] a method for determining the empirical parameters of the TD VIV model needs to be established in order for the model to be applied as an engineering tool. The complexity of finding parameters that provide good results for all cases was experienced in this study, and here only the NDP experiments were considered. It is needed to investigate if the set of parameters found here are appropriate also for modelling of other experiments. Most likely the parameters would need to be scaled, and it needs to be investigated how the scaling should be done. Little work has been done so far with respect to scaling, but Thorsen [2] suggested that surface roughness, Reynolds number and KC-number might all be relevant quantities.

With respect to the empirical parameters obtained in this study it would be interesting to see if an optimization algorithm would provide the same set of parameters. Optimally all the hydrodynamic parameters should be optimized, but this might not be feasible. Based on the experience from this study the parameters that should be optimized are the cross-flow and in-line vortex shedding excitation coefficients ($C_{v,y}$ and $C_{v,x}$) and the quadratic drag coefficient ($C_D$). If possible the algorithm should take into account both the uniform and shear flow cases and for consistency focus on the mean stress standard deviation along the riser as was done in this study. If the same approach is applied to a large number of experiments the hydrodynamic parameters can be mapped based on their dependency of e.g. the Reynolds number and possibly empirical formulas can be established.

Higher harmonics are not considered in this thesis. Recalling that the fatigue damage from higher order vibrations in some cases exceeds the fundamental response (see Section 2.2) supports that they should be included in a VIV response analysis. The higher harmonic load coefficient ($C_{hh}$) used in the 4th paper by Ulveseter [3] is a natural choice as initial value. Taking into account that some of the empirical parameters in Ulveseter's paper are different from those used in this thesis it might be needed to calibrate $C_{hh}$.

The approach in this study was to model the straked section with Morison's equation and apply the hydrodynamic added mass and drag coefficients found from analytical formulations [33]. It has not been looked into how the energy dissipation from the modelled strakes and the experimental strakes correspond. Even though the results are seen to be reasonably good, this should be evaluated in further work for a more thorough investigation of the performance of the hydrodynamic load model for strakes. As well, all new models need to be benchmarked against several experimental investigations in order to verify the robustness or reveal the weaknesses of the model. The model developed in this thesis is no exception, and other model tests with risers fitted with strakes, e.g. the Shell High Mode VIV tests [15], should be looked into.

# Bibliography

[1] P.E. Voie, C.M. Larsen, J. Wu, and T. Resvanis. *VIV Best Practice: Guideline on analysis of vortex-induced vibrations in risers and umbilicals.* Det Norske Veritas AS, 2016.

[2] M.J. Thorsen. *Time Domain Analysis of Vortex-Induced Vibrations.* PhD thesis, 2016.

[3] J.V. Ulveseter. *Advances in semi-empirical time domain modelling of vortex-induced vibrations.* PhD thesis, 2018.

[4] M.J. Thorsen, S. Sævik, and C.M. Larsen. A simplified method for time domain simulation of cross-flow vortex-induced vibrations. *Journal of Fluids and Structures*, 49:135 – 148, 2014.

[5] M.J. Thorsen, S. Sævik, and C.M. Larsen. Time domain simulation of vortex-induced vibrations in stationary and oscillating flows. *Journal of Fluids and Structures*, 61:1 – 19, 2016.

[6] J.V. Ulveseter, M.J. Thorsen, S. Sævik, and C.M. Larsen. Time domain simulation of riser viv in current and irregular waves. *Marine Structures*, 60:241 – 260, 2018.

[7] SINTEF Ocean. *VIVANA 4.12.0 Theory Manual.* 2018.

[8] A.D. Trim, H. Braaten, H. Lie, and M.A. Tognarelli. Experimental investigation of vortex-induced vibration of long marine risers. *Journal of Fluids and Structures*, 21(3):335 – 361, 2005. Marine and Aeronautical Fluid-Structure Interactions.

[9] M. Greco. *Lecture Notes TMR4215: Sea Loads.* 2012.

[10] J.K. Vandiver K. Vikestad and C.M. Larsen. Added mass and oscillation frequency for a circular cylinder subjected to vortex-induced vibrations and external disturbance. *Journal of Fluids and Structures*, 14(7):1071 – 1088, 2000.

[11] O.M. Faltinsen. *Sea Loads on Ships and Offshore Structures.* Cambridge University Press, 1990.

[12] DNV GL. *Guidelines No. 14: Free Spanning Pipelines.* Det Norske Veritas AS, 1998.

[13] K.H. Aronsen. An experimental investigation of in-line and combined in-line and cross-flow vortex induced vibrations. *Ph.D. thesis*, December 2007.

[14] J. Wu, D. Yin, H. Lie, C.M. Larsen, R.J. Baarholm, V. Jhingran, and S.Liapis. On the occurrence of higher harmonics in the VIV response. *Proceedings of the ASME 2015 34th International Conference on Ocean, Offshore and Arctic Engineering*, June 2015.

[15] H. Lie, H. Braaten, V.G. Jhingran, O.E. Sequeiros, and K. Vandiver. Comprehensive riser VIV model tests in uniform and sheared flow. *Proceedings of the ASME 2012 31st International Conference on Ocean, Offshore and Arctic Engineering*, July 2012.

[16] E. Huse, G. Kleiven, and F.G. Nielsen. Large scale model testing of deep sea risers. *Offshore Technology Conference, OTC-8701-MS*, May 1998.

[17] J. Wu, D. Yin, H. Lie, C.M. Larsen, R.J. Baarholm, and S.Liapis. On the significance of the higher-order stress in riser vortex-induced vibrations responses. *Journal of Offshore Mechanics and Arctic Engineering*, 141, July 2017.

[18] M.A. Tognarelli, S.T. Slocum, W.R. Frank, and R.B. Campbell. VIV response of a long flexible cylinder in uniform and linearly sheared currents. *Offshore Technology Conference, OTC-16338-MS*, May 2004.

[19] G.S. Baarholm, C.M. Larsen, and H. Lie. On fatigue damage accumulation from in-line and cross-flow vortex-induced vibrations on risers. *Journal of Fluids and Structures*, 22(1):109 – 127, 2006.

[20] H. Lie and K.E. Kaasen. Modal analysis of measurements from a large-scale viv model test of a riser in linearly sheared flow. *Journal of Fluids and Structures*, 22(4):557 – 575, 2006.

[21] J.R. Chaplin, P.W. Bearman, F.J. Huera Huarte, and R.J. Pattenden. Laboratory measurements of vortex-induced vibrations of a vertical tension riser in a stepped current. *Journal of Fluids and Structures*, 21(1):3 – 24, 2005. Fluid-Structure and Flow-Acoustic Interactions involving Bluff Bodies.

[22] M.R. Dhanak and N.I.Xiros. *Springer Handbook of Ocean Engineering.* Springer, 2016.

[23] M.M. Zdravkovich. Review and classification of various aerodynamic and hydrodynamic means for suppressing vortex shedding. *Journal of Wind Engineering and Industrial Aerodynamics*, 7(2):145 – 189, 1981.

[24] H. Marcollo, A.E. Potts, D.R. Johnstone, P. Pezet, and P. Kurts. Drag reduction and VIV suppression behaviour of LGS technology integral to drilling riser buoyancy units. *Proceedings of the ASME 2016 35th International Conference on Ocean, Offshore and Arctic Engineering*, June 2016.

[25] M.L. Facchinetti, E. de Langre, and F. Biolley. Coupling of structure and wake oscillators in vortex-induced vibrations. *Journal of Fluids and Structures*, 19(2):123 – 140, 2004.

[26] R.H.M. Ogink and A.V. Metrikine. A wake oscillator with frequency dependent coupling for the modeling of vortex-induced vibration. *Journal of Sound and Vibration*, 329(26):5452 – 5473, 2010.

[27] P. Mainçon. A wiener-laguerre model of viv forces given recent cylinder velocities. *Mathematical Problems in Engineering*, vol. 2011:43 pages, 2011.

[28] M.J. Thorsen, S. Sævik, and C.M. Larsen. Fatigue damage from time domain simulation of combined in-line and cross-flow vortex-induced vibrations. *Marine Structures*, 41:200 – 222, 2015.

[29] M.J. Thorsen, S. Sævik, and C.M. Larsen. Non-linear time domain analysis of cross-flow vortex-induced vibrations. *Marine Structures*, 51:134 – 151, 2017.

[30] J.V. Ulveseter, S. Sævik, and C.M. Larsen. Time domain model for calculation of pure in-line vortex-induced vibrations. *Journal of Fluids and Structures*, 68:158 – 173, 2017.

[31] H.Braaten and H. Lie. NDP Riser High Mode VIV Tests Main Report. *Norwegian Deepwater Program: Riser and Mooring Project*, April 2005.

[32] DNV GL. *DNV-RP-C205: Environmental conditions and environmental loads.* Det Norske Veritas AS, 2010.

[33] A.Nestegård, P.E. Voie, and N. Sødahl. Hydrodynamic coefficients for straked risers. *ASME 2014 33rd International Conference on Ocean, Offshore and Arctic Engineering*, 6A: Pipeline and Riser Technology, 2014.

[34] I. Korkischko, J.R. Meneghini, R.S. Gioria, P.J. Jabardo, E. Casaprima, and R. Franciss. An experimental investigation of the flow around straked cylinders. *ASME 2007 26th International Conference on Offshore Mechanics and Arctic Engineering*, 3: Pipeline and Riser Technology; CFD and VIV, 2007.

[35] SINTEF Ocean. *RIFLEX 4.12.0 Theory Manual.* 2018.

[36] SINTEF Ocean. *RIFLEX 4.15.0 User Guide.* 2018.

[37] T. Sarpkaya. Force on a circular cylinder in viscous oscillatory flow at low keulegan—carpenter numbers. *Journal of Fluid Mechanics*, 165:61–71, 1986.

[38] H. Senga and C.M. Larsen. Forced motion experiments using cylinders with helical strakes. *Journal of Fluids and Structures*, 68:279 – 294, 2017.

[39] Y.W. Cheng and J.J. Broz. *Cycle counting methods for fatigue analysis with random load histories: a Fortran user's guide.* National Bureau of Standards U.S. Department of Commerce, 1986.

[40] M. Matsuishi and T. Endo. Fatigue of metals subjected to varying stress. *Society of Mechanical Engineers, Fukuoka, Japan*, 1968.

[41] Sweden Centre for Mathematical Science, Lund University. Wafo toolbox, 2017.

[42] T.Kristiansen and H. Lie. NDP Riser High Mode VIV Tests - Modal Analysis. *Norwegian Deepwater Program: Riser and Mooring Project*, April 2005.

[43] R. Baarholm. Research activities in the norwegian deepwater programme. *Conference on CeSOS Highlights and AMOS Visions*, 2013.

[44] T.Kristiansen and H. Lie. NDP Riser High Mode VIV Tests - Response Analysis. *Norwegian Deepwater Program: Riser and Mooring Project*, April 2005.

# Appendix A

# Riflex input-files

## A.1 Template input-files

In order to run a set of simulations by a loop from Matlab, a set of template input-files were created. There was one template for both INPMOD, STAMOD and DYNMOD, as well as separate templates were used for the bare riser cases, the 50% and the 75% partially straked riser cases. Common features for all the templates were:

- In DYNMOD it is defined that the simulation length will be 400 fundamental cross-flow periods and that each cross-flow period will contain 40 time-steps. For each case the fundamental cross-flow period is altered in INPMOD.
- A constant tension, different from case to case, is applied at the lower end of the riser by applying a specified force to the last node of the lower segment in STAMOD.
- In INPMOD a uniform and a sheared current alternative are created, where the current speed is set to $1m/s$ for both current profiles (maximum for sheared current). In STAMOD it is for each case selected if the uniform or sheared current alternative should be applied, and the magnitude of the current speed is controlled by a scaling factor.

In addition the template input-file to INPMOD for the bare riser cases included an option for changing the hydrodynamic parameters, which was relevant during the calibration.

The template input-files are submitted in a zip-file and are found within relevant folders within the main folder "RIFLEX". "RIFLEX" contains the following folders and template-files:

**INPMOD:**

- Bare riser cases: ndp38m0_inpmod.inp.
- 50% partially straked riser cases: ndp38m0_Strakesinpmod.inp.
- 75% partially straked riser cases: ndp38m0_Strakes2inpmod.inp.

**STAMOD:**

- Bare riser cases: ndp38m0_stamod.inp.
- 50% partially straked riser cases: ndp38m0_Strakesstamod.inp.

- 75% partially straked riser cases: ndp38m0_Strakes2stamod.inp.

**DYNMOD:**

- Bare riser cases: ndp38m0_dynmod.inp.
- 50% partially straked riser cases: ndp38m0_Strakesdynmod.inp.
- 75% partially straked riser cases: ndp38m0_Strakes2dynmod.inp.

## A.2 Example input-files

In this section a set of input-files to INPMOD, STAMOD and DYNMOD are presented in order to illustrate the structure of these files. One input-file to INPMOD from the bare riser cases, the 50% and 75% partially straked riser cases are given, while only one input-file to STAMOD and DYNMOD from the bare riser cases are presented. This is because only the strake coverage is altered between the three groups of cases, which is done in INPMOD. The examples presented here are when the risers were exposed to shear flow with current speed $2.2 m/s$.

### A.2.1 INPMOD input-files

**Bare riser case**

```
'**********************************************************************
 INPMOD IDENTIFICATION TEXT 4.6.1
'**********************************************************************
NDP 38m pipe time domain VIV simulation
Bare cylinder
Shear flow: U=2.2 m/s
'----------------------------------------------------------------------
 UNIT NAMES SPECIFICATION
'----------------------------------------------------------------------
'ut ul um uf grav gcons
 s  m  Mg kN /    1.000000000e+00
'**********************************************************************
 NEW SINGLE RISER
'**********************************************************************
'atyps idris
 AR    ARSYS
'**********************************************************************
 ARBITRARY SYSTEM AR
'**********************************************************************
'nsnod nlin nsnfix nves nricon nspr nakc
 2     1    2      0    0      0    0
'ibtang zbot ibot3d
 0      0    0
'B 6.5: LINE TOPOLOGY DEFINITION
'lineid lintyp-id snod1-id snod2-id
 line1  ltyp1     node1    node2
'FIXED NODES
'snod-id ipos ix iy iz irx iry irz chcoo  chupro
```

```
 node1   0    1  1  1  0   1   0   GLOBAL NO
’x0       y0        z0        x1       y1        z1   rot    dir
 0.00e+00 0.00e+00 -5.00e+00  0.00e+00 0.00e+00 -5    0      0
’snod-id ipos ix iy iz irx iry irz chcoo  chupro
 node2   0    1  0  1  0   1   0   GLOBAL NO
’x0       y0        z0       x1       y1        z1    rot    dir
 0.00e+00 3.80e+01 -5.00e+00 0.00e+00 3.80e+01 -5     0      0
’B.10 Line and segment specification
’**********************************************************************
 NEW LINE DATA
’**********************************************************************
’lintyp-id nseg ncmpty2 flutyp iaddtwi iaddbend
 ltyp1     2    0        0      0       0
’crstyp ncmpty1 exwtyp nelseg slgth    nstrps nstrpd slgth0   isoity
cs1_1   0       0      250    1.90e+01 1      1      1.90e+01 0
’crstyp ncmpty1 exwtyp nelseg slgth    nstrps nstrpd slgth0   isoity
cs1_1   0       0      250    1.90e+01 1      1      1.90e+01 0
’**********************************************************************
 NEW COMPONENT CRS1
’**********************************************************************
’cmptyp-id temp     alpha    beta
 cs1_1     1.80e+01 0.00e+00 0.00e+00
’ams        ae          ai  rgyr ast wst dst thst rextcnt rintcnt
 0.9330e-03 5.7260e-04 0   0    0   0   0   0    0       0
’iea iej igt ipress imf harpar
 1   1   1   0      0   0.000000000e+00
’ea
 8.190000000e+03
’ei              gas
 0.599           0.000000000e+00
’gtminus
 4.91000000000e-01
’chload
 HYDR
’chtype
 TVIV
’cqx cqy cax cay clx cly  icode d     scfkn CV   FNUL  FMIN FMAX  NMEM CVIL ALPHIL CHH
0    0.9 0   1   0   0    2     0.027 1     0.85 0.144 0.08 0.208 500  0.98 0.15   0
’tb        ycurmx
50.00e+00  1.00e+00
’**********************************************************************
 ENVIRONMENT IDENTIFICATION
’**********************************************************************
Current only
’idenv
 ENV
’----------------------------------------------------------------------
 WATERDEPTH AND WAVETYPE
’----------------------------------------------------------------------
```

```
'wdepth   noirw norw ncusta nwista
 1.00e+01 0     1    3      0
'-----------------------------------------------------------------------
 ENVIRONMENT CONSTANTS
'-----------------------------------------------------------------------
'airden   watden     wakivi   airkivi
 1.20e-03 1.00e+00   1.00e-06 1.50e-05
'-----------------------------------------------------------------------
 REGULAR WAVE DATA
'-----------------------------------------------------------------------
'inrwc amplit   period   wavdir
1      1e-09    0.093023 0
'-----------------------------------------------------------------------
 NEW CURRENT STATE
'-----------------------------------------------------------------------
'icusta nculev l_ext
 1      2      0
'curlev    curdir   curvel
 0.00e+00  0.00e+00 1e+00
 -1.00e+01 0.00e+00 1e+00
'-----------------------------------------------------------------------
 NEW CURRENT LINE
'-----------------------------------------------------------------------
'icusta npt
 2      2
'ipt nculev xpt ypt
 1   2      0   0
'curlev curdir curvel
 0      0      1.0
 -10    0      1.0
'ipt nculev xpt ypt
 2   2      0   38
'curlev curdir curvel
 0      0      0
 -10    0      0
'***********************************************************************
 END
'***********************************************************************
```

**50% straked riser case**

```
'*********************************************************************
 INPMOD IDENTIFICATION TEXT 4.6.1
'*********************************************************************
NDP 38m pipe time domain VIV simulation
50% straked cylinder
Shear flow: U=2.2 m/s
'---------------------------------------------------------------------
 UNIT NAMES SPECIFICATION
'---------------------------------------------------------------------
'ut ul um uf grav    gcons
 s  m  Mg kN 9.81    1.000000000
'*********************************************************************
 NEW SINGLE RISER
'*********************************************************************
'atyps idris
 AR    ARSYS
'*********************************************************************
 ARBITRARY SYSTEM AR
'*********************************************************************
'nsnod nlin nsnfix nves nricon nspr nakc
 2     1    2      0    0      0    0
'ibtang zbot ibot3d
 0      0    0
'B 6.5: LINE TOPOLOGY DEFINITION
'lineid lintyp-id snod1-id snod2-id
 line1  ltyp1     node1    node2
'FIXED NODES
'snod-id ipos ix iy iz irx iry irz chcoo  chupro
 node1   0    1  1  1  0   1   0   GLOBAL NO
'x0       y0        z0        x1       y1        z1   rot      dir
 0.00e+00 0.00e+00 -5.00e+00  0.00e+00 0.00e+00 -5    0        0
'snod-id ipos ix iy iz irx iry irz chcoo  chupro
 node2   0    1  0  1  0   1   0   GLOBAL NO
'x0       y0        z0       x1       y1        z1    rot      dir
 0.00e+00 3.80e+01 -5.00e+00 0.00e+00 3.80e+01 -5     0        0
'B.10 Line and segment specification
'*********************************************************************
 NEW LINE DATA
'*********************************************************************
'lintyp-id nseg ncmpty2 flutyp iaddtwi iaddbend
 ltyp1     2    0       0      0       0
'crstyp ncmpty1 exwtyp nelseg slgth    nstrps nstrpd slgth0   isoity
cs2_1   0       0      250    1.90e+01 1      1      1.90e+01 0
'crstyp ncmpty1 exwtyp nelseg slgth    nstrps nstrpd slgth0   isoity
cs1_1   0       0      250    1.90e+01 1      1      1.90e+01 0
'*********************************************************************
 NEW COMPONENT CRS1
```

```
'**********************************************************************
'cmptyp-id temp     alpha    beta
 cs1_1     1.80e+01 0.00e+00 0.00e+00
'ams        ae         ai  rgyr ast wst dst thst rextcnt rintcnt
 0.9330e-03 5.7260e-04 0   0    0   0   0   0    0       0
'iea iej igt ipress imf harpar
 1   1   1   0      0   0.000000000e+00
'ea
 8.190000000e+03
'ei              gas
 0.599           0.000000000e+00
'gtminus
0.491
'chload
 HYDR
'chtype
 TVIV
'cqx cqy cax cay clx cly icode d     scfkn CV   FNUL FMIN FMAX  NMEM CVIL ALPHIL CHH
 0   0.9 0   1.0 0   0   2     0.027 1     0.85 0.144 0.08 0.208 500  0.98 0.15   0
'tb        ycurmx
50.00e+00  1.00e+00
'**********************************************************************
 NEW COMPONENT CRS2
'**********************************************************************
'cmptyp-id temp
 cs2_1     1.80e+01
'ams         ae         ai       rgyr
 1.2330e-03  5.7260e-04 0.00e+00 0.00e+00
'iea iej igt ipress
 1   1   1   0
'ea
 8.190e+03
'ejy        ejz        gasz     gasy
0.599       0.599      0.00e+00 0.00e+00
'gt-
 0.491
'chload
 HYDR
'chtype
 MORI
'CDX       CDY        CDZ        CDT AMX    AMY       AMZ      AMT CDLX CDLY CDLZ SCFKN SCFKT
 1.6253e-3 2.44898e-2 2.44898e-2 0   1.2e-6 12.596e-4 8.633e-4 0   0    0    0    1     1
'tb        ycurmx   zcurmx
 50.00e+00 1.00e+00 1.00e+00
'**********************************************************************
 ENVIRONMENT IDENTIFICATION
'**********************************************************************
Current only
'idenv
```

```
 ENV
'----------------------------------------------------------------------
 WATERDEPTH AND WAVETYPE
'----------------------------------------------------------------------
'wdepth   noirw norw ncusta nwista
 1.00e+01 0     1    3      0
'----------------------------------------------------------------------
 ENVIRONMENT CONSTANTS
'----------------------------------------------------------------------
'airden   watden     wakivi   airkivi
 1.20e-03 1.00e+00   1.00e-06 1.50e-05
'----------------------------------------------------------------------
 REGULAR WAVE DATA
'----------------------------------------------------------------------
'inrwc amplit   period   wavdir
1      1e-09    0.22154  0
'----------------------------------------------------------------------
 NEW CURRENT STATE
'----------------------------------------------------------------------
'icusta nculev l_ext
 1      2      0
'curlev    curdir   curvel
 0.00e+00  0.00e+00 1e+00
 -1.00e+01 0.00e+00 1e+00
'----------------------------------------------------------------------
 NEW CURRENT LINE
'----------------------------------------------------------------------
'icusta npt
 2      2
'ipt nculev xpt ypt
 1   2      0   0
'curlev curdir curvel
 0      0      1.0
 -10    0      1.0
'ipt nculev xpt ypt
 2   2      0   38
'curlev curdir curvel
 0      0      0
 -10    0      0
'**********************************************************************
 END
'**********************************************************************
```

**75% straked riser case**

```
'*********************************************************************
 INPMOD IDENTIFICATION TEXT 4.6.1
'*********************************************************************
NDP 38m pipe time domain VIV simulation
75% straked cylinder
Shear flow: U=2.2 m/s
'---------------------------------------------------------------------
 UNIT NAMES SPECIFICATION
'---------------------------------------------------------------------
'ut ul um uf grav    gcons
 s  m  Mg kN 9.81    1.000000000
'*********************************************************************
 NEW SINGLE RISER
'*********************************************************************
'atyps idris
 AR    ARSYS
'*********************************************************************
 ARBITRARY SYSTEM AR
'*********************************************************************
'nsnod nlin nsnfix nves nricon nspr nakc
 2     1    2      0    0      0    0
'ibtang zbot ibot3d
 0      0    0
'B 6.5: LINE TOPOLOGY DEFINITION
'lineid lintyp-id snod1-id snod2-id
 line1  ltyp1     node1    node2
'FIXED NODES
'snod-id ipos ix iy iz irx iry irz chcoo  chupro
 node1   0    1  1  1  0   1   0   GLOBAL NO
'x0       y0        z0        x1       y1        z1  rot  dir
 0.00e+00 0.00e+00 -5.00e+00  0.00e+00 0.00e+00 -5   0    0
'snod-id ipos ix iy iz irx iry irz chcoo  chupro
 node2   0    1  0  1  0   1   0   GLOBAL NO
'x0       y0        z0       x1       y1        z1   rot  dir
 0.00e+00 3.80e+01 -5.00e+00 0.00e+00 3.80e+01 -5    0    0
'B.10 Line and segment specification
'*********************************************************************
 NEW LINE DATA
'*********************************************************************
'lintyp-id nseg ncmpty2 flutyp iaddtwi iaddbend
 ltyp1     2    0       0      0       0
'crstyp ncmpty1 exwtyp nelseg slgth    nstrps nstrpd slgth0   isoity
cs2_1   0       0      375    2.85e+01 1      1      2.85e+01 0
'crstyp ncmpty1 exwtyp nelseg slgth    nstrps nstrpd slgth0   isoity
cs1_1   0       0      125    0.95e+01 1      1      0.95e+01 0
'*********************************************************************
 NEW COMPONENT CRS1
```

```
'**********************************************************************
'cmptyp-id temp     alpha    beta
 cs1_1     1.80e+01 0.00e+00 0.00e+00
'ams        ae         ai  rgyr ast wst dst thst rextcnt rintcnt
 0.9330e-03 5.7260e-04 0   0    0   0   0   0    0       0
'iea iej igt ipress imf harpar
 1   1   1   0      0   0.000000000e+00
'ea
 8.190000000e+03
'ei              gas
 0.599           0.000000000e+00
'gtminus
0.491
'chload
 HYDR
'chtype
 TVIV
'cqx cqy cax cay clx cly icode d     scfkn CV   FNUL  FMIN FMAX  NMEM CVIL ALPHIL CHH
 0   0.9 0   1.0 0   0   2     0.027 1     0.85 0.144 0.08 0.208 500  0.98 0.15   0
'tb        ycurmx
50.00e+00  1.00e+00
'**********************************************************************
 NEW COMPONENT CRS2
'**********************************************************************
'cmptyp-id temp
 cs2_1     1.80e+01
'ams         ae         ai       rgyr
 1.2330e-03  5.7260e-04 0.00e+00 0.00e+00
'iea iej igt ipress
 1   1   1   0
'ea
 8.190e+03
'ejy        ejz        gasz     gasy
0.599       0.599      0.00e+00 0.00e+00
'gt-
 0.491
'chload
 HYDR
'chtype
 MORI
'CDX        CDY         CDZ         CDTMOM AMX     AMY       AMZ       AMTOR CDLX CDLY CDLZ SCFKN  SC
 1.6253e-03 2.44898e-02 2.44898e-02 0      1.2e-06 8.633e-04 8.633e-04 0     0    0    0    1      1
'tb        ycurmx   zcurmx
 50.00e+00 1.00e+00 1.00e+00
'**********************************************************************
 ENVIRONMENT IDENTIFICATION
'**********************************************************************
Current only
'idenv
```

```
 ENV
'----------------------------------------------------------------------
 WATERDEPTH AND WAVETYPE
'----------------------------------------------------------------------
'wdepth   noirw norw ncusta nwista
 1.00e+01 0     1    3      0
'----------------------------------------------------------------------
 ENVIRONMENT CONSTANTS
'----------------------------------------------------------------------
'airden   watden     wakivi   airkivi
 1.20e-03 1.00e+00   1.00e-06 1.50e-05
'----------------------------------------------------------------------
 REGULAR WAVE DATA
'----------------------------------------------------------------------
'inrwc amplit   period   wavdir
1      1e-09    0.20735  0
'----------------------------------------------------------------------
 NEW CURRENT STATE
'----------------------------------------------------------------------
'icusta nculev l_ext
 1      2      0
'curlev    curdir   curvel
 0.00e+00  0.00e+00 1e+00
 -1.00e+01 0.00e+00 1e+00
'----------------------------------------------------------------------
 NEW CURRENT LINE
'----------------------------------------------------------------------
'icusta npt
 2      2
'ipt nculev xpt ypt
 1   2      0   0
'curlev curdir curvel
 0      0      1.0
 -10    0      1.0
'ipt nculev xpt ypt
 2   2      0   38
'curlev curdir curvel
 0      0      0
 -10    0      0
'**********************************************************************
 END
'**********************************************************************
```

### A.2.2 STAMOD input-file: bare riser case

```
'A1 STAMOD IDENTIFICATION TEXT
'*********************************************************************
 STAMOD CONTROL INFORMATION 4.6.1
'*********************************************************************
NDP 38m pipe time domain VIV simulation
Bare cylinder
Shear flow: U=2.2 m/s
'---------------------------------------------------------------------
'A1.3   OPTION AND PRINT SWITCHES
'irunco idris ianal iprdat iprcat iprfem ipform iprnor ifilm ifilco
 1      ARSYS 1     2      1      1      1      1      2     0
'---------------------------------------------------------------------
 RUN IDENTIFICATION
'---------------------------------------------------------------------
'idres
 SIMA
'---------------------------------------------------------------------
 ENVIRONMENT REFERENCE IDENTIFIER
'---------------------------------------------------------------------
'idenv
 ENV
'---------------------------------------------------------------------
' STORE VISUALISATION RESPONSES
'---------------------------------------------------------------------
'option chresp chilin
' STORE  ALL    ALL
'*********************************************************************
 STATIC CONDITION INPUT
'*********************************************************************
'lcomp icurin curfac        iwindin
 1     2      2.2           0
'line-id ilseg ilnode ildof rlmag  chicoo
 line1   2     251    2     4.425  GLOBAL
'lcons isolvr
 0     2
'*********************************************************************
 COMPUTATIONAL PROCEDURE
'*********************************************************************
'ameth
 FEM
'---------------------------------------------------------------------
 FEM ANALYSIS PARAMETERS
'---------------------------------------------------------------------
'.....................................................................
 LOAD GROUP DATA
'.....................................................................
'nstep maxit racu
```

```
 10    10    1.000000000e-06
'lotype ispec
 SFOR   0
'.......................................................................
 LOAD GROUP DATA
'.......................................................................
'nstep maxit racu
 10    10    1.000000000e-06
'lotype ispec
 VOLU   0
'.......................................................................
 LOAD GROUP DATA
'.......................................................................
'nstep maxit racu
 10    10    1.000000000e-06
'lotype ispec
 CURR   0
'***********************************************************************
 END
'***********************************************************************
```

### A.2.3 DYNMOD input-file: bare riser case

```
'A1 DYNMOD CONTROL INFORMATION
'*******************************************************************
 DYNMOD CONTROL INFORMATION 4.6.1
'*******************************************************************
NDP 38m pipe time domain VIV simulation
Bare cylinder
Shear flow: U=2.2 m/s
'-------------------------------------------------------------------
'irunco ianal   idris idenv idstat idirr idres
 ANAL   REGULAR ARSYS ENV   SIMA   XX    SIMA
'******************************************************************
'
'          DATA GROUP C, REGULAR WAVE, TIME DOMAIN ANALYSIS
'
'*******************************************************************
 REGULAR WAVE ANALYSIS
'*******************************************************************
'nper nstppr irwcn imotd
 400  40     1     0
'*******************************************************************
 REGULAR WAVE LOADING
'*******************************************************************
'iwtyp isurf iuppos
 1     1     2
'******************************************************************
'
'          DATA GROUP E
' Time domain procedure and file storage parameters
'
'*******************************************************************
 TIME DOMAIN PROCEDURE
'*******************************************************************
'itdmet inewil
 2      1
'E1.3   TIME INTEGRATION
'betin gamma    theta a1 a2      a1t a1to a1b a2t a2t0 a2b
 4.0   5.0e-01  1     0  0.0001  0   0    0   0   0    0
'E1.4    NONLINEAR FORCE MODEL
'indint indhyd maxhit epshyd          tramp           indrel iconre istepr ldamp
 1      3      5      1.000000000e-02 0.000000000e+01 0      0      0      0
'-------------------------------------------------------------------
 NONLINEAR INTEGRATION PROCEDURE
'-------------------------------------------------------------------
'itfreq isolit maxit daccu           icocod ivarst itstat
 1      1      10    1.000000000e-05 1      0      1
'-------------------------------------------------------------------
 DISPLACEMENT RESPONSE STORAGE
```

```
'----------------------------------------------------------------------
'idisp nodisp idisfm
 2     2      -1
'line-id iseg inod
 line1   1    ALL
 line1  2    ALL
'----------------------------------------------------------------------
 CURVATURE RESPONSE STORAGE
'----------------------------------------------------------------------
'icurv nocurv icurfm
 2     2     -1
'line-id iseg iel
 line1   1    ALL
 line1   2    ALL
'----------------------------------------------------------------------
 ENVELOPE CURVE SPECIFICATION
'----------------------------------------------------------------------
'ienvd ienvf ienvc tenvs           tenve           nprend nprenf nprenc ifilmp
 1     1     1     0.000000000e+00 1.000000000e+07 1      1      1      2
'
'STORE VISUALISATION RESPONSES
'
'TCONDS TCONDE DELT CHFORM
' 0        50    0.01   VIS
'**********************************************************************
 END
'**********************************************************************
```

# Appendix B

# Matlab scripts

Here all the relevant Matlab scripts used in the thesis are presented and briefly explained. The scripts are all submitted in a zip-file and are found within relevant folders within the main folder ”MATLAB”. ”MATLAB” contains the following folders with associated scripts:

**RUN SIMULATIONS**
This folder contains the scripts that were used for running simulations, as well as loading and saving the processed experimental NDP-data from excel-files and mat-files (these are found in ”NDP DATA”). These scripts load the template input-files and write the data related to the case considered to the file. One script for the bare riser cases and one script for each of the two partial strake coverage cases were created:

- BareSimulations.m. Script for running bare riser cases. Note that some processing is included in this script because it was found convenient for the calibration.
- Strakes50Simulations.m. Script for running 50% straked riser cases.
- Strakes75Simulations.m. Script for running 75% straked riser cases.

Within the folder ”Myfuncs\riflex” the function riflex.m, which runs Riflex in batch mode from Matlab, is found. It requires several sub-functions which are found in ”Myfuncs”.

**NDP DATA**
The scripts for processing the NDP experimental data are found in this folder. In addition, text files with time windows for the steady-state periods, peak frequencies and more, which are taken as input to the processing scripts, are found here:

- Bare riser cases: NDPmeas_bare.m and icasesd2.txt.
- 50% straked riser cases: NDPmeas_50strakes.m and icasesstrakes.txt.
- 75% straed riser cases: NDPmeas_75strakes.m and icasesstrakes2.txt.

The mat-files with the NDP experimental raw data and the function acc2displ.m, which computes displacements from measured accelerations, are also found in this folder. In addition the mat-files (nakedmeasdata1w.mat, strakedmeasdata1w.mat and straked2measdata1w.mat) and excel-files (bare_1w.xlsx, straked_1w.xlsx and straked2_1w.xlsx) with the processed NDP data are contained in this folder.

### POST PROCESSING

For post processing of the simulation data and comparison with the experimental data, one script for each of the three groups of cases was used:

- postproc_Bare.m. Script for post processing bare riser cases.
- postproc_50Strakes.m. Script for post processing 50% straked riser cases.
- postproc_75strakes.m. Script for post processing 75% straked riser cases.

The script bpass.m, used for band-pass filtering, is also found in this folder, as well as the MATLAB routines from Wafo. dat2tp.m, tp2rfc.m and cc2dam.m are the Wafo routines used for computing the fatigue damage from a stress time series.

Håkon Drengsrud

Systematic Evaluation of VIV Prediction for Riser with Partial Strake Coverage

NTNU
Norwegian University of
Science and Technology